UNIVERSITY OF OKLAHOMA

GRADUATE COLLEGE

EVALUATING THE PERFORMANCE OF A NONLINEAR DUAL-MODE VIBRATION ISOLATOR/ABSORBER SYSTEM

A THESIS

SUBMITTED TO THE GRADUATE FACULTY

in partial fulfillment of the requirements for the

Degree of

MASTER OF SCIENCE

By

PUTHYNAN BIN
Norman, Oklahoma
2021

Downloaded from SHAREOK. Persistent Handle URL: https://hdl.handle.net/11244/329571

EVALUATING THE PERFORMANCE OF A NONLINEAR DUAL-MODE VIBRATION ISOLATOR/ABSORBER SYSTEM

A THESIS APPROVED FOR THE
SCHOOL OF CIVIL ENGINEERING AND ENVIRONMENTAL SCIENCE

BY THE COMMITTEE CONSISTING OF

Dr. Philip S. Harvey Jr., Chair

Dr. Royce W. Floyd

Dr. Jin-Song Pei

© Copyright by PUTHYNAN BIN 2021
All Rights Reserved.

This thesis is dedicated to my beloved mother, Ratana Chhoeum, who has always been there for me through countless hardships. She is the strongest person I know, and this achievement would have never been made possible without her love, perseverance, and hard work.

Acknowledgements

I would like to express my deepest appreciation and gratitude to my advisor, Dr. Philip S. Harvey Jr., whose advise, guidance, and support serve as the main inspiration that leads to my accomplishment today. No words can express how much I have learned from him throughout this incredible journey.

I would like to also thank the rest of my committee members, Dr. Royce W. Floyd and Dr. Jin-Song Pei, for their feedback that helps improve the quality of this thesis. Thank you to the OU CEES department and Gallogly College of Engineering for their supports, scholarships, and opportunities. Special thanks to Mr. Shelby Davis for his financial support throughout my college education and the staffs of OU UWC scholar program for their works.

I would like to extend this acknowledgement to my beloved brothers and close friends for always believing in me and providing emotional supports through all my ups and downs.

Last but not least, I would like to thank the National Science Foundation (NSF) for funding this project. This material is based upon work supported by the NSF under award No. CMMI-1663376.

Table of Contents

Acknowledgments . . . . . **v**

Table of Contents . . . . . **vi**

List of Figures . . . . . **ix**

List of Tables . . . . . **xiv**

Abstract . . . . . **xv**

1 Introduction **1**
- 1.1 Background and Motivation 1
- 1.2 Literature Review 3
  - 1.2.1 Raised Floor Isolation System (FIS) 3
  - 1.2.2 Vibrational Energy Absorbing System 6
  - 1.2.3 Combined System for Vibration Isolation/Absorption 10
- 1.3 Summary 11

2 Probabilistic Design of a Dual-mode FIS* **12**
- 2.1 Overview 12
- 2.2 Mathematical Model of the Coupled PS-FIS System 17
  - 2.2.1 Non-linear Reduced Order Model (NLROM) via Component Mode Synthesis 17
  - 2.2.2 Nonlinear FIS model 19
- 2.3 Multi-Objective Design Problem Formulation 20
  - 2.3.1 Response Quantities and Evaluation Criteria 20
  - 2.3.2 Dual-mode FIS optimization 22
- 2.4 Illustrative Example 24
  - 2.4.1 Description of the PS-FIS model considered 24
  - 2.4.2 Seismic excitations 26
  - 2.4.3 Baseline (linear) performance 28
  - 2.4.4 Parametric study 30
- 2.5 Optimization Study 35
  - 2.5.1 Nominal Case 37
  - 2.5.2 Effect of Lognormal Standard Deviation on Optimal Design . . 41

2.5.3 Effect of Threshold Values on Optimal Design 42
2.5.4 Effect of Mass Ratio and Installation Location on Optimal Design 44
2.6 Optimization with Genetic Algorithm 45
2.7 Summary 47

3 Experimental evaluation of the performance of a nonlinear dual-mode vibration isolator/absorber system 49
3.1 Overview 49
3.2 Problem Formulation 49
3.2.1 Floor Isolation System 49
3.2.2 Nonlinear FIS force 53
3.2.3 Primary Structure 54
3.2.4 The Coupled PS-FIS System 55
3.2.5 Performance Metrics 57
3.3 Experimental System 58
3.3.1 Primary Structure 58
3.3.2 Floor Isolation System 60
3.3.3 Bumper 61
3.4 Experimental Protocol 61
3.4.1 PS-FIS Setup 62
3.4.2 Ground Motions and Testing 64
3.4.3 Testing procedure 67
3.5 Experimental Results 69
3.5.1 El Centro 69
3.5.2 Hachinohe 73
3.5.3 Kobe 77
3.5.4 Northridge 80
3.5.5 Normalized Performance Indices 82
3.5.6 Discussion of the Experimental Results 85
3.6 Numerical Results 85
3.7 Summary 91

4 Summary, Conclusions, and Future Work 94
4.1 Summary and Conclusions 94
4.2 Future Work 95

Bibliography 96

A State Space Formulation 104

B Equilibrium Formulation 106

C System Identification of Experimental Structure 108
C.1 Mathematical Formulation 108

C.2 System Identification 111
C.2.1 Mass and Stiffness Identification 111
C.2.2 Modal Damping Estimation 114

D Characterization Test 116

List of Figures

1.1 FPS bearing 4
1.2 RNC isolator 5
1.3 SCF on a raised-floor system in a multi-story structure 6
1.4 Track NES 8
1.5 SSVI track NES 8
1.6 Schematic design of the systems on the nine-story structure 9
1.7 Schematic of a dual-mode vibration isolator/absorber system 10

2.1 Coupled PS-FIS system 16
2.2 Nonlinear force-displacement relationship assumed for the FIS force f_{FIS} 19
2.3 Force-displacement relationships of the FIS under harmonic displacement with increasing amplitude (A) for various stiffness parameter κ = 1, 50, and 100 and damping parameter χ = (B) 1 and (C) 10. 20
2.4 Comparison of responses calculated using the full PS model and those using nonlinear reduced order models (NLROMs) with r = 3, 2, or 1 mode retained: FIS (μ = 5%, d_o = 20.3 cm, κ = 50, and χ = 10) installed on the second level of PS subject to a MCE-level GM. 25
2.5 Transfer functions from ground acceleration to (A) FIS displacement $d_{\max}$, (B) FIS acceleration $a_{\max}$ and story level acceleration $a^{\text{PS}}_{\max}$, (C) maximum inter-story drift $\delta_{\max}$, and (D) roof drift $\Delta_{\max}$ for varying isolated mass ratios: μ = 0 (no isolation), 5%, and 20%. 26
2.6 Response spectra (5% damped) of 50 synthetic ground motions (GMs) used in numerical study, including mean and one standard deviation. . . 27
2.7 Empirical cumulative probabilities of peak responses—(A) FIS displacement, (B) FIS and story level accelerations, (C) inter-story drift ratio, and (D) roof drift ratio—for a linear FIS of varying mass ratio μ installed on the second level subject to DBE-scaled GMs 30
2.8 Empirical cumulative probabilities of peak responses of PS-FIS systems with various gaps d_o subject to SLE-scaled GMs: μ = 5%, κ = 50, and χ = 10. The two highlighted cases are the linear FIS ($d_o \to \infty$; —) and a nonlinear FIS with d_o = 20.3 cm (– – –) 31
2.9 Empirical cumulative probabilities of peak responses of PS-FIS systems with various gaps d_o subject to MCE-scaled GMs: μ = 5%, κ = 50, and χ = 10. The two highlighted cases are the linear FIS ($d_o \to \infty$; —) and a nonlinear FIS with d_o = 20.3 cm (– – –) 32

2.10 Empirical cumulative probabilities of the ratio $\delta_{\max}/\delta_{\max}^{\text{linear}}$ of the peak inter-story drift with FISs of various gaps d_o to the linear FIS, subject to MCE-scaled GMs: $\mu = 5\%$, $\kappa = 50$, and $\chi = 10$. The two highlighted cases are the linear FIS ($d_o \to \infty$; —) and a nonlinear FIS with $d_o = 20.3$ cm (– – –) 33
2.11 Effect of gap d_o on evaluation criteria (A) FIS failure probability and (B) PS failure probability under SLE- and MCE-scaled GMs, respectively, for various isolated mass ratio μ: FIS ($\kappa = 50$ and $\chi = 10$) installed on the second level. 34
2.12 (A) Probability of peak FIS acceleration exceeding $a_{\text{thresh}} = 0.3g$ under SLE-scaled GMs, and (B) probability of peak inter-story drift ratio exceeding $\delta_{\text{thresh}} = 3\%$ under MCE-scaled GMs: FIS ($\mu = 5\%$) installed on the second level. Note that different color scales are used in (A) and (B) to represent the probabilities. 38
2.13 (A) Pareto front for a FIS ($\mu = 5\%$) installed on the second level, and (B) Pareto optimal design parameters. The horizontal/vertical lines are for the cases of no FIS (– – –) and linear FIS (– · –), and the gray points are the 25,000 individual samples in the random search. Note that unequal axes scales are used to represent the failure probabilities (A). 40
2.14 Effect of lognormal standard deviation β on (A) Pareto front for a FIS ($\mu = 5\%$) installed on the second level and (B) Pareto optimal design parameters. Note that unequal axes scales are used to represent the failure probabilities (A). 41
2.15 Effect of acceleration threshold a_{thresh} on (A) Pareto front for a FIS ($\mu = 5\%$) installed on the second level and (B) Pareto optimal design parameters. Note that unequal axes scales are used to represent the failure probabilities (A). 42
2.16 Effect of drift threshold δ_{thresh} on (A) Pareto front for a FIS ($\mu = 5\%$) installed on the second level and (B) Pareto optimal design parameters. Note that unequal axes scales are used to represent the failure probabilities (A). 43
2.17 Pareto fronts for FISs with varying mass ratio μ installed on the (A) first level, (B) second level, and (C) third level. The horizontal/vertical lines are for the cases of no FIS (– – –) and linear FIS (– · –). 45
2.18 Comparison of Pareto fronts determined from a random search (25,000 samples) and a genetic algorithm (GA) with 50 or 100 individuals per generation: FIS ($\mu = 5\%$) installed on the second level. Note that unequal axes scales are used to represent the failure probabilities. 46

3.1 Schematic of friction pendulum (FP) bearing. 50
3.2 Primary structure at Fears Lab 59
3.3 Experimental floor isolation system 60
3.4 Load-deflection curves based on (a) experimental data and (b) estimated contact force f_c model 62

3.5 Experimental PS-FIS system 62
3.6 A camera shot from the second story camera capturing the second interstory drift 63
3.7 Time histories of (a) El Centro, (b) Hachinohe, (c) Kobe and (d) Northridge 64
3.8 Response spectrum with 5% damping for (a) unscaled and (b) scaled GMs 64
3.9 Peak responses with no FIS and locked FIS for El Centro: (a) 2nd floor total acceleration a_2, (b) 1st story drift δ_1, (c) 2nd story drift δ_2, and (d) 3rd story drift δ_3. 70
3.10 Peak FIS responses with different seismic gaps for El Centro: (a) total accelerations a_2 and a_{FIS}, and (b) FIS displacement d_{FIS}. The horizontal lines represent the seismic gap for each case (based on line style). The filled markers indicates cases in which impacts occurred in the FIS. . . . 71
3.11 Peak PS responses with different seismic gaps for El Centro: (a) 1st story drift δ_1, (b) 2nd story drift δ_2, and (c) 3rd story drift δ_3. The filled markers indicates cases in which impacts occurred in the FIS. 72
3.12 Peak responses with no FIS and locked FIS for Hachinohe: (a) 2nd floor total acceleration a_2, (b) 1st story drift δ_1, (c) 2nd story drift δ_2, and (d) 3rd story drift δ_3. 74
3.13 Peak FIS responses with different seismic gaps for Hachinohe: (a) total accelerations a_2 and a_{FIS}, and (b) FIS displacement d_{FIS}. The horizontal lines represent the seismic gap for each case (based on line style). The filled markers indicates cases in which impacts occurred in the FIS. . . . 76
3.14 Peak PS responses with different seismic gaps for for Hachinohe: (a) 1st story drift δ_1, (b) 2nd story drift δ_2, and (c) 3rd story drift δ_3. The filled markers indicates cases in which impacts occurred in the FIS. . . . 76
3.15 Peak responses with no FIS and locked FIS for Kobe: (a) 2nd floor total acceleration a_2, (b) 1st story drift δ_1, (c) 2nd story drift δ_2, and (d) 3rd story drift δ_3. 77
3.16 Peak FIS responses with different seismic gaps for Kobe: (a) total accelerations a_2 and a_{FIS}, and (b) FIS displacement d_{FIS}. The horizontal lines represent the seismic gap for each case (based on line style). The filled markers indicates cases in which impacts occurred in the FIS. . . . 79
3.17 Peak PS responses with different seismic gaps for Kobe: (a) 1st interstory drift δ_1, (b) 2nd interstory drift δ_2, and (c) 3rd interstory drift δ_3. The filled markers indicates cases in which impacts occurred in the FIS. 79
3.18 Peak responses with no FIS and locked FIS for Northridge: (a) 2nd floor total acceleration a_2, (b) 1st story drift δ_1, (c) 2nd story drift δ_2, and (d) 3rd story drift δ_3. 80
3.19 Peak FIS responses with different seismic gaps for Northridge: (a) total accelerations a_2 and a_{FIS}, and (b) FIS displacement d_{FIS}. The horizontal lines represent the seismic gap for each case (based on line style). The filled markers indicates cases in which impacts occurred in the FIS. . . . 81

3.20 Peak PS responses with different seismic gaps for Northridge: (a) 1st interstory drift δ_1, (b) 2nd interstory drift δ_2, and (c) 3rd interstory drift δ_3. The filled markers indicates cases in which impacts occurred in the FIS. 82
3.21 Peak total acceleration performance index J_a for (a) El Centro, (b) Hachinohe, (c) Kobe, and (d) Northridge. The filled markers indicates cases in which impacts occurred in the FIS. 83
3.22 Peak interstory drift performance index J_δ for (a) El Centro, (b) Hachinohe, (c) Kobe, and (d) Northridge. The filled markers indicates cases in which impacts occurred in the FIS. 84
3.23 Spectrograms of the roof acceleration for gap B subject to (a) El Centro, (b) Hachinohe, (c) Kobe, and (d) Northridge. 86
3.24 Peak FIS responses with different seismic gaps for El Centro: (a) total accelerations a_2 and a_{FIS}, and (b) FIS displacement d_{FIS}. The horizontal lines represent the seismic gap for each case (based on line style). The grey portion indicates cases in which there are no impact whereas the black portion indicates cases in which impacts occurred in the FIS. . . . 87
3.25 Peak PS responses with different seismic gaps for El Centro: (a) 1st interstory drift δ_1, (b) 2nd interstory drift δ_2, and (c) 3rd interstory drift δ_3. The grey portion indicates cases in which there are no impact whereas the black portion indicates cases in which impacts occurred in the FIS. . 88
3.26 Peak FIS responses with different seismic gaps for Hachinohe: (a) total accelerations a_2 and a_{FIS}, and (b) FIS displacement d_{FIS}. The horizontal lines represent the seismic gap for each case (based on line style). The grey portion indicates cases in which there are no impact whereas the black portion indicates cases in which impacts occurred in the FIS. . . . 88
3.27 Peak PS responses with different seismic gaps for Hachinohe: (a) 1st interstory drift δ_1, (b) 2nd interstory drift δ_2, and (c) 3rd interstory drift δ_3. The grey portion indicates cases in which there are no impact whereas the black portion indicates cases in which impacts occurred in the FIS. . 89
3.28 Peak FIS responses with different seismic gaps for Kobe: (a) total accelerations a_2 and a_{FIS}, and (b) FIS displacement d_{FIS}. The horizontal lines represent the seismic gap for each case (based on line style). The grey portion indicates cases in which there are no impact whereas the black portion indicates cases in which impacts occurred in the FIS. . . . 89
3.29 Peak PS responses with different seismic gaps for Kobe: (a) 1st interstory drift δ_1, (b) 2nd interstory drift δ_2, and (c) 3rd interstory drift δ_3. The grey portion indicates cases in which there are no impact whereas the black portion indicates cases in which impacts occurred in the FIS. . 90

3.30 Peak FIS responses with different seismic gaps for Northridge: (a) total accelerations a_2 and a_{FIS}, and (b) FIS displacement d_{FIS}. The horizontal lines represent the seismic gap for each case (based on line style). The grey portion indicates cases in which there are no impact whereas the black portion indicates cases in which impacts occurred in the FIS. . . . 90
3.31 Peak PS responses with different seismic gaps for Northridge: (a) 1st interstory drift δ_1, (b) 2nd interstory drift δ_2, and (c) 3rd interstory drift δ_3. The grey portion indicates cases in which there are no impact whereas the black portion indicates cases in which impacts occurred in the FIS. . 91
3.32 Peak total acceleration performance index J_a for (a) El Centro, (b) Hachinohe, (c) Kobe, and (d) Northridge. The grey portion indicates cases in which there are no impact whereas the black portion indicates cases in which impacts occurred in the FIS. 92
3.33 Peak interstory drift performance index J_δ for (a) El Centro, (b) Hachinohe, (c) Kobe, and (d) Northridge. The grey portion indicates cases in which there are no impact whereas the black portion indicates cases in which impacts occurred in the FIS. 93

B.1 Free body diagram of a FP bearing. 106

C.1 First singular values of the power spectral density matrix for each configuration, with the identified frequencies indicated ($*$). 111
C.2 Frequency response data ($\cdot$) from the (a) first, (b) second, and (c) third floors, indicating selected data ($\circ$) used to fit modal damping ratios, with the fitted transfer functions (—). 115

D.1 FIS setup for sine sweep test 116
D.2 Sine sweep test exhibiting hysteresis (history dependence) 117

List of Tables

2.1 Average PS response quantities for the linear PS-FIS system with varying mass ratios μ installed on the second level subject to DBE-scaled GMs. The term in brackets is the percent reduction in the response quantities when compared to the case of no FIS ("Rigid"). 29
2.2 Performance criteria for the linear PS-FIS system with varying mass ratios μ installed different stories. The term in brackets is the reduction in the failure probability when compared to the case of no FIS ("Rigid"). 36
2.3 Nominal parameters used in the multi-objective optimization study, about which parametric variations are considered. 37

3.1 Mass and stiffness of each floor of the experimental structure 59
3.2 Modal properties of the experimental structure 59
3.3 Ground motions used for study, including peak values for the unscaled records. 65
3.4 Characteristics of unscaled ground motions. 65
3.5 Experimental tests conducted. Impacts were observed at scale factors that are *italicized*. 68
3.6 Seismic gaps used for experimental FIS 69

C.1 Configurations for system identification 110
C.2 Identified modal frequencies using frequency domain decomposition (FDD). 111
C.3 Experimental structure components and weights. 113
C.4 Best estimates of modal frequencies based on GA-optimized masses and stiffnesses. 114

Abstract

During the event of an earthquake, motion-sensitive equipment inside a building can be protected from seismic disturbance using a floor isolation system (FIS). Its behaviour is assumed linear when it displaces within the allowable capacity of its seismic gap and nonlinear when it displaces beyond, resulting in an impact between the FIS and the displacement limit, which can be augmented with a shock absorber. This induced nonlinearity may create a non-negligible dynamic coupling between the primary structure (PS) and the FIS, which can possibly be tuned to reduce the PS responses during strong earthquakes. This research aims to evaluate the performance of the FIS as a vibration isolator when subjected to low-intensity earthquakes (i.e., before impact occurs) and as a vibration absorber when subjected to high-intensity earthquakes (i.e., after impact occurs). Such a FIS is termed *dual-mode vibration isolator/absorber system* whose quantities of interest concern peak FIS acceleration and peak PS interstory drift when evaluating the isolation performance and the absorption performance, respectively. Two approaches are used to realize and evaluate the FIS's dual behaviour. A probabilistic approach is based on a numerical simulation that uses a nonlinear reduced order model to investigate the FIS performance when subjected to a suite of synthetic ground motions at various hazard levels, as well as to optimize some controlling parameters via two competing objective functions. An experimental approach is based on a lab-scale experiment to study the FIS performance when attached to the second story of the PS that is subjected to four historic ground motions. The data has shown promising result that suggests the dual performance of the FIS.

Chapter 1
Introduction

1.1 Background and Motivation

During a seismic event, the intensity of a ground motion (GM) plays an important role in determining the damage state of a structure. For a high intensity disturbance, the GM can cause irreparable damage to structural members, potentially resulting in collapse. In such a scenario, the priority course of action would be to save lives of the building's occupants. Mitigating structural responses during an earthquake can be achieved through a base isolation system, which is detailed in later sections. During a small to moderate disturbance, the ground motion of an earthquake may not cause the collapse of a building but could potentially damage expensive and mission-critical equipment inside the building, disrupting business operations. This may include the computers in data centers, displays in a museum, and much more. Therefore, if a structure is predicted to be subjected to this type of GM, it can be more economical to focus the engineering design on mitigating the response of such sensitive contents rather than the entire building. Such mitigation can be achieved through a number of methods: (1) isolating the base of an entire building (Konstantinidis and Nikfar, 2015; Shi et al., 2014; Chen et al., 2016; Ryan et al., 2016), (2) isolating individual objects (Baggio et al., 2015; Tsai et al., 2010; Harvey et al., 2014; Calhoun et al., 2019; Casey et al., 2018; Harvey and Gavin, 2013), or (3) isolating a raised floor of the structure that objects are placed on (Lambrou and Constantinou, 1994; Hamidi and El Naggar, 2007; Ismail et al., 2009; Gidaris et al.,

2016; Liu and Warn, 2012). The scope of this research is limited to the third method.

Seismic base isolation is a method of elongating the fundamental period of a structure by placing isolation devices at the base of a building to decouple it from the ground (Warn and Ryan, 2012). This results in acceleration reduction of structural components during an earthquake. Similar to base isolation system, a floor isolation system (FIS) isolates the objects from the floor so that the transmission of the floor motion to the objects can be mitigated. Another technique of vibration control can be achieved through vibration absorbers. These devices absorb the vibrational energy of the building and dissipate it to a higher order mode of the structure. Vibration absorbers and FISs work as secondary systems attached to the primary structure (PS) to absorb the vibrational energy of the PS and isolate building contents from the motion of the building, respectively.

Seeing the potential in seismic mitigation of both the vibration absorbers and isolation systems, an idea has been recently proposed to combine the two systems into a single dual-mode vibration isolator/absorber system (Harvey et al., 2018). This study had only shown that such a device proves effective for mitigating the response of a harmonic base excitation, but did not do so for seismic. Therefore, this research aims to fill this gap by studying the combined system to mitigate seismic response due to a moderate earthquake to protect building contents and passively adapt to protect the PS under strong earthquakes. To do so, different intensity level earthquakes have been considered (Tehrani and Harvey, 2019) — service level earthquake (SLE), design basis earthquake (DBE), and maximum considered earthquake (MCE). SLE is used in relation to the vibration isolator, whereas DBE and MCE are used in the context of vibration absorber due to their higher excitation intensities relative to the SLE. Therefore, this research focuses on evaluating the performance of a *nonlinear dual-mode vibration isolator/absorber system* subjected to seismic excitation.

1.2 Literature Review

This section provides insights of the past and current research findings relevant to important vibration isolator and absorber concepts that are part of this research.

1.2.1 Raised Floor Isolation System (FIS)

The FIS has been a topic of research and discussion for many years now. It has proved to be an effective technique in providing protection to motion-sensitive building contents. Since the FIS decouples the contents from the floor, the transmission of the acceleration from the floor to the contents can be mitigated. There are many types of FISs that have been proposed and tested, including friction pendulum system (FPS), roll-n-cage (RCN) isolation system, sliding concave foundation (SCF) system, and variable frequency pendulum isolator (VFPI), among others. A few of these are described here.

In research conducted by Lambrou and Constantinou (1994), the FPS as shown in Figure 1.1 has been studied. The bearing consists of a concave spherical surface faced with stainless steel and an articulated slider. With a radius of curvature of 22 in., the isolation system has a period of 1.5 sec and an allowable displacement of 3.5 in. Three different isolation configurations using FPS bearings were installed on a raised floor, and a cabinet functioning as the computer replica was placed on the raised floor to be tested. In the first configuration, only high friction FPS bearings were used for testing. Fluid viscous dampers were added to the system of lower friction FP bearings during testing of the second and third isolation configurations to enhance the system's ability to dissipate energy. The bearing was tested by installing it between the raised floor and a shake table, with the spherical FPS surface facing down. The results showed that there was a substantial reduction in the response of a generic computer cabinet on top of the isolated floor compared to a non-isolated system. The authors concluded that the isolation bearings having a period of 3 sec, damping ratio of 50%, and coefficient of

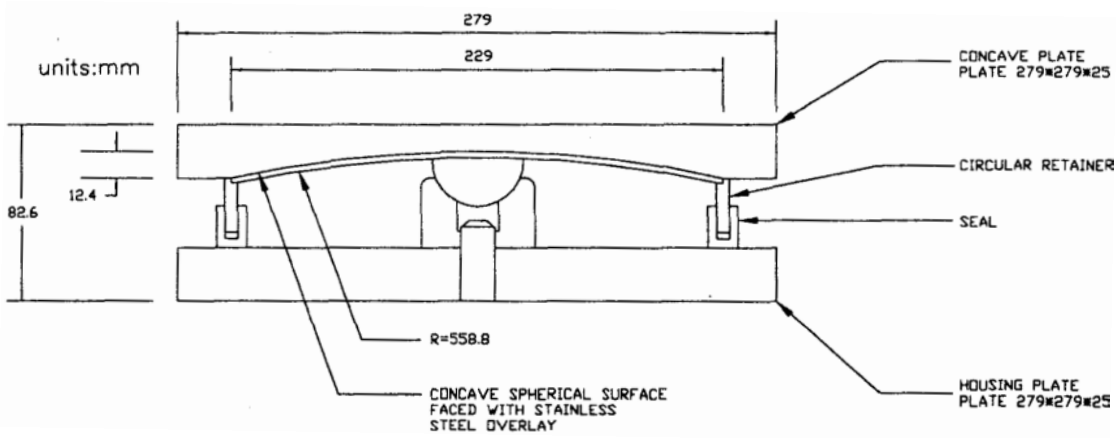


Figure 1.1: FPS bearing. Source: Lambrou and Constantinou (1994)

friction of 0.05 were the most effective in reducing the responses.

In Ismail et al. (2009), the study of an innovative isolation bearing for motion-sensitive equipment using roll-n-cage (RNC) isolation system as shown in Figure 1.2 was discussed. The RNC was proposed and tested using the raised floor approach. The RNC isolation bearing consists of a stiff rolling body placed between two stiff circular plates attached to the isolated object and the base floor (Ismail et al., 2009). Three cases — (a) isolated floor on fixed base structure, (b) non-isolated equipment on RNC isolated base structure, and (c) non-isolated equipment on fixed-base structure — were tested under harmonic ground motions and actual earthquakes. The results showed a substantial reduction in the acceleration of the equipment in the isolated case compared to the non-isolated equipment.

Another floor isolation approach that has increasingly gained popularity is a sliding isolator. Hamidi and El Naggar (2007) investigated the performance of sliding concave foundation (SCF) system as shown in Figure 1.3 for a raised floor in the PS that was subjected to harmonic and earthquake excitations. The SCF's performance was analyzed based on the system's response to the structure's excitation. There was a reduction in the equipment acceleration even near the fundamental frequency of the PS. The results showed that the increase in the radius of curvature of the SCF's sliding surface decreases

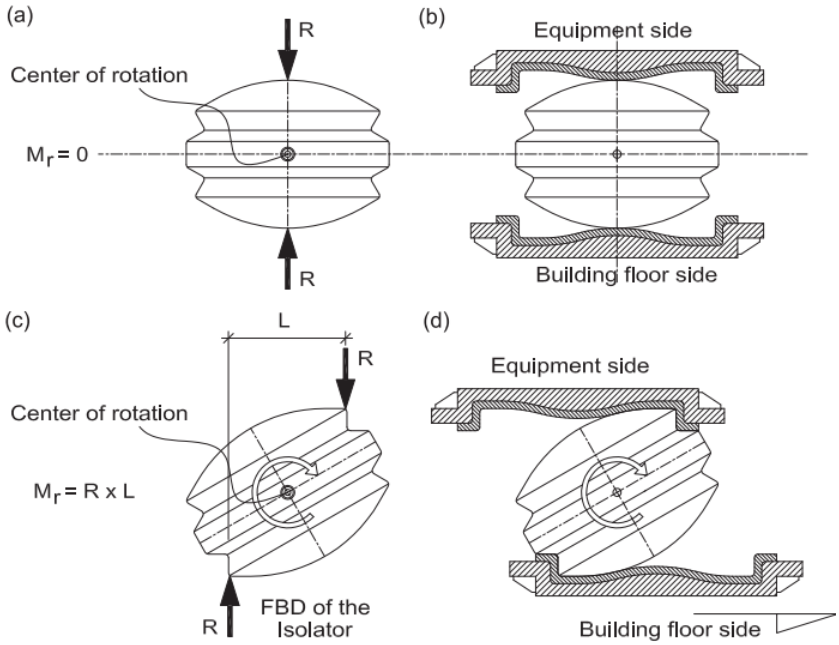


Figure 1.2: RNC isolator. Source: Ismail et al. (2009)

the acceleration response for harmonic excitation. However, the effect of the radius of curvature was shown to be negligible for earthquake excitations. The overall result of the study indicated that the SCF isolation system is an effective technique for a raised floor system.

Pranesh and Sinha (2000) proposed and experimentally tested a sliding isolation system called variable frequency pendulum isolator (VFPI). This system has proved to behave more effectively than a conventional FPS in resisting earthquake of varying intensities. The experimented result of the VFPI showed that the system is effective at all intensities of excitations which, in this case, refer to El Centro GM scaled by a factor of 0.5 (low intensity), 1.0 (medium intensity) and 2.0 (high intensity). Moreover, the system has been observed to act as both a base isolator and an energy dissipator.

In this section, a few devices that have been used as FISs were discussed. In these studies, good isolation performance was achieved through proper tuning of the system. However, none of these studies considered the PS's response in the design of the FIS. Therefore, the next section will discuss methods of mitigating PS's responses subjected

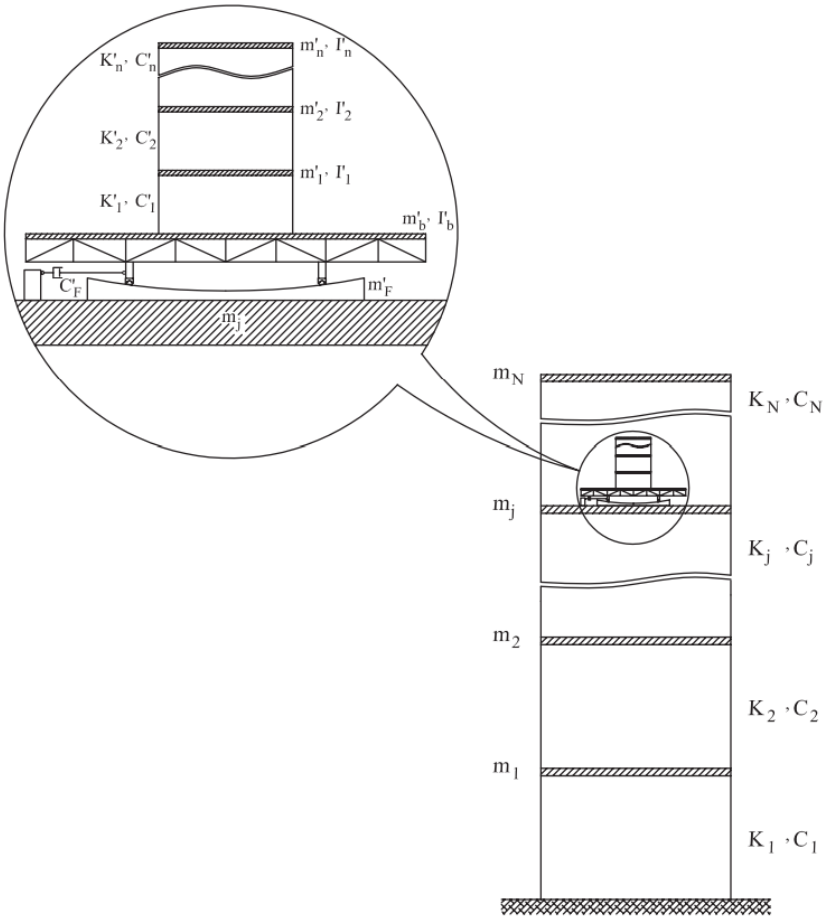


Figure 1.3: SCF on a raised-floor system in a multi-story structure. Source: Hamidi and El Naggar (2007)

to seismic GM.

1.2.2 Vibrational Energy Absorbing System

Structural responses of the PS caused by ground excitations can be mitigated using a vibration energy absorber. As the name implies, this device absorbs (or redistributes) the structure's vibrational energy to help reduce the building responses.

One traditional method to achieve the structure's energy absorption is via the use of tune mass damper (TMD) (Den Hartog, 1985). In Housner et al. (1997), a number of passive energy dissipation control techniques have been discussed. Among those is a TMD which is a type of dynamic vibration absorber (DVA). TMD is a linear approach

to passively dissipate energy of PS consisting of a secondary mass that is about 1 percent of the structure's total mass. It has been well established that TMD is effective in reducing wind-induced structural vibration. In term of seismic control, recent research findings have shown that TMD is most effective for a lightly damped structure and when the structure's frequency is close to the GM's frequency (Murudi and Mane, 2004). Due to the limitation on suppressing broader frequency range, non-linear DVAs are preferred because they can overcome the limitation set by linear DVAs. One type of passive non-linear DVA is the vibro-impact absorber (Nucera et al., 2007). This vibration absorbing system pumps energy when the system experiences impact and dissipates it. This device can effectively dissipate energy from PS and redistribute it to higher-order modes of the structure.

A very common type of DVA is nonlinear energy sink (NES) devices. They have been numerically and experimentally proven to be effective systems in absorbing and dissipating energy of the PS under seismic excitation (Wang et al., 2015a; Luo et al., 2014b). Many types of NES devices have been proposed and studied.

In Wang et al. (2015b), a new type of NES called "track NES" was proposed, with configuration and free body diagram as shown in Figure 1.4. The performance of the track NES was compared to that of a locked system, linear TMD, and Type I NES where it is defined as a single degree of freedom (DOF) NES with nonlinear stiffness and linear damping attachment to the structure (Wierschem et al., 2012). The comparison is based on effective damping and story drift under impulse-like and seismic excitations. As expected, the locked system exhibited the highest displacement and the least energy absorption among the four. The results also showed that the track NES had similar effects on response reduction as Type I NES and could transfer energy from lower mode to the higher mode of the structure. Compared to in-tune TMD, the system was not as effective against seismic excitation, but exhibited robustness against changes

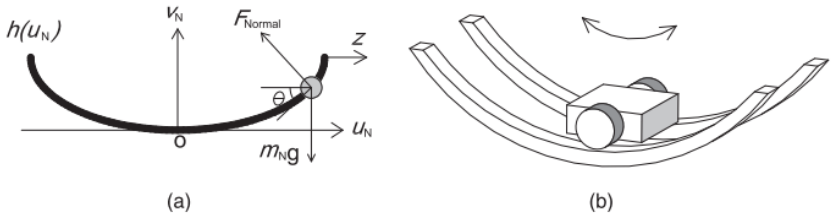


Figure 1.4: Track NES. Source: Wang et al. (2015b)

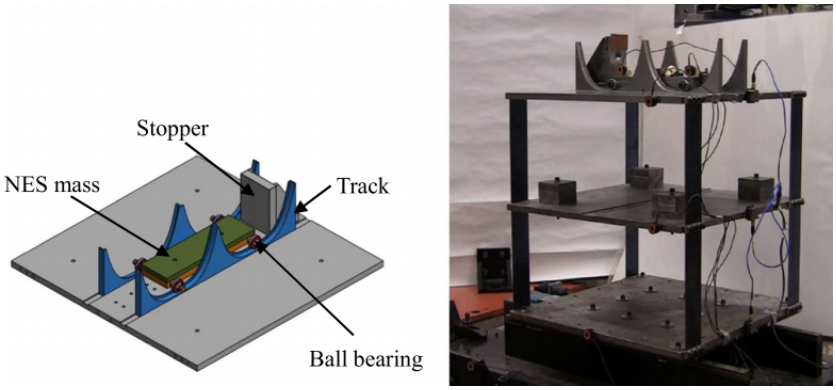


Figure 1.5: SSVI track NES. Source: Wang et al. (2016)

in structural stiffness. Investigated by the same authors, the single-sided vibro-impact track nonlinear energy sink (SSVI track NES) was proposed and studied (Wang et al., 2016). This system is designed by adding an impact stopper on one side of the NES mass for the system, as shown in Figure 1.5, to provide nonlinearity by smooth nonlinear force-distance relationship and discontinuity in restoring force. The experimental results showed that the SSVI track NES is more effective than the track NES in reducing responses and able to reduce peak PS displacement significantly.

In Nucera et al. (2007), the concept of a vibro-impact (VI) NES for mitigating seismic response of a structure was introduced. They numerically simulated the response of the system using four earthquakes — El Centro, Hachino, Kobe, and Northridge — in the N-S direction. The results showed that VI NES generates a redistribution of energy from lower to higher mode of the structure. Due to the requirement for large mass for best performance, VI NES is more effective in transferring momentum when installed at a lower floor. However, NES with smooth nonlinearity are more effective in absorbing

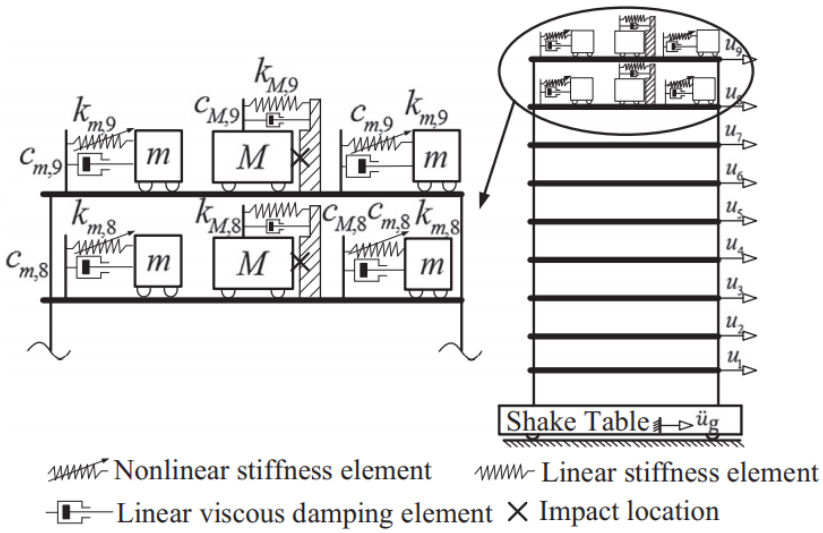


Figure 1.6: Schematic design of the systems on the nine-story structure. Source: Luo et al. (2014b)

seismic energy when attached at a higher floor.

In a research conducted by Luo et al. (2014b), a large-scale experiment and numerical simulation for seismic mitigation has been studied by combining a system of different types of NES devices on a lab-scaled nine-story structure. Two Type I NESs and one SSVI track NES were installed on the eighth and ninth floor as shown in Figure 1.6. The building was subjected to base excitation from the shake table that simulates ground motion of three scaled historic earthquakes. The data exhibited the reduction of both peak and root square mean values of the floor displacement, first-story column strain and base shear. The test showed that the use of the two NES types combined is more effective in suppressing floor acceleration and displacement compared to the case of using SSVI NESs alone. This result indicated that the NES devices can be combined to provide a very effective means of mitigating structural responses.

In this section, linear and nonlinear vibration absorbers were discussed. Nonlinear systems exhibit greater robustness for broader frequency range of GMs compared to the linear systems. By introducing impact, the devices work more effectively in reducing the PS's responses. Next, the concept discussed in Section 1.2.1 and this section will be

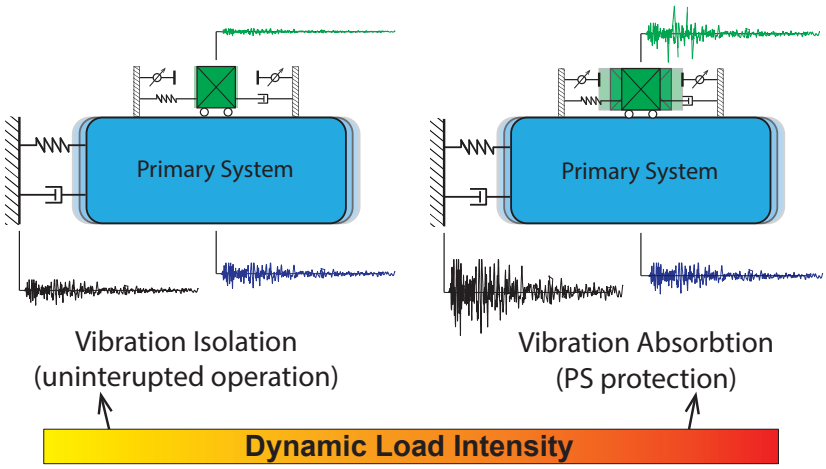


Figure 1.7: Schematic of a dual-mode vibration isolator/absorber system

combined and discussed.

1.2.3 Combined System for Vibration Isolation/Absorption

According to the above sections, seismic isolation systems and vibration absorbers are usually studied and considered separately until the idea of combining them into a single system was proposed and experimentally investigated by Harvey et al. (2018). This system is termed a "dual-mode vibration isolator/absorber system". It was designed to adapt the concept of isolation system during small to moderate disturbance to a vibration absorber during larger disturbance amplitude. The latter was to be achieved via impact at the surface of a metal stopper and the device when the system's displacement capacity exceeded the limitation. The proposed system was tested under harmonic excitation and it showed a promising result in protecting sensitive equipment. However, the system had not been tested and proved effective for seismic GMs.

Reggio and De Angelis (2014) have explored this concept as well but their studies are limited to linear systems. Therefore, nonlinear behaviors of the combined primary-secondary system under seismic excitation still requires further research.

1.3 Summary

In this chapter, previously studied approaches to vibration mitigation of structures were discussed. These included FISs to protect sensitive equipment and vibration absorbers to reduce the response of the PS. Then, the concept of combining the two systems was presented, yet have not been successfully proven to resist seismic excitation. Therefore, this research aims to explore in greater depth the performance of the dual-mode FIS, with a schematic representation shown in Figure 1.7, by using two approaches as described in Chapter 2 and 3.

Chapter 2
Probabilistic Design of a Dual-mode FIS*

2.1 Overview

Seismic isolation is a well-established strategy for suppressing and controlling the inertial loads transferred to buildings and their contents (Naeim and Kelly, 1999; Warn and Ryan, 2012). The basic premise behind seismic isolation is to elongate the natural period, which results in larger displacements and smaller accelerations. This reduction of acceleration results in uninterrupted operation of mission-critical equipment and less downtime following an earthquake, which improves the resilience of the community served (Anajafi and Medina, 2018a). To date, several approaches to protecting sensitive yet vulnerable equipment or other valuable objects housed inside buildings have been used: (1) base isolation of the entire building (Konstantinidis and Nikfar, 2015; Shi et al., 2014; Chen et al., 2016; Ryan et al., 2016), (2) isolating an individual object (Baggio et al., 2015; Tsai et al., 2010; Harvey et al., 2014; Calhoun et al., 2019), and (3) isolating a group of objects (Casey et al., 2018) or a floor inside the building (Lambrou and Constantinou, 1994; Hamidi and El Naggar, 2007; Ismail et al., 2009; Gidaris et al., 2016; Liu and Warn, 2012). There has been a growing interest in the later

*This chapter is based upon work that is currently in press (Bin et al., nd). This was a collaborative effort, with Ms. Bin taking the leading role in performing the numerical simulations, conducting the multi-objective optimization, and writing the manuscript. The nonlinear reduced order modeling technique was first proposed by Dr. Tehrani in his Ph.D. dissertation (Tehrani, 2019), and preliminary numerical modeling of the PS-FIS system in MATLAB was performed by Ms. Nisa. Dr. Taflanidis provided input on the Monte Carlo simulations and multi-objective optimization algorithms, as well as implementation of the model in Simulink.

two approaches—collectively termed *secondary isolation systems* hereinafter—due to the relatively lower cost of implementation, as well as ease of application as a retrofit strategy. Secondary isolation systems are intentionally *detuned* from the fundamental frequency of the supporting building since decoupling of dynamic behavior is necessary and essential for *vibration isolation*. Hence, a common assumption in the assessment and design of secondary isolation systems is that the primary building structure and the isolation system exhibit one-way interaction (Gidaris et al., 2016). Such an assumption of negligible dynamic interaction is justified if the secondary isolation system is detuned and its mass is sufficiently small (Igusa and Der Kiureghian, 1985; Chen and Soong, 1988). The former condition is satisfied by design (see three sentences above), but the latter condition may be invalidated for floor isolation systems (FISs) with large mass ratios. Moreover, it should be noted that these conditions assume *linear* systems, which is *not* true for most isolation system especially when impacts occur (see next paragraph).

Isolation systems can perform extremely well when their displacement demands do not exceed their displacement capacities. When an isolator's displacement capacity is insufficient to meet the demands of a disturbance, the performance of the isolator is diminished because of impacts, giving rise to high acceleration responses in isolated objects (Becker et al., 2017; Andreaus and De Angelis, 2020). Isolation systems can be designed to reduce the likelihood of impacts by increasing displacement capacity (Harvey and Gavin, 2014a; Calhoun et al., 2019) and/or by reducing displacement demands (Harvey et al., 2014). The former may be cost prohibitive or infeasible due to seismic gap limitations (Jia et al., 2014). The latter can be realized through supplemental damping (Kemeny, 1997; Harvey et al., 2014) or a displacement control region at or near the displacement limit (Yang et al., 2020). Recently, a phased approach to supplementing damping at large displacements had been proposed (Zargar et al., 2013;

Rawlinson et al., 2015; Zargar et al., 2017), but displacement control regions are more often associated with a stiffening effect (Soni et al., 2011; Lu et al., 2011). While suppressing isolator displacements, this nonlinear stiffening effect will bring the secondary isolation system's period closer to that of the building, potentially coupling the primary and secondary systems' responses. Such stiffening effects are also activated during impacts (Muthukumar and DesRoches, 2006). Non-smooth restoring forces caused by impacts are accompanied by a scattering of the vibration energy into high-frequency modes (Nucera et al., 2007), which is the basic premise behind nonlinear energy sinks (NESs) (Luo et al., 2014a) discussed below.

An alternative solution for vibration mitigation is the *vibration absorber* or tuned mass damper (TMD) (Gutierrez Soto and Adeli, 2013). A TMD consists of a secondary mass that is connected to the primary structure through a spring and/or a damper. As the name implies, the TMD is *tuned* to the natural frequency of the structure. The application of a linear TMD is usually limited by its constant natural frequency. That is, only one targeted mode (per TMD) can be considered for suppression. On the other hand, nonlinear TMDs are able to be tuned for a broader frequency range in the vicinity of the targeted frequency. Recently, nonlinear TMDs with stiffening behavior have gained attention as energy pumping devices or NESs (Gourdon et al., 2007; Luo et al., 2014b; Wang et al., 2020). Another disadvantage of (linear) TMDs is that they require a relatively large mass. Some researchers have proposed using isolated floors (Xiang and Nishitani, 2014; Engle et al., 2015; Anajafi and Medina, 2018b), stories (Ziyaeifar and Noguchi, 1998; Reggio and De Angelis, 2015), or other massive components (Matta and De Stefano, 2009) as TMDs, leveraging the mass that is already present in the structure and requiring no additional weight (dead load). Whereas TMDs are more established for reducing wind induced vibrations, TMDs with large mass (De Angelis et al., 2012) and/or engineered nonlinearities (Wang et al., 2020) hold promise for seismic mitigation

as well.

Both secondary isolation systems and vibration absorbers involve a secondary system supported by the primary structure (PS), but these two approaches differ in their function. Isolation systems protect the isolated objects, whereas vibration absorbers protect the supporting PS. Other researchers have looked at using FISs for both vibration isolation and vibration absorption, but they have either not taken the PS response into consideration in the design or assumed linear systems. For example, Reggio and De Angelis (2013) modeled and tested a hysteretic FIS incorporating the coupling between the supporting structure and the FIS. The results of that study showed that the FIS had an advantageous effect on the supporting structure's response, even though their dual-criteria focused only on the FIS response. In a follow-on study, Reggio and De Angelis (2014) optimized the combined primary-secondary system performance, this time including PS response criteria, but this analysis was performed on the linearized system with a stochastic design process (i.e., assuming filtered Gaussian white noise excitation and using response variance as a metric). Similarly, Anajafi and Medina (2018b) designed partial mass isolation systems considering both PS and FIS responses, but they likewise assumed a linear system, stochastic excitation, and root-mean-square criteria. The problem with designing a FIS for both vibration isolation and absorption in this way is that there is a trade-off between isolation performance and PS response reduction, which is independent of the excitation intensity. Therefore, vibration isolation performance will be sacrificed at service level earthquakes (SLEs) where it is most essential for uninterrupted operation, and vibration absorption performance will be sacrificed at design-basis earthquake (DBE) and up to maximum considered earthquake (MCE) where damage/collapse prevention of the PS is paramount. In this study, these two concepts are merged in a *nonlinear impact-based dual-mode vibration isolator/absorber system*. A single FIS acts as a vibration isolator when the PS motion

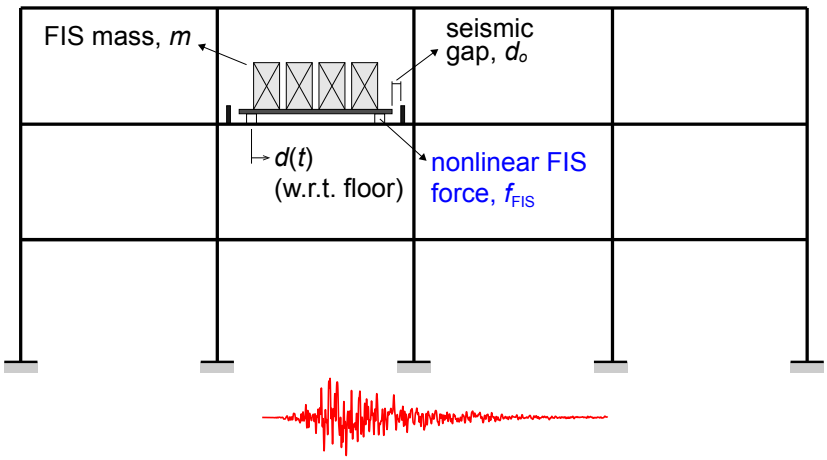


Figure 2.1: Coupled PS-FIS system

is small and as a vibration absorber when the PS motion is large. The displacement-dependent or *phased* transition is achieved by a stiffening nonlinearity or impact. Only with a nonlinear system and a complementary multi-objective, risk-based design criteria can such response-based adaptation be realized.

This chapter investigates the conceptual design of a nonlinear FIS that act as dual-mode vibration isolator/absorber systems. In Section 2.2, a nonlinear reduced order model (NLROM) is formulated for an elastic structure supporting a nonlinear FIS. This NLROM is then used in a multi-objective design problem that is formulated in Section 2.3 to optimize the dual-mode FIS. An illustrative example is presented in Section 2.4, including a parametric study to explore the effects of gap size and impact parameters on the coupled PS-FIS response. Guidelines to the optimal tuning of the dual-mode FIS based on a multi-objective, risk-based design utilizing a Latin hypercube sampling and genetic algorithm are presented in Section 2.5 and 2.6 respectively, followed by concluding remarks in Section 2.7.

2.2 Mathematical Model of the Coupled PS-FIS System

2.2.1 Non-linear Reduced Order Model (NLROM) via Component Mode Synthesis

Consider a building or primary structure (PS) supporting acceleration-sensitive equipment on the jth level. To protect the equipment, a floor isolation system (FIS) is used to isolate a portion of the jth level—either on a raised floor or isolated floor slab—as shown in Figure 2.1. The isolated mass is given by $m = \mu M_j$, where μ is the proportion of the jth level's total mass M_j that is isolated. The PS is modeled by n degrees of freedom (DOFs), represented by $\mathbf{q}(t) \in \mathbb{R}^n$, which may include lateral displacements, vertical displacements, and rotations; the FIS is modeled by its lateral displacement $d(t)$ relative to the story level on which it is mounted. The dynamics of the coupled PS-FIS system is given by the following $n + 1$ equations:

$$(\mathbf{M} - m\mathbf{p}\mathbf{p}^{\mathrm{T}})\ddot{\mathbf{q}}(t) + \mathbf{C}\dot{\mathbf{q}}(t) + \mathbf{K}\mathbf{q}(t) = -(\mathbf{M} - m\mathbf{p}\mathbf{p}^{\mathrm{T}})\boldsymbol{\iota}\ddot{u}_{\mathrm{g}}(t) + \mathbf{p}f_{\mathrm{FIS}} \tag{2.1a}$$

$$m\ddot{d}(t) + f_{\mathrm{FIS}} = -m\mathbf{p}^{\mathrm{T}}(\ddot{\mathbf{q}}(t) + \boldsymbol{\iota}\ddot{u}_{\mathrm{g}}(t)) \tag{2.1b}$$

where $\mathbf{M}$, $\mathbf{C}$, and $\mathbf{K}$ are the $n \times n$ mass, damping, and (linear-elastic) stiffness matrices, respectively; $\boldsymbol{\iota}$ is the n-dimensional influence vector that applies the horizontal ground-motion acceleration, $\ddot{u}_{\mathrm{g}}(t)$, to the lateral nodal displacements; $\mathbf{p}$ is the Boolean n-vector identifying the FIS position in the PS; and $f_{\mathrm{FIS}} \equiv f_{\mathrm{FIS}}(d(t), \dot{d}(t))$ is the nonlinear isolator force, coupling the PS and FIS, the form of which will be discussed in Section 2.2.2. Note that the mass matrix $\mathbf{M}$ appearing in Equation (2.1a) represents the mass matrix of the PS *including* the mass m to be isolated; it is written in this way to emphasize that this formulation assumes that the total mass within the PS-FIS system is conserved.

Equation (2.1) represents the *full coupled model* of the PS-FIS system, including all nonlinear interactions. To ease the computational burden of analyzing the full coupled model [Equation (2.1)], the PS portion of the coupled model can be transformed into

its modal coordinates while keeping the secondary system of equations in the nonlinear reduced order model (NLROM). Transformation to the modal coordinates is performed using r ($\ll n$) selected frequencies ($\omega_1, \ldots, \omega_r$) and associated mode shapes ($\boldsymbol{\phi}_1, \ldots, \boldsymbol{\phi}_r$) of the PS, i.e., $\mathbf{K}\boldsymbol{\phi}_i = \omega_i^2(\mathbf{M} - m\mathbf{p}\mathbf{p}^{\mathrm{T}})\boldsymbol{\phi}_i$. These r modes are selected based on the modal participation factors $\Gamma_i \equiv \boldsymbol{\phi}_i^{\mathrm{T}}\mathbf{M}\boldsymbol{\iota}$ to capture the modes with the highest contribution to the lateral response (Tehrani et al., 2018). The selected mode shapes are assembled into the reduced modal matrix $\boldsymbol{\Phi}_r = [\boldsymbol{\phi}_1, \ldots, \boldsymbol{\phi}_r] \in \mathbb{R}^{n\times r}$. The responses of the PS is then approximated by only these r modes:

$$\mathbf{q}(t) \approx \boldsymbol{\Phi}_r \boldsymbol{\eta}(t) \tag{2.2}$$

where $\boldsymbol{\eta} = [\eta_1, \ldots, \eta_r]^{\mathrm{T}}$ are the modal coordinates. Using the PS modes (or "component modes"), Equation (2.1) can be approximated as follows:

$$\hat{\mathbf{M}}\ddot{\boldsymbol{\eta}}(t) + \hat{\mathbf{C}}\dot{\boldsymbol{\eta}}(t) + \hat{\mathbf{K}}\boldsymbol{\eta}(t) = -\hat{\boldsymbol{\Gamma}}\ddot{u}_{\mathrm{g}}(t) + \hat{\mathbf{p}} f_{\mathrm{FIS}} \tag{2.3a}$$

$$m\ddot{d}(t) + f_{\mathrm{FIS}} = -m(\hat{\mathbf{p}}^{\mathrm{T}}\ddot{\boldsymbol{\eta}}(t) + \ddot{u}_{\mathrm{g}}(t)) \tag{2.3b}$$

where the condensed matrices and vectors are given by

$$\hat{\mathbf{M}} = \boldsymbol{\Phi}_r^{\mathrm{T}}(\mathbf{M} - m\mathbf{p}\mathbf{p}^{\mathrm{T}})\boldsymbol{\Phi}_r,\ \hat{\mathbf{C}} = \boldsymbol{\Phi}_r^{\mathrm{T}}\mathbf{C}\boldsymbol{\Phi}_r,\ \hat{\mathbf{K}} = \boldsymbol{\Phi}_r^{\mathrm{T}}\mathbf{K}\boldsymbol{\Phi}_r,\ \hat{\boldsymbol{\Gamma}} = \boldsymbol{\Phi}_r^{\mathrm{T}}(\mathbf{M} - m\mathbf{p}\mathbf{p}^{\mathrm{T}})\boldsymbol{\iota},\ \hat{\mathbf{p}} = \boldsymbol{\Phi}_r^{\mathrm{T}}\mathbf{p}$$

and the relation $\mathbf{p}^{\mathrm{T}}\boldsymbol{\iota} = 1$ (i.e., the FIS is attached at a horizontal DOF) has been applied.

Equation (2.3) represents the NLROM from component mode analysis, for which the PS has been reduced to modal coordinates and the (nonlinear) coupling to the secondary FIS has been retained. Equation (2.3) is integrated to determine $\boldsymbol{\eta}(t)$ and $d(t)$, from which the PS response is reconstructed from Equation (2.2). The specific form of of the nonlinear coupling force is described in the next section.

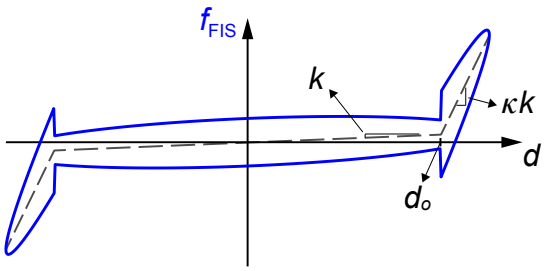


Figure 2.2: Nonlinear force-displacement relationship assumed for the FIS force f_{FIS}

2.2.2 Nonlinear FIS model

The *phased* FIS force is represented by f_{FIS}. This force is comprised of a linear regime, parameterized by stiffness k and damping coefficient c, up to a displacement of d_o. Beyond d_o, the force-displacement relation changes. The specific form of the force beyond d_o can be modeled considering different combinations of linear or nonlinear spring and damping mechanisms (Zargar et al., 2013). In this study, a Kelvin impact model (Muthukumar and DesRoches, 2006) is considered, and the FIS force takes the following form:

$$f_{FIS} \equiv f_{FIS}(d(t), \dot{d}(t)) = \begin{cases} c\dot{d}(t) + kd(t), & |d(t)| \leqslant d_o \\ \chi c\dot{d}(t) + kd(t) + (\kappa - 1)kd(t)[1 - d_o/|d(t)|], & |d(t)| > d_o \end{cases} \quad (2.4)$$

where d_o, κ, and χ are the engagement displacement, stiffening parameter, and damping parameter, respectively. Figure 2.2 presents the phased force-displacement relationship. This model can represent either a harsh impact with a restraining wall (i.e., d_o = seismic gap (Hughes and Mosqueda, 2020)) or a gap at which a supplemental device is activated (e.g., dual-mode system (Tehrani and Harvey, 2019), such as a gap damper Zargar et al. (2017)).

To better illustrate how the parameters κ and χ affect the phased force-displacement relationship, the response of the FIS under harmonic displacement with increasing amplitude (Figure 2.3A) applied to the system is illustrated in Figures 2.3B and 2.3C for damping parameter $\chi = 1$ and 10, respectively, for various stiffening parameter κ. The

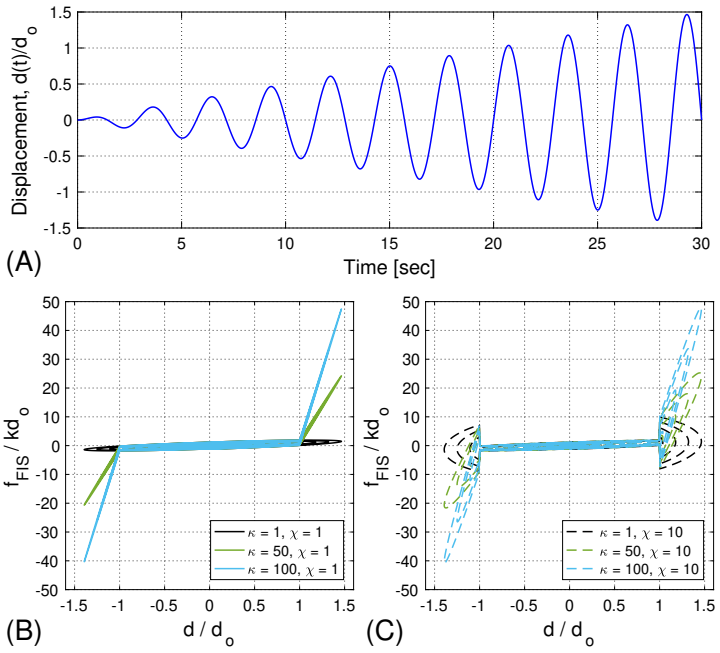


Figure 2.3: Force-displacement relationships of the FIS under harmonic displacement with increasing amplitude (A) for various stiffness parameter $\kappa = 1$, 50, and 100 and damping parameter $\chi =$ (B) 1 and (C) 10.

displacement is normalized by the engagement displacement d_o, and the force f_{FIS} is normalized by the linear restoring force at the engagement displacement (i.e., kd_o). The two values of the damping parameter considered correspond to no additional damping at engagement ($\chi = 1$) and 10 times more damping ($\chi = 10$); these represent elastic and inelastic "impacts," respectively. By adjusting the stiffening parameter κ, the impact can be more ($\kappa = 100$) or less ($\kappa = 1$) harsh. The effect of these parameters on the PS and FIS responses will be explored later in greater detail.

2.3 Multi-Objective Design Problem Formulation

2.3.1 Response Quantities and Evaluation Criteria

In order to evaluate and optimize the PS-FIS performance, the evaluation criteria are divided into two categories. The first category of the evaluation criteria is related to the FIS response. For the FIS, the *peak* response quantities of interest are based on the displacement $d(t)$ across the isolation system and the total acceleration $a(t)$ transmitted

to the isolated equipment:

$$d_{\max} = \max_t |d(t)| \equiv \text{peak relative displacement of FIS} \tag{2.5a}$$

$$a_{\max} = \max_t |a(t)| \equiv \text{peak total acceleration of FIS} \tag{2.5b}$$

Furthermore, let a_{thresh} denote a threshold acceleration limit state for the protected (isolated) objects. Ideally, good vibration isolation performance ($a_{\max} \leqslant a_{\text{thresh}}$) with a low occurrence of impacts ($d_{\max} < d_o$) is observed for low-to-moderate intensity shaking [i.e., service level earthquake (SLE)], at which uninterrupted operation of the equipment is desirable. As such, the first evaluation criterion is given by

$$J^{\text{FIS}}_{\text{accel}} = \mathbb{P}[a_{\max} \geqslant a_{\text{thresh}} | \text{SLE}, \boldsymbol{x}] \equiv \text{FIS failure probability} \tag{2.6}$$

where $\mathbb{P}[\cdot|\text{SLE}, \boldsymbol{x}]$ is the probability conditional on the design variables $\boldsymbol{x}$ (discussed later) under a SLE.

The second category of the evaluation criteria is related to the PS response. For the PS, the peak response quantities of interest are based on the inter-story drift ratio $\delta_j(t)$ in the jth story and the roof drift ratio $\Delta(t)$:

$$\delta_{\max} = \max_{j,t} |\delta_j(t)| \equiv \text{largest peak inter-story drift ratio} \tag{2.7a}$$

$$\Delta_{\max} = \max_t |\Delta(t)| \equiv \text{peak roof drift ratio} \tag{2.7b}$$

Ideally, good vibration absorption performance (i.e., reduced $\delta_{\max}$) is realized at high intensity shaking [i.e., maximum considered earthquake (MCE)], at which life safety is of utmost concern, to achieve damage/collapse prevention of the PS. Therefore, the second evaluation criterion is given by

$$J^{\text{PS}}_{\text{drift}} = \mathbb{P}[\delta_{\max} \geqslant \delta_{\text{thresh}} | \text{MCE}, \boldsymbol{x}] \equiv \text{PS failure probability} \tag{2.8}$$

where δ_{thresh} is a threshold inter-story drift ratio at which damage is expected. An additional response quantity is based on the total acceleration $a^{\text{PS}}(t)$ of the story level of the

PS on which the FIS is installed:

$$a^{\text{PS}}_{\text{max}} = \max_{t} |a^{\text{PS}}(t)| \equiv \text{peak total acceleration of story level of PS} \tag{2.9}$$

This quantity serves as a reference for determining the *transmissibility* reduction afforded by the FIS, i.e., TR = $a^{\text{PS}}_{\text{max}}/a_{\text{max}}$.

Note that, in this study, the response quantities and evaluation criteria are based on *peak* responses, as opposed to norm-based metrics [i.e., root-mean squared (RMS) responses]. While norm-based criteria are common in evaluating the performance of TMDs and NESs (Fu and Johnson, 2011; Wang et al., 2015a; Anajafi and Medina, 2018b), the decision to use peak responses was made to avoid artificially exaggerating the performance gains afforded by the dual-mode FIS, as peak responses are generally of greater concern in seismic design.

2.3.2 Dual-mode FIS optimization

The response quantities and evaluation criteria defined in the previous section are used to quantify the performance of a *dual-mode* FIS installed within a multi-story PS. To reiterate from before, vibration isolation ($a_{\text{max}} \leqslant a_{\text{thresh}}$) is desired at the SLE, and vibration absorption ($\delta_{\text{max}} \leqslant \delta_{\text{thresh}}$) is sought at the MCE. Ultimately, the mathematical description for the multi-objective, risk-targeted design problem is as follows:

$$\boldsymbol{x}^{*} = \arg\min_{\boldsymbol{x}\in\mathcal{X}} \left\{ J^{\text{FIS}}_{\text{accel}}, J^{\text{PS}}_{\text{drift}} \right\} \tag{2.10}$$

where the evaluation criteria $J^{\text{FIS}}_{\text{accel}}$ (Equation (2.6)) and $J^{\text{PS}}_{\text{drift}}$ (Equation (2.8)) depend on the design variables $\boldsymbol{x} = [d_o, \kappa, \chi]$. This is to say that the PS properties (**M**, **C**, **K**) and FIS linear parameters (m, c, k), as well as its location within the structure (**p**), are fixed quantities. The admissible design space $\mathcal{X}$ is defined later for the illustrative example.

The solution of the multi-objective design problem involves evaluating the probabilistic quantities of the evaluation criteria at two hazard levels, $\mathcal{H} \in \{\text{SLE}, \text{MCE}\}$.

These quantities can be estimated through Monte Carlo simulation using a suite of N risk-targeted ground-motions $\ddot{u}_g^{(i)}$, $i = 1, \ldots, N$ (see Section 2.4.2):

$$\mathbb{P}[z \geqslant z_{\text{thresh}} | \mathcal{H}, \boldsymbol{x}] \approx \frac{1}{N} \sum_{i=1}^{N} \mathbb{I}_{z \geqslant z_{\text{thresh}}}(\ddot{u}_{\text{g}}^{(i)}, \boldsymbol{x}) \tag{2.11}$$

where $\mathbb{I}_{z \geqslant z_{\text{thresh}}}(\ddot{u}_{\text{g}}^{(i)}, \boldsymbol{x})$ is the indicator function of failure, which equals to unity if the system with parameters $\boldsymbol{x}$ subject to ground motion $\ddot{u}_{\text{g}}^{(i)}$ fails [i.e., peak response quantity z (here, $a_{\max}$ or $\delta_{\max}$) exceeds the defined threshold z_{thresh}] and zero if it does not. To address challenges in the optimization associated with the discontinuous characteristics of the indicator function, and following recommendations of Taflanidis and Beck (2008), this function is replaced with a lognormal distribution as follows:

$$\mathbb{I}_{z \geqslant z_{\text{thresh}}}(\ddot{u}_{\text{g}}^{(i)}, \boldsymbol{x}) \rightarrow \Phi[\ln(z/z_{\text{thresh}})/\beta] \tag{2.12}$$

where $\Phi[\cdot]$ is the standard Gaussian cumulative distribution function. The logarithmic standard deviation β is taken to be sufficiently small (0.05 unless otherwise noted) to not affect the optimal design but simply get better optimization behavior and/or performance characterization (Taflanidis and Beck, 2008). The optimization is performed in a random search pattern (see Section 2.5) in order to permit a better understanding of the design variables and objective function characteristics on the desired passive displacement-dependent transition from vibration isolation to vibration absorption. An exhaustive parametric search, which is eased by the NLROM, is used to determine the optimal Pareto front of the dominant designs that represent different compromises between the multi-objective criteria. A design is termed *dominant*, and belongs in the Pareto front, if there is no other design that can simultaneously improve upon both competing objectives. In the following sections, the results of the parametric study and multi-objective design are illustrated for the 3-story benchmark building under earthquake loading.

2.4 Illustrative Example

2.4.1 Description of the PS-FIS model considered

The 3-story seismically excited benchmark building (Ohtori et al., 2004) is adopted as the PS for this study. This benchmark building, which is 11.89 m in elevation and 36.85 m by 84.87 m in plan, represents a typical design for Los Angeles, CA, and it utilizes a steel perimeter moment-resisting frames (MRFs) as its lateral load-resisting system. The structure is modeled using elastic Euler-Bernoulli beam elements with a total of $n = 45$ DOFs. The masses of the structure are the same as those for the benchmark structure (Ohtori et al., 2004), and the periods of the first three modes of the PS model are 1.01, 0.33, and 0.17 sec. The FIS is taken to be located on either the 1st, 2nd, or 3rd story level of the PS, isolating $\mu = 1$, 2, 5, 10 and 20% of the existing floor mass (9.57×10^5, 9.57×10^5, or 10.4×10^5 kg, respectively). For each case, the damping matrix $\mathbf{C}$ is determined based on an assumption of Rayleigh damping with 2% damping in the first and second modes ($\zeta_1 = \zeta_3 = 2\%$) (Ohtori et al., 2004) based on the modal properties determined from Equation (2.1a), i.e., $\mathbf{C} = c_1(\mathbf{M} - m\mathbf{p}\mathbf{p}^{\mathrm{T}}) + c_2\mathbf{K}$. The response of the PS-FIS system is shown in Figure 2.4 for a representative case calculated using the full model (Equation (2.1)) and the NLROM (Equation (2.3)) with varying number of retained modes. Going forward, three modes ($r = 3$) are retained in the NLROM, which for this three-story building captures a majority of the response: modal participating mass ratios of 82.8, 13.5, and 3.7% for the case of $\mu = 0$ (i.e., no FIS).

The FIS, which is modeled as a nonlinear SDOF system attached initially to the 2nd level, is taken to have a natural period of 3 sec and damping ratio of 40% in the linear regime ($|d| \leqslant d_o$). These values were selected to give a low probability of failure ($J^{\mathrm{FIS}}_{\mathrm{accel}} \leqslant 2\%$) for a threshold acceleration of $a_{\mathrm{thresh}} = 0.3g$ (Gidaris et al., 2016; Liu and Warn, 2012; IBM, 2014) in the linear range. As previously noted, the impact parameters (κ and

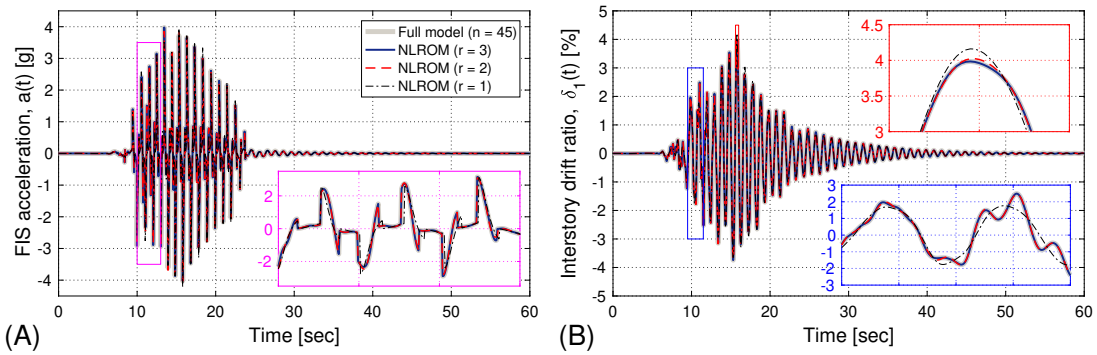


Figure 2.4: Comparison of responses calculated using the full PS model and those using nonlinear reduced order models (NLROMs) with $r = 3$, 2, or 1 mode retained: FIS ($\mu = 5\%$, $d_o = 20.3$ cm, $\kappa = 50$, and $\chi = 10$) installed on the second level of PS subject to a MCE-level GM.

χ) and the gap (d_o) serve as the design variables and are varied in order to investigate their effects on the performance of the PS-FIS system.

Assuming the FIS responds in the linear range, transfer functions for the response quantities can be determined (see Appendix A). These transfer functions are shown in Figure 2.5. From these transfer functions a few observations can be made. First, the FIS is effective at reducing accelerations at forcing frequencies above 0.5 Hz (Figure 2.5B), as desired and expected. Second, these reduced accelerations are associated with large FIS displacements near PS resonance (Figure 2.5A), e.g., 30 to 40 cm of displacement for a 1-Hz excitation with amplitude $0.1g$ (2.5 cm). Third, isolating a portion of the second level's mass has a small effect on the fundamental resonant frequency of the PS, e.g., 3% increase in frequency for the largest mass ratio ($\mu = 20\%$); this is expected because the FIS is sufficiently detuned from the PS and the mass ratios are relatively small (Igusa and Der Kiureghian, 1985; Chen and Soong, 1988). Fourth, isolating a portion of the second level's mass has an effect on the PS response—both maximum inter-story drift (Figure 2.5C) and roof drift (Figure 2.5D)—when compared to the PS without isolation ($\mu = 0$). This effect on the fundamental PS mode is more or less pronounced when mass is isolated from, respectively, the third or first level (not shown). In summary, these linear harmonic results show that there is an inherent benefit to isolating

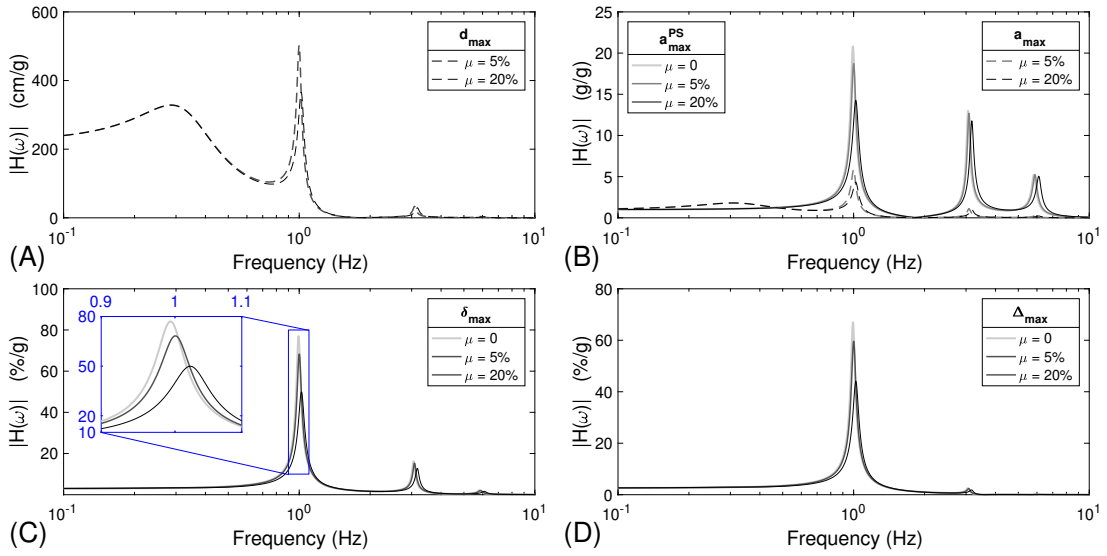


Figure 2.5: Transfer functions from ground acceleration to (A) FIS displacement $d_{\max}$, (B) FIS acceleration $a_{\max}$ and story level acceleration $a^{\text{PS}}_{\max}$, (C) maximum inter-story drift $\delta_{\max}$, and (D) roof drift $\Delta_{\max}$ for varying isolated mass ratios: $\mu = 0$ (no isolation), 5%, and 20%.

a portion of the second level's mass, and the benefit to the PS is greater for higher mass ratios. These results are corroborated for the seismic excitations discussed later.

2.4.2 Seismic excitations

In order to evaluate and design the dual-mode FIS, the PS-FIS system [Equation (2.3)] is excited by a suite of earthquake ground motions (GMs). Fifty uniform-hazard GMs are synthesized representing a 10% probability of exceedance in 50 years (DBE) for a site in Los Angeles, CA for a site class D (firm soil) (Gavin and Dickinson, 2011). These synthetic GMs were generated using a statistical model and are characteristic of the suites of GM records (Foutch, 2000) developed for the SAC Steel Project (1994). The 5%-damped acceleration response spectra for the historic and synthetic GMs are presented in Figure 2.6. The individual spectra are presented, as well as their mean and mean plus/minus one standard deviation. The synthesized GM records and spectra shown in Figure 2.6 represent a DBE-level event. These GM records are scaled by factors of 0.5 and 1.5 to represent SLE and MCE hazards, respectively (ASCE, 2017).

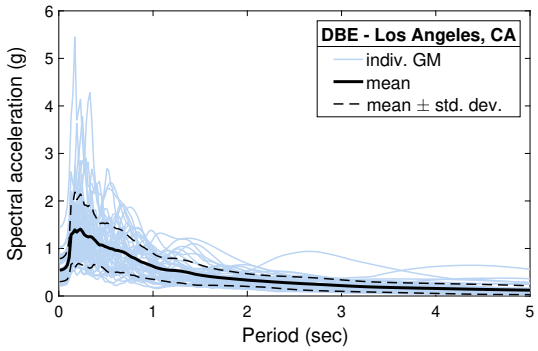


Figure 2.6: Response spectra (5% damped) of 50 synthetic ground motions (GMs) used in numerical study, including mean and one standard deviation.

2.4.2(a) A note on scalability

Although Equation (2.3) constitutes a *nonlinear* PS-FIS system, an important scaling law still holds because of the specific form of the FIS force assumed in Equation (2.4). Namely, the response of a PS-FIS system having a gap of d_o subject to excitation $\ddot{u}_g(t)$ will be proportional—with constant of proportionality $1/\lambda$—to the response of a different PS-FIS system having a gap of λd_o subject to the scaled excitation $\lambda\ddot{u}_g(t)$. This of course assumes all other parameters are held constant, and the PS is linear elastic. This scaling law will prove valuable in the parametric study (Section 2.4.4) because the responses under the suite of DBE-scaled GMs for a range of gaps, say $d_o \in [2.54, 76.2]$ cm, can simply be scaled by 0.5 and 1.5 to generate results under the SLE- and MCE-scaled GMs, respectively, for gaps of $d_o \in [1.27, 38.1]$ and $[3.81, 114.3]$ cm, respectively. Likewise, this would be beneficial for enumerative techniques to the optimal design, whereby a large parametric design space is exhaustively explored. In the multi-objective design, evaluation of the fitness function [Equation (2.10)] for an individual nevertheless requires two simulations—once at SLE and once at MCE—for the same gap value. It may be possible to incorporate this scaling law into the framework using a similar rationale, but doing so is outside the scope of this work.

2.4.3 Baseline (linear) performance

In order to evaluate the performance of an FIS system as an isolator and absorber, it is important to look at the baseline performances of the system as shown in Figure 2.7. These include the peak FIS displacement, peak accelerations, peak inter-story drift ratio, and peak roof drift ratio for the linear PS-FIS system. The structural responses of different mass ratios (1, 2, 5, 10 and 20%) are generated under DBE-scaled GMs. Additionally, the case of no FIS in which the sensitive equipment is *rigidly* attached to the structure is considered for comparison.

Empirical cumulative probabilities for each of the peak response quantities are illustrated in Figure 2.7. From 2.7A, it is apparent that higher mass ratios exhibit marginally lower peak FIS displacements. Figure 2.7B shows two groups of lines: one representing the peak acceleration $a_{\max}$ of the FIS and another representing the peak acceleration $a_{\max}^{\mathrm{PS}}$ of the second level of the PS on which the FIS is installed. The figure shows that, with an FIS attached to the second level, the median acceleration of the building contents can be dramatically reduced from $1.2g$ to $0.3g$. In terms of acceleration, an increase in mass ratio does not necessarily correspond to smaller accelerations. Figures 2.7C and 2.7D show a reduction in peak inter-story drift ratio $\delta_{\max}$ and peak roof drift ratio $\Delta_{\max}$, respectively, with an increase in mass ratio.

According to Figures 2.7C and 2.7D, the attachment of an FIS system to the second level of the PS has shown promising result in mitigating the response of the PS under linear motion. The average reductions in peak inter-story drift ratios, peak roof drift ratios, and base shear are shown in Table 2.1. In this table, the percent reduction increases with higher mass ratios. With a large mass ratio of 20%, median peak inter-story drift and peak roof drift are reduced by 12.5 and 10.8%, respectively, when compared to the case of no FIS ("Rigid").

The result of these baseline performances serves as a basic measure to which the

Table 2.1: Average PS response quantities for the linear PS-FIS system with varying mass ratios μ installed on the second level subject to DBE-scaled GMs. The term in brackets is the percent reduction in the response quantities when compared to the case of no FIS ("Rigid").

Response quantity	Mass ratio, μ (%)					
	Rigid	1	2	5	10	20
$\delta_{\max}$ (%)	2.58	2.57 [0.50%]	2.56 [1.00%]	2.52 [2.59%]	2.45 [5.19%]	2.32 [10.2%]
$\Delta_{\max}$ (%)	2.08	2.07 [0.49%]	2.06 [0.99%]	2.03 [2.43%]	1.98 [4.93%]	1.87 [10.0%]
$V_{b,\max}$ (10^3 kN)	21.9	21.8 [0.49%]	21.7 [0.99%]	21.4 [2.41%]	20.9 [4.47%]	20.1 [7.89%]

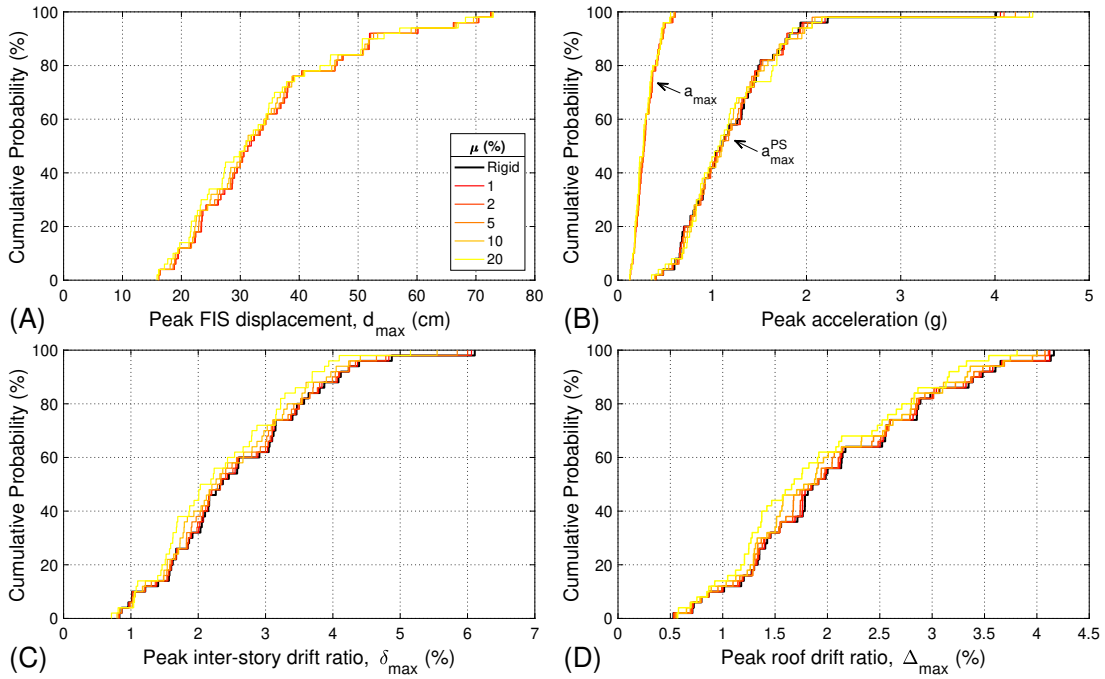


Figure 2.7: Empirical cumulative probabilities of peak responses—(A) FIS displacement, (B) FIS and story level accelerations, (C) inter-story drift ratio, and (D) roof drift ratio—for a linear FIS of varying mass ratio μ installed on the second level subject to DBE-scaled GMs

nonlinear cases will be compared to in the subsequent parametric study.

2.4.4 Parametric study

To illustrate the effects of the multi-functional FIS, some representative results are presented here for the case of $\mu = 5\%$, $\kappa = 50$, and $\chi = 10$ with varying d_o. The effectiveness of the dual-mode vibration isolator/absorber system is characterized by statistics of the response quantities defined in Section 2.3.1. Figures 2.8 and 2.9 show the empirical cumulative probabilities of these peak response quantities for systems with various gaps d_o subject to GMs scaled to SLE and MCE, respectively.

2.4.4(a) Discussion of two cases: linear and $d_o = 20.3$ cm

In Figures 2.8 and 2.9, two cases are highlighted: the linear FIS (i.e., $d_o \to \infty$, or equivalently $\kappa = \chi = 1$) and a FIS with a gap of $d_o = 20.3$ cm. These two cases are discussed in detail here.

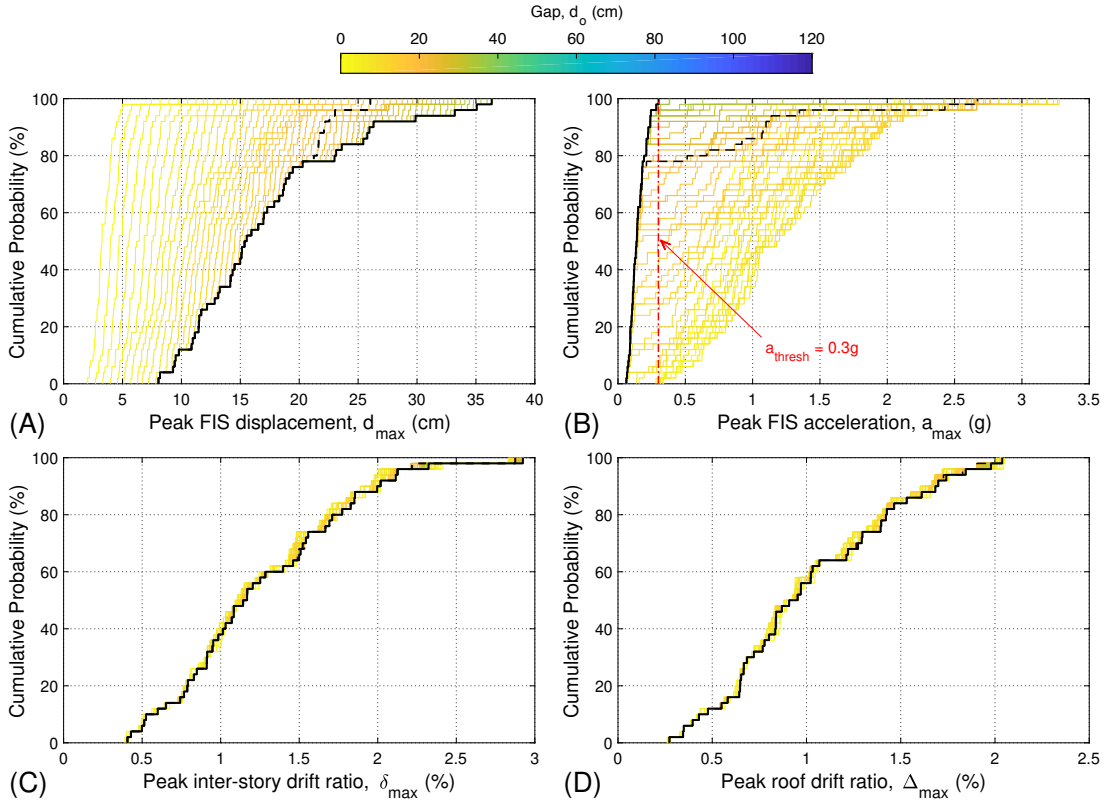


Figure 2.8: Empirical cumulative probabilities of peak responses of PS-FIS systems with various gaps d_o subject to SLE-scaled GMs: $\mu = 5\%$, $\kappa = 50$, and $\chi = 10$. The two highlighted cases are the linear FIS ($d_o \to \infty$; —) and a nonlinear FIS with $d_o = 20.3$ cm (– – –)

Under the SLE-scaled GMs (Figure 2.8), peak displacements (Figure 2.8A) of the linear FIS range from about 8 to 36 cm. For excitations in which $d_{\max} \leqslant 20.3$ cm (about 80% of earthquakes), the two FISs perform identically, but diverge when the displacement demand exceeds 20.3 cm, resulting in a spike in the peak FIS acceleration (Figure 2.8B) up to about $2.5g$. As a point of comparison, the acceleration threshold $a_{\text{thresh}} = 0.3g$ is indicated in Figure 2.8B. The results show that, for the FIS with $d_o = 20.3$ cm, good isolation performance ($a_{\max} \leqslant a_{\text{thresh}}$, i.e., sustained accelerations less than the threshold acceleration) is achieved for about 80% of the SLE-scaled GMs. The linear case always decreases the accelerations because impacts are not encountered; however, this would require a gap of at least 36 cm. There is very little difference in the cumulative probabilities of inter-story drift (Figure 2.8C) and roof drift (Figure 2.8D)

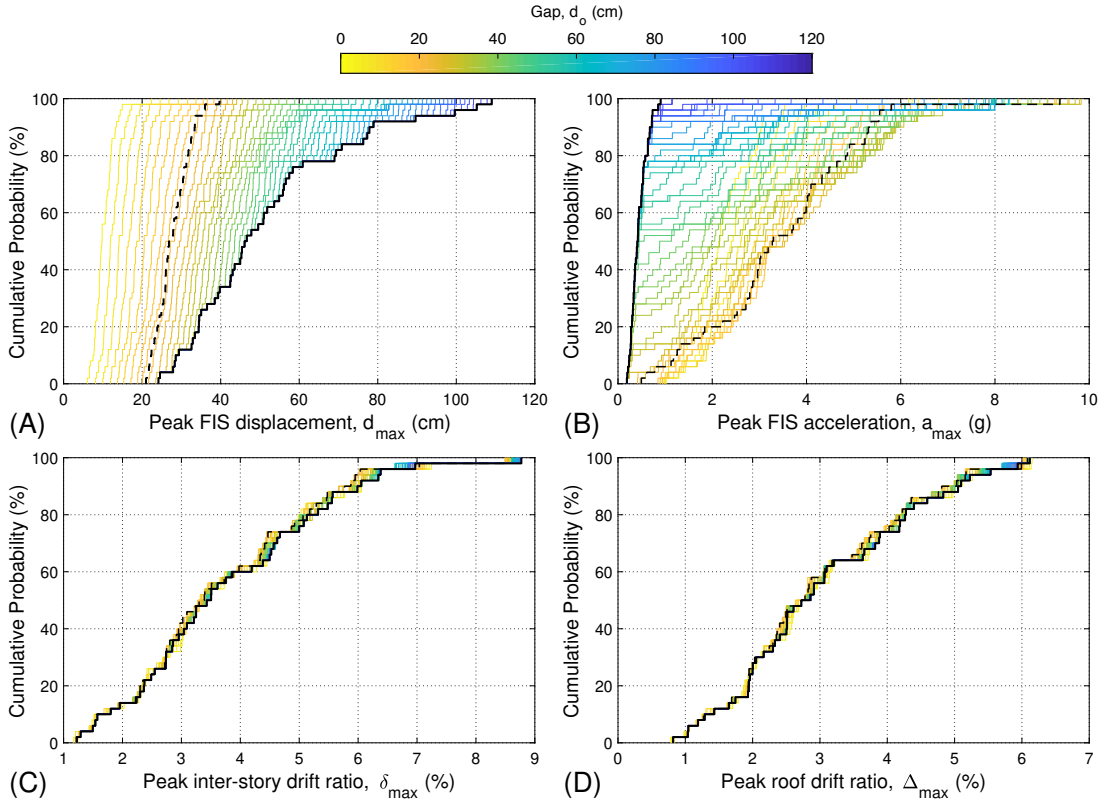


Figure 2.9: Empirical cumulative probabilities of peak responses of PS-FIS systems with various gaps d_o subject to MCE-scaled GMs: $\mu = 5\%$, $\kappa = 50$, and $\chi = 10$. The two highlighted cases are the linear FIS ($d_o \to \infty$; —) and a nonlinear FIS with $d_o = 20.3$ cm (– – –)

in these two cases.

Under the MCE-scaled GMs (Figure 2.9), impacts ($d_{\max} > d_o = 20.3$ cm; Figure 2.9A) are induced in 100% of earthquakes, with accelerations reaching nearly $10g$ (Figure 2.9B). There is a slight difference between the cumulative probabilities of inter-story drift (Figure 2.9C) and roof drift (Figure 2.9D), with the impacting system ($d_o = 20.3$ cm) giving smaller peak drifts. To better illustrate this effect, the cumulative probability of maximum peak inter-story drift is recast using the ratio $\delta_{\max}/\delta_{\max}^{\text{linear}}$ where $\delta_{\max}^{\text{linear}}$ is the peak inter-story drift ratio for the PS-FIS with a linear FIS (i.e., $d_o \to \infty$). This ratio gives a metric for the reduction (< 1) or amplification (> 1) produced by the dual-mode nonlinear FIS. Figure 2.10 shows the cumulative probability of this ratio, again highlighting the case of a FIS with $d_o = 20.3$ cm. Improved PS performance ($\delta_{\max}/\delta_{\max}^{\text{linear}} < 1$)

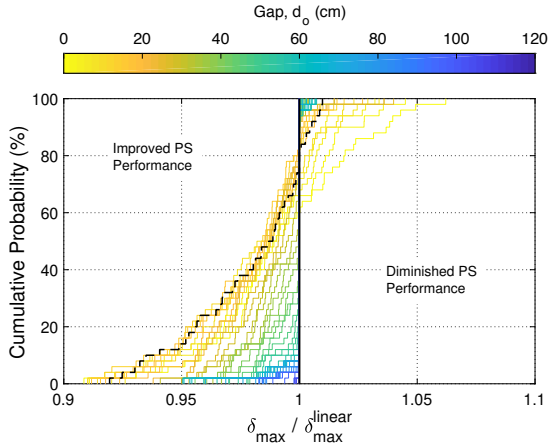


Figure 2.10: Empirical cumulative probabilities of the ratio $\delta_{\max}/\delta_{\max}^{\text{linear}}$ of the peak inter-story drift with FISs of various gaps d_o to the linear FIS, subject to MCE-scaled GMs: $\mu = 5\%$, $\kappa = 50$, and $\chi = 10$. The two highlighted cases are the linear FIS ($d_o \to \infty$; —) and a nonlinear FIS with $d_o = 20.3$ cm (– – –)

is observed in over 75% of earthquakes, with average and maximum drift reductions of 2% and nearly 8%, respectively.

2.4.4(b) Effects of gap d_o and mass ratio μ

The effect of the gap d_o on the peak responses are illustrated for a range of gaps in Figures 2.8 and 2.9 and on the ratio of PS inter-story drift ratio in Figure 2.10. In terms of the FIS response, impacts are observed in more cases for smaller gaps, as is expected. Under MCE-scaled GMs, the resulting increase in peak acceleration (Figure 2.9B) is greatest on average for systems with the intermediate gaps ($d_o \simeq 20.3$ cm); this is because larger velocities are able to be developed in these cases, versus the smaller d_o where impacts occur more frequently but are less severe. The greatest improvements in PS performance (Figure 2.10) is nearly 10% reduction in peak inter-story drift; the greatest decrease in PS performance is about 6% increase in peak inter-story drift for the FIS with smallest gap ($d_o = 3.81$ cm).

To better illustrate the effects of gap d_o on the PS-FIS performance, Figure 2.11 shows how the evaluation criteria $J_{\text{accel}}^{\text{FIS}}$ (Equation (2.6)) and $J_{\text{drift}}^{\text{PS}}$ (Equation (2.8)) vary with d_o for various isolated mass ratio μ. Figure 2.11A shows that the probability of

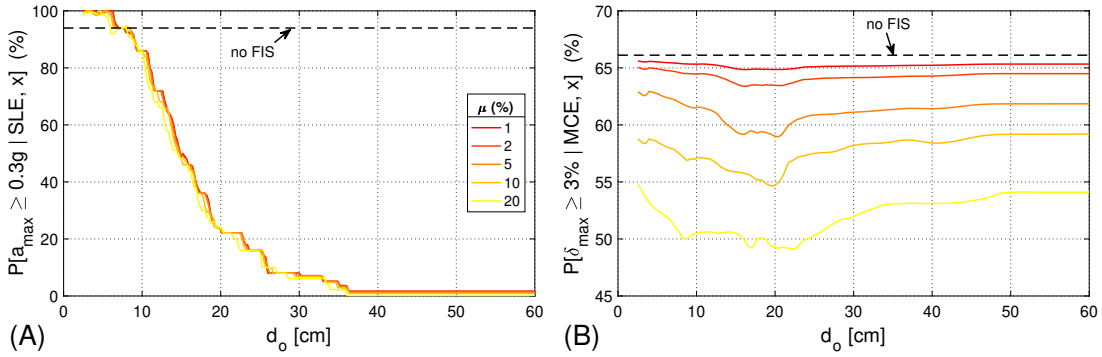


Figure 2.11: Effect of gap d_o on evaluation criteria (A) FIS failure probability and (B) PS failure probability under SLE- and MCE-scaled GMs, respectively, for various isolated mass ratio μ: FIS ($\kappa = 50$ and $\chi = 10$) installed on the second level.

equipment failure ($a_{\max} \geqslant a_{\text{thresh}} = 0.3g$) decreases with increasing d_o. This is expected because larger gaps result in fewer impacts and spikes in acceleration. The greatest sensitivity of $J^{\text{FIS}}_{\text{accel}}$ to d_o is observed for $10 \leqslant d_o \leqslant 25$ cm, indicating that there is a greater advantage in terms of isolation performance for increasing the gap. This is because these d_o values roughly correspond to the steepest portion of the empirical cumulative probability interquartile range of $d_{\max}$ (Figure 2.8A). FISs with gaps $d_o > 7.5$ cm outperform the case of "no FIS," which represents the case in which the sensitive equipment is rigidly attached to the structural floor; hence, in this case, the FIS failure probability is determined using the story level peak acceleration $a^{\text{PS}}_{\max}$ (Equation (2.9)) to calculate $J^{\text{FIS}}_{\text{accel}}$ in Equation (2.6). FISs with gaps $d_o > 36.5$ cm behave as linear systems (Table 2.2) because the peak displacement demand at SLE (Figure 2.8A) is insufficient to cause an impact. The isolated mass ratio μ has little effect on the FIS evaluation criterion.

Figure 2.11B shows $J^{\text{PS}}_{\text{drift}}$, the probability of the maximum peak inter-story drift $\delta_{\max}$ exceeding a threshold of $\delta_{\text{thresh}} = 3\%$ at MCE, for various gaps d_o. With increasing d_o, $J^{\text{PS}}_{\text{drift}}$ decreases at first, reaches a minimum, and then increases, trending toward the values for the linear system (Table 2.2). The presence of a minimum corresponds to an optimal design of the FIS for PS response reduction. The optimal gaps d^*_o are

between 17 and 22 cm for all the mass ratios. These correspond to modest reductions—approximately 0.5% ($\mu = 1\%$) to 5% ($\mu = 20\%$)—reductions in the probability of failure compared to a linear FIS with the same μ; that is, neglecting the inherent reduction from simply isolating the mass (e.g., 12.0% for the case of $\mu = 20\%$, see Table 2.2). It is worth pointing out that distinct local minima are observed, which correspond to optimal gaps that vary by as much as 6 cm but give comparable values for $J^{\text{PS}}_{\text{drift}}$.

Note that the optimal d_o^* values discussed in the previous paragraph consider only the PS evaluation criterion $J^{\text{PS}}_{\text{drift}}$, but do not reflect the isolation performance under SLE hazards. The proper design of a dual-mode impact isolator/absorber FIS needs to consider the vibration isolation performance and whether the accelerations are within acceptable ranges for the sensitive equipment being isolated. For example, for an isolated mass ratio μ of 5% and a gap d_o of 18 cm (i.e., approximately d_o^*), excessive accelerations ($J^{\text{FIS}}_{\text{accel}}$) and equipment failures would be expected in about 25% of cases under the SLE-scaled GMs (Figure 2.11A). Hence, this design does not strictly meet both objectives of a dual-mode vibration isolator/absorber FIS—mitigate accelerations under SLE hazards and provide enhanced PS performance under MCE hazards—constituting a multi-objective design optimization (Equation (2.10)). Such an optimization is presented in the following section.

2.5 Optimization Study

While the previous sections detail the effects of the seismic gap (d_o) on the performance of the FIS and PS, this section studies the effect of other two parameters—stiffening parameter (κ) and damping parameter (χ)—together with d_o to obtain the optimized performance of the PS-FIS system. This optimization study focuses on the the objective functions given by Equations (2.6) and (2.8). Nominal values for the thresholds are $a_{\text{thresh}} = 0.3g$ at SLE and $\delta_{\text{thresh}} = 3\%$ at MCE, which correspond respectively to operational vibration limits of information technology equipment (IBM, 2014) and an

Table 2.2: Performance criteria for the linear PS-FIS system with varying mass ratios μ installed different stories. The term in brackets is the reduction in the failure probability when compared to the case of no FIS ("Rigid").

Objective	Story Level	Mass ratio, μ (%)					
		Rigid	1	2	5	10	20
$\mathbb{P}[a_{\max} \geqslant 0.3g \vert \text{SLE}, \boldsymbol{x}]$ (%)	1st	81.4	0.00 [81.4]	0.00 [81.4]	0.00 [81.4]	0.00 [81.4]	0.00 [81.4]
	2nd	94.0	1.69 [92.3]	1.59 [92.4]	1.34 [92.6]	0.91 [93.1]	0.22 [93.8]
	3rd	91.4	9.93 [81.4]	10.3 [81.0]	11.2 [80.1]	11.9 [79.5]	11.2 [80.2]
$\mathbb{P}[\delta_{\max} \geqslant 3\% \vert \text{MCE}, \boldsymbol{x}]$ (%)	1st	66.1	65.9 [0.26]	65.6 [0.54]	64.5 [1.66]	62.2 [3.93]	58.1 [8.04]
	2nd	66.1	65.3 [0.78]	64.5 [1.62]	61.9 [4.26]	59.2 [6.92]	54.1 [12.0]
	3rd	66.1	64.2 [1.87]	62.3 [3.81]	57.9 [8.24]	54.8 [11.3]	46.8 [19.3]

"extensive" damage state of low-rise steel MRFs (FEMA, 2003). These values are assumed unless otherwise noted.

To approach the optimal design, Latin hypercube sampling is used to generate 25,000 samples for d_o, χ, and κ. The appropriateness of this value for facilitation an efficient exploration of the admissible design space will be examined later. This space for each of these design variables is taken to be $d_o \in [2.54, 60.96]$ cm, $\kappa \in [1, 100]$, and $\chi \in [1, 20]$. The optimization is set to run for 50 GMs at SLE, DBE and MCE, with mass ratios μ = 1, 2, 5, 10, and 20% and the FIS attached to the first, second, and third levels; the nominal case is μ = 5% on the second level. Recall, a lognormal cumulative distribution function is used in the generation of the Pareto front with the nominal lognormal standard deviation value of β = 0.05 (Taflanidis and Beck, 2008), but other values will be considered to assess its influence.

2.5.1 Nominal Case

For the nominal case (Table 2.3), the two objective functions are plotted in Figure 2.12 for all 25,000 sample points in the (d_o, χ, κ) design space. According to Figure 2.12A, a gap d_o from 2.56 to about 12.7 cm exhibits a high probability of failure in the FIS ($J^{\text{FIS}}_{\text{accel}} \geqslant 70\%$), independent of κ and χ. It is observed that as d_o increases, the FIS probability of failure decreases. This makes sense because larger values of d_o corresponds to a reduced chance of impact resulting in a lower probability of FIS failure. The FIS

Table 2.3: Nominal parameters used in the multi-objective optimization study, about which parametric variations are considered.

Variable	Value
Mass ratio, μ [%]	5
Lognormal standard deviation, β	0.05
Acceleration threshold, a_{thresh} [g]	0.3
Inter-story drift ratio threshold, δ_{thresh} [%]	3
Story level on which FIS is installed	2nd

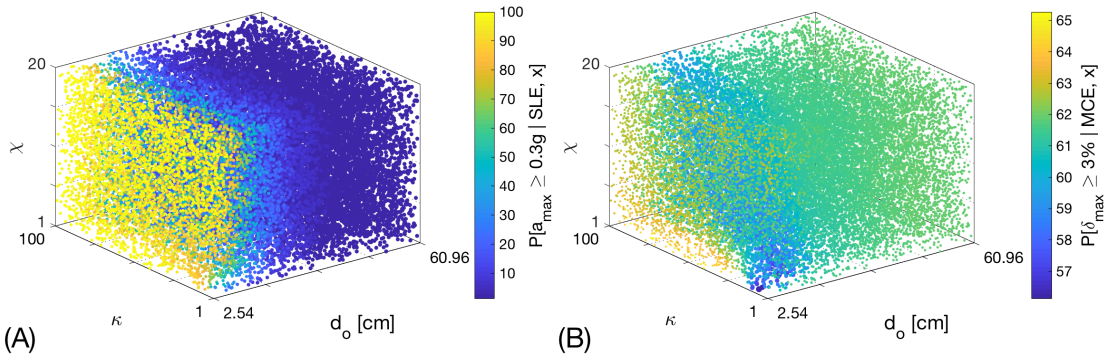


Figure 2.12: (A) Probability of peak FIS acceleration exceeding $a_{\text{thresh}} = 0.3g$ under SLE-scaled GMs, and (B) probability of peak inter-story drift ratio exceeding $\delta_{\text{thresh}} = 3\%$ under MCE-scaled GMs: FIS (μ = 5%) installed on the second level. Note that different color scales are used in (A) and (B) to represent the probabilities.

exhibits the best performance ($J^{\text{FIS}}_{\text{accel}} \leqslant 10\%$) at $d_o \geqslant 36$ cm where the probability is constant (~2%). Referring back to Figure 2.8A, the peak FIS displacement d_{max} is 36 cm. Therefore, it serves as a confirmation that any seismic gap greater than 36 cm should have the same performance (i.e., that of the linear system). However, this value of seismic gap is quite high for practical purposes. An alternative with an acceptable FIS performance ($10\% \leqslant J^{\text{FIS}}_{\text{accel}} \leqslant 40\%$) can be found at the vicinity of $d_o = 20$ cm. Parameters χ and κ seem to have negligible effect in optimizing the FIS performance given how $J^{\text{FIS}}_{\text{accel}}$ is currently defined. In Figure 2.12B, the best PS performance ($J^{\text{PS}}_{\text{drift}} \leqslant 60\%$) is achieved for gaps d_o between 12.7 to 25.4 cm, independent of χ values. However, κ and d_o exhibit an exponential-like relationship, which will be discussed later in the context of the Pareto optimal design parameters. Thus, the best PS performance occurs at small κ values, which correspond to a failure probability of about 57%. From the analysis of Figure 10, for the case of the FIS installed on the second level with $\mu = 5\%$, the optimal design values that minimize the objective functions occur at $d_o \approx 20$ cm and $\kappa \leqslant 10$, independent of χ, which is explored in greater detail below.

Figure 2.13A shows the Pareto front for a FIS installed on the second level with a mass ratio of 5%. The horizontal/vertical lines are plotted for the cases of no FIS and linear FIS so that their performances for each objective function can be compared.

When compared to the case of no FIS, the incorporation of the linear FIS results in a substantial drop in the probability of FIS failure (ordinate) from 95% to about 2%. On the other hand, a small reduction (≈4%) in PS failure probability (abscissa) is observed, indicating that the probability of the PS failure can also be reduced if the linear FIS is installed. The left-most Pareto point gives the best FIS performance (≈ 2% probability of failure) while it has the worst PS performance (≈ 60% probability of failure). The inverse can be said for the right-most point of the Pareto front. These two *anchor points* (the left-most and the right-most points) of a given Pareto front correspond to the single-objective optimums. Moving from left to right along the Pareto front (indicating worse FIS performance), better PS performance is achieved. Therefore, there has to be a trade-off between the two objective functions, and the sacrifice has to be made based on the relative importance of the FIS or PS upon the particular design application. In this case (Figure 2.13), marginal improvements (< 4%) in PS performance are gained only with a substantial reduction (up to 80%) in FIS performance. It should be noted that the sacrifices/gains in PS performance are distorted in Figure 2.13 (and some later figures) because of the different axes scales used to represent the failure probabilities (abscissa and ordinate).

Figure 2.13B shows Pareto optimal design parameters corresponding to the Pareto front in Figure 2.13A. The same coloring scheme is used in both Figures 2.13A and 2.13B so that the Pareto points can be matched up accordingly. It is apparent that χ has little effect on the optimal design of the PS-FIS system, while κ and d_o are influential and clearly exhibit a relationship. Points with good FIS performance (yellow) cluster around $d_o \approx 30$ cm, with variability in κ values. In term of seismic gap, this makes sense because there is a low chance of impact occurring and the system would function primarily as an isolator. However, the variation in κ (about $d_o \approx 30$ cm) does not exhibit an obvious trend of how the stiffening effect affects the FIS and PS performance. Points

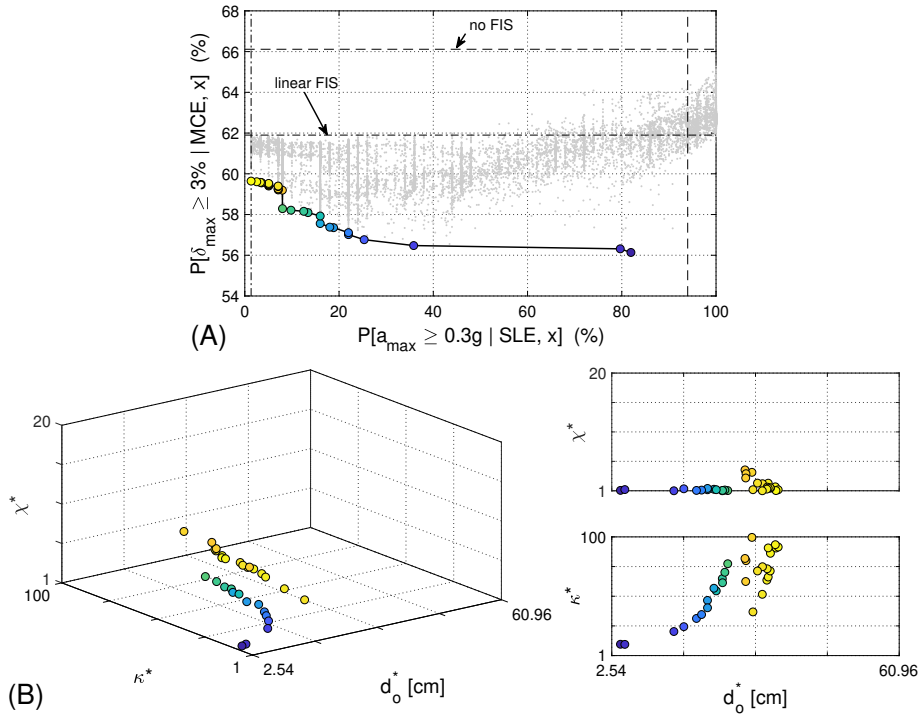


Figure 2.13: (A) Pareto front for a FIS ($\mu = 5\%$) installed on the second level, and (B) Pareto optimal design parameters. The horizontal/vertical lines are for the cases of no FIS (– – –) and linear FIS (– · –), and the gray points are the 25,000 individual samples in the random search. Note that unequal axes scales are used to represent the failure probabilities (A).

with decreasing PS performance spread out in an exponential-like fashion with the best PS performance (blue) occurring at low values of d_o, κ, and χ. It is observed that the optimal gap d_o^* tends towards its lower bound (2.54 cm) with a stiffening parameter κ^* of 10. For such a small gap, the FIS is essentially in a constant state of impact, and the effective stiffness is therefore κk, which in this case corresponds to a FIS period of about 1 sec. This is approximately equal to the fundamental period of the PS. Therefore, the FIS acts like a TMD that is tuned to the PS period. However, at this value (right-most blue points on Figure 2.13A), the equipment has an 80% probability of failure. Thus, to achieve a TMD-functioning FIS, there has to be a considerable sacrifice in isolation performance. Conversely, by sacrificing a small (and questionable) improvement in the PS performance at MCE, there is a significant gain in the FIS performance at SLE, as seen in Figure 2.13A.

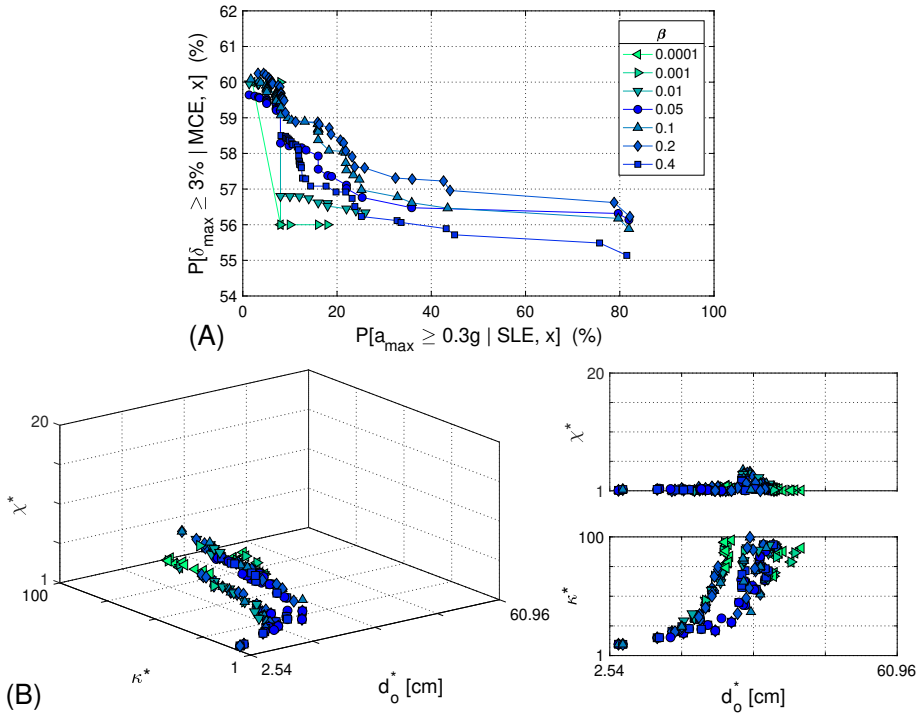


Figure 2.14: Effect of lognormal standard deviation β on (A) Pareto front for a FIS ($\mu = 5\%$) installed on the second level and (B) Pareto optimal design parameters. Note that unequal axes scales are used to represent the failure probabilities (A).

2.5.2 Effect of Lognormal Standard Deviation on Optimal Design

Recalling 0.05 was selected as the nominal lognormal standard deviation, the effect of other β values is shown in Figure 2.14. In Figure 2.14A, the smallest β demonstrates a diminished Pareto front comprised of only two points, and for the next smallest β a step-function characteristic is observed. As β increases, the edges of the Pareto front become smoother and wider and more points are included in the Pareto front. Figure 2.14B shows the scatter in the optimal design space due to different β values. It is observed that these points coincide with nearly identical optimal design parameters. Therefore, it is concluded that β has negligible effect on the optimal design values, and the use of any β value should provide similar results for the optimization.

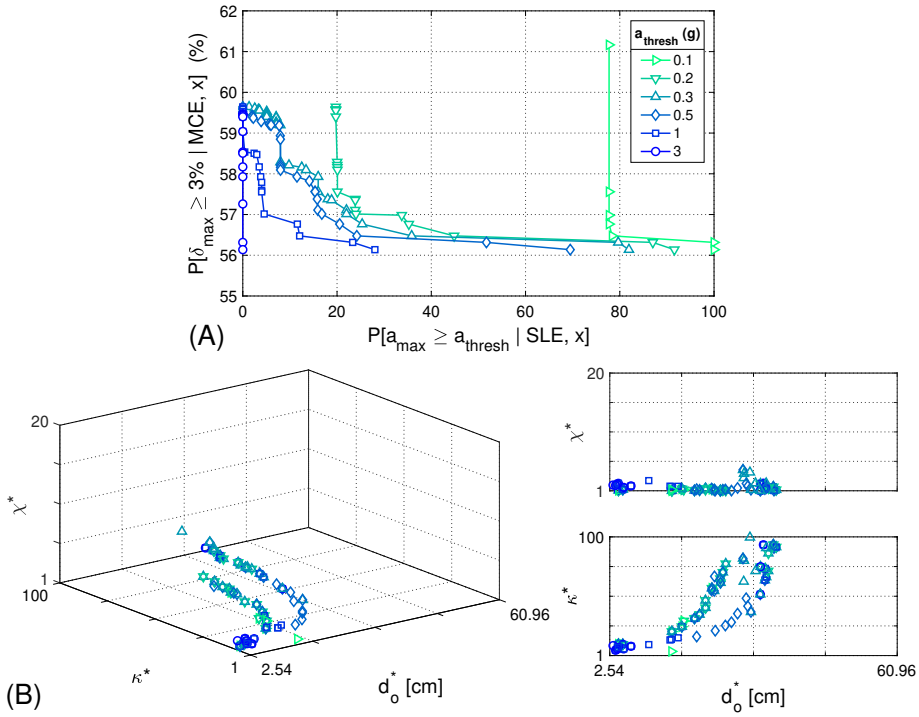


Figure 2.15: Effect of acceleration threshold a_{thresh} on (A) Pareto front for a FIS ($\mu = 5\%$) installed on the second level and (B) Pareto optimal design parameters. Note that unequal axes scales are used to represent the failure probabilities (A).

2.5.3 Effect of Threshold Values on Optimal Design

Figure 2.15 shows the effect of different acceleration thresholds (a_{thresh}) on the Pareto front and the optimal design parameters. The acceleration thresholds considered are related to the sensitivity of the equipment, from $0.1g$ being the most sensitive to $3g$ being the most robust. As shown in Figure 2.15A, there will be a failure in the equipment with $a_{\text{thresh}} = 0.1g$ after a steep drop in $J^{\text{PS}}_{\text{drift}}$ at a FIS failure probability of about 80%; this serves as a lower bound on the achievable FIS performance for very sensitive equipment. As a_{thresh} increases, the lines move to the left indicating lower FIS failure probability. At $a_{\text{thresh}} = 3g$, there is no failure in the equipment and $J^{\text{PS}}_{\text{drift}}$ can be reduced by almost 4%. Figure 2.15B indicates the that different acceleration thresholds do not result in different optimal trends of the design parameters.

Figure 2.16A shows the effect of different drift thresholds (δ_{thresh}) on the Pareto

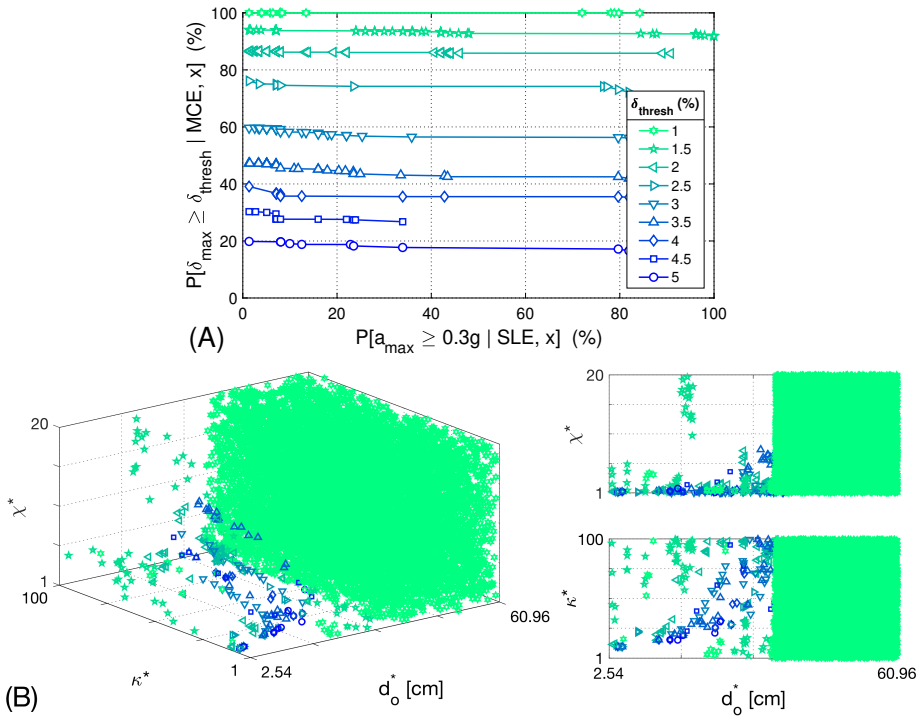


Figure 2.16: Effect of drift threshold δ_{thresh} on (A) Pareto front for a FIS ($\mu = 5\%$) installed on the second level and (B) Pareto optimal design parameters. Note that unequal axes scales are used to represent the failure probabilities (A).

front for a FIS installed on the second level with a mass ratio of 5%. As the drift threshold increases, the PS failure probability decreases from 100% ($\delta_{\text{thresh}} = 1\%$) to about 20% ($\delta_{\text{thresh}} = 5\%$). For each drift threshold, it is worth noting that the greatest reduction in PS failure probability between the anchor points is about 5.5%, occurring at $\delta_{\text{thresh}} = 3.5\%$. Therefore, in this case, a PS with a drift threshold of 3.5% would receive the greatest benefit from the dual-mode FIS. However, at 1% drift threshold, the PS has a 100% failure probability with almost no reduction between the anchor points. In such a case, it would be more beneficial to focus the design attention on saving the equipment than trying to have a better PS performance.

Figure 2.16B shows the Pareto optimal design parameters corresponding to the Pareto fronts in Figure 2.16A. It is observed that there is a big cluster of points corresponding to $\delta_{\text{thresh}} = 1\%$ and 100% PS failure probability occurring at $d_o \geqslant 34$ cm,

independent of κ and χ. For this case ($\delta_{\text{thresh}} = 1\%$), FISs exhibit no capability in protecting the PS, so it is best to avoid impacts via a large seismic gap. Optimal designs for small drift thresholds (1.5% and 2.0%) seem sparsely distributed at random with no notable relationship. However, optimal designs corresponding to greater drift threshold values ($> 2\%$) seem to exhibit an exponential-like relationship in κ and d_o as previously discussed.

2.5.4 Effect of Mass Ratio and Installation Location on Optimal Design

Lastly, the effect of mass ratio μ and installation location on the optimal design is analyzed. Figure 2.17 shows the Pareto fronts of FISs with varying mass ratio installed at different story levels. The case with no FIS shows the worst PS and FIS performances. On all the story levels, it is observed that the greater the mass ratio, the smaller the PS failure probability for the linear FIS. When attached to the first level (Figure 2.17A), the FIS works best as an isolator with the highest FIS failure probability of only 20%. This is because the first level has the smallest accelerations and therefore the lowest displacement demand on the FIS. In this case, however, the FIS has little effect in protecting the PS. For the case of a FIS installed on the third level (Figure 2.17C), the device has the greatest effect in improving the PS performance. By installing the FIS on the roof (Figure 2.17C), the FIS helps reduce the inter-story drift and thus provides great reduction in $J^{\text{PS}}_{\text{drift}}$. Typical vibration absorbers such as TMD are also commonly found at the top of the building (Gutierrez Soto and Adeli, 2013). With a high mass ratio of 20%, the PS failure probability can be reduced down to about 33% if the FIS performance can be sacrificed to have 75% failure probability. Moreover, when the FIS is installed at the roof, the demands on the FIS are highest, so the lower bound (best) on FIS performance is no longer 0%, but instead around 10%. Figure 2.17B shows Pareto fronts for the case of a FIS installed on the second level, which provides a middle ground between

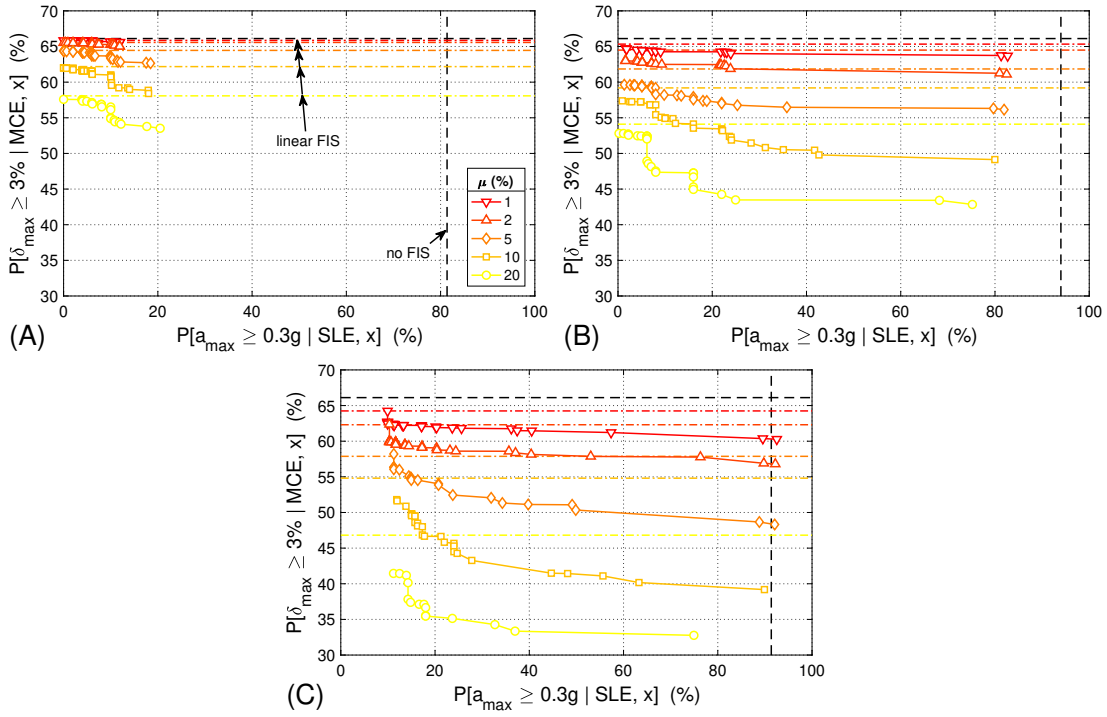


Figure 2.17: Pareto fronts for FISs with varying mass ratio μ installed on the (A) first level, (B) second level, and (C) third level. The horizontal/vertical lines are for the cases of no FIS (– – –) and linear FIS (– · –).

having the FIS function as an isolator (1st level) and an absorber (3rd level). Small mass ratios (1% and 2%) provide little improvement in terms of the PS performance even though the FIS performance is sacrificed. Larger mass ratios (10% and 20%) show greater reduction in the PS failure probability as the FIS is being sacrificed. Overall, the installation of the linear FIS with increasing mass ratio provides better protection to both the PS and the FIS than the case without the FIS. Depending on the intended application of the FIS, it works best as an isolator when installed on the lower level and as an absorber at the higher level.

2.6 Optimization with Genetic Algorithm

The preceding optimization study employed a random search to permit a thorough parametric study. This exhaustive search used 25,000 samples, each of which required two simulations—one at SLE and one at MCE. Alternatively, the optimization problem

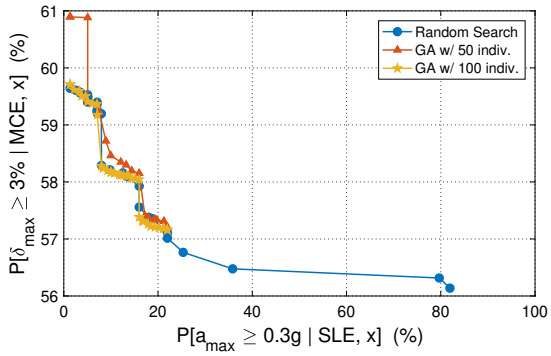


Figure 2.18: Comparison of Pareto fronts determined from a random search (25,000 samples) and a genetic algorithm (GA) with 50 or 100 individuals per generation: FIS ($\mu = 5\%$) installed on the second level. Note that unequal axes scales are used to represent the failure probabilities.

could have been approached using a variety of multi-objective optimization routines. As an example, here a controlled, elitist genetic algorithm (GA) (Deb, 2001) is considered. Such a GA helps to ensure convergence to the optimal Pareto front of the dominant designs that represent different compromises between the performance criteria. The GA was implemented in MATLAB using the `gamultiobj` algorithm considering 50 (default) and 100 individuals per generation. Figure 2.18 illustrates the Pareto fronts for the nominal case (Table 2.3) resulting from the random search and the GA. Good correspondence is seen between the various methods, but the GA with 50 individuals finds lower performing elite members compared to the other two methods. Neither of the GA optimizations are able to find the Pareto points with PS failure probabilities (ordinate) less than 57%. This is due to the relatively narrow range of design variables producing such performance (i.e., highly sensitive), illustrated by the sparsity of points in this region in Figure 2.13A. It is worth noting that the GA with 50 and 100 individuals per generation required 105 and 142 generations, respectively, to converge—5,250 and 14,200 total samples, respectively. These correspond to 79% and 43.2% reductions in function evaluations compared to the the random search (25,000). However, the results are specific to the case considered, and the GA would need to be rerun for a different scenario (e.g., different a_{thresh}, δ_{thresh}, β, etc.).

2.7 Summary

The performance of a dual-mode FIS installed in a multi-story PS has been studied. A nonlinear reduced order modeling procedure is proposed to ease the computational burden. The dual-mode behavior is realized through a Kelvin-type impact model, which is activated at a specified displacement (d_o). The performance of the PS-FIS system has been evaluated in terms of the vibration isolation (peak acceleration of FIS) and the vibration absorption (peak interstory drift of PS) to a suite of synthetic GMs representative of various hazards (SLE, DBE, and MCE). A parametric study has been performed to examine the importance of different controlling factors—seismic gap (d_o), impact parameters (κ and χ), isolated mass ratio (μ), FIS location within the PS, and performance metric parameters (a_{thresh}, δ_{thresh}, β)—on the FIS and PS performance. Two objective functions—(1) probability of the peak acceleration of the FIS exceeding a threshold acceleration under SLE-scaled GMs, and (2) probability of the maximum peak inter-story drift of the PS exceeding a threshold drift under MCE-scaled GMs—are used to measure the FIS and PS performance accordingly in the optimization study. These constitute competing objectives within the multi-objective stochastic design framework.

From the optimization and analysis, the following observations can be made: (1) in general, employing a bilinear FIS is an effective way to protect sensitive equipment under SLE hazards, so long as the displacement demand does not exceed the seismic gap d_o; (2) an increase in d_o yields better isolation performance (i.e., fewer impacts), but only insofar as the displacement demands on the FIS are large enough to produce impacts; (3) stiffening of the FIS under large displacements (greater than d_o) effectively couples the FIS and PS, decreasing the PS response in some cases; (4) there is a distinct optimal gap d_o resulting in reduced PS response, corresponding to modest reductions (0.5% to 5%) reductions in PS failure probabilities; (5) lower values of the stiffening parameter ($\kappa \leqslant 10$) provide better PS performance, tending toward TMD-like behavior

at MCE, but at a significant penalty of poor isolation performance of the FIS at SLE; (6) the damping parameter χ of the restrainer/bumper has negligible effect on the PS-FIS performance; (7) the mass ratio μ has a greater effect on the PS failure probability than that of the FIS, with larger mass ratios providing better performance for the linear and nonlinear (impact-based) PS-FIS systems; and (8) the PS-FIS system functions best as an isolator when installed at the first story level and best as an absorber when installed at the roof. Overall, the results have shown that the bilinear FIS can effectively protect sensitive equipment under SLE and also help to protect (albeit to a lesser degree) the PS under MCE, which constitutes a *dual-mode vibration isolator/absorber FIS*.

An experimental study to validate this concept is described in the next chapter.

Chapter 3
Experimental evaluation of the performance of a nonlinear dual-mode vibration isolator/absorber system

3.1 Overview

An experimental approach that aims to study the dual behaviour of the dual-mode FIS is described in this chapter. In Section 3.2, the equation of motion for FIS, PS and the coupled PS-FIS system are formulated, and the performance matrices for evaluating the isolation and absorption performance are defined. The experimental system that details the PS, FIS, and shock absorber are described in Section 3.3. The experimental protocol that describes the PS-FIS setup, GMs, and testing procedure can be referred to in Section 3.4. The experimental and numerical results are discussed in Section 3.5 and 3.6 respectively, followed by a summary of the chapter in Section 3.7.

3.2 Problem Formulation

This section addresses the equations of motion (EOM) of the FIS and the PS, as well as outline the metrics to evaluate the performance of the PS-FIS system.

3.2.1 Floor Isolation System

Lagrange's equation is used in this study to derive the equation of motion of the FIS utilizing pendulum bearings like the one shown in Figure 3.1. The kinetic energy $\mathcal{T}$ of

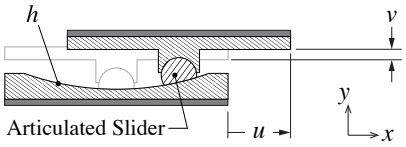


Figure 3.1: Schematic of friction pendulum (FP) bearing.

the FIS comes from the ground motion and the horizontal as well as vertical motion of the FIS itself (Wiebe and Harvey, 2019). The kinetic energy is given by

$$\mathcal{T}(\dot{u}, \dot{v}) = \frac{1}{2}m(\dot{u} + \dot{x}^t)^2 + \frac{1}{2}m(\dot{v} + \dot{y}^t)^2 \tag{3.1}$$

where u and v denote the horizontal and vertical displacements, respectively, of the FIS relative to the structural floor's total horizontal and vertical displacements, x^t and y^t, respectively. The overdot represents the derivative with respect to time and m denotes the total isolated mass of the FIS.

As the articulated slider of the FIS moves horizontally, the motion also results in a vertical displacement. The potential energy $\mathcal{V}$ of this system is given by

$$\mathcal{V}(v) = mgv + mgy^t \tag{3.2}$$

where g is the gravitational acceleration. The vertical displacement v is kinematically constrained by the rolling of the bearings across the concave surface having profile $h(u)$. Hence, the kinematic constraint is written as follows:

$$v = h(u) \tag{3.3}$$

Thus, the vertical velocity $\dot{v}$ can be found from the differentiation of Equation (3.3) to be

$$\dot{v} = h'(u)\dot{u} \tag{3.4}$$

Likewise, the vertical acceleration can be obtained by taking the derivative of the velocity to be

$$\ddot{v} = h''(u)\dot{u}^2 + h'(u)\ddot{u} \tag{3.5}$$

To formulate the equations of motion, the kinematic constraint [Equation (3.3)] is handled by the use of a Lagrange multiplier λ as follows:

$$\frac{d}{dt}\frac{\partial \mathcal{L}}{\partial \dot{u}} - \frac{\partial \mathcal{L}}{\partial u} = Q_u + \lambda \frac{\partial \phi}{\partial u} \tag{3.6a}$$

$$\frac{d}{dt}\frac{\partial \mathcal{L}}{\partial \dot{v}} - \frac{\partial \mathcal{L}}{\partial v} = Q_v + \lambda \frac{\partial \phi}{\partial v} \tag{3.6b}$$

where the Lagrangian $\mathcal{L} = \mathcal{T} - \mathcal{V}$, Q_u is the sum of forces coming from virtual work due to non-conservative forces (e.g., friction) and the contact force f_c, and the constraint is given by

$$\phi(u, v) = v - h(u) \equiv 0 \tag{3.7}$$

Applying this form of Lagrange's equation gives

$$m(\ddot{u} + \ddot{x}^t) = Q_u - \lambda h'(u) \tag{3.8a}$$

$$m(\ddot{v} + \ddot{y}^t) + mg = Q_v + \lambda \tag{3.8b}$$

From Equation (3.8), the force of constraint, which is *normal* to the constraint surface, is given by

$$\mathbf{N} = \lambda \begin{Bmatrix} -h'(u) \\ 1 \end{Bmatrix} \tag{3.9}$$

which has magnitude

$$N = \lambda \sqrt{1 + [h'(u)]^2} \tag{3.10}$$

Therefore, the normal (constraint) force can be re-written as follows:

$$\mathbf{N} = N \frac{1}{\sqrt{1 + [h'(u)]^2}} \begin{Bmatrix} -h'(u) \\ 1 \end{Bmatrix} \tag{3.11}$$

The forces Q_u and Q_v are due to friction $\mathbf{f}_f$ and the contact force $\mathbf{f}_c$ of impact. The friction force is perpendicular to $\mathbf{N}$, opposing the motion, and is modeled using a Bouc-Wen hysteresis model (Harvey and Gavin, 2014b):

$$\mathbf{f}_f = -\mu N \frac{1}{\sqrt{1 + [h'(u)]^2}} \begin{Bmatrix} 1 \\ h'(u) \end{Bmatrix} Z(t) \tag{3.12}$$

where A, β, γ, and n are the Bouc-Wen parameters, and s_y is arc-length displacement over which the full friction force is developed. The hysteretic displacement $Z(t)$ satisfies

$$\dot{Z}(t) = \dot{s}(t)\{A - [\beta \operatorname{sgn}(Z(t)\dot{u}(t)) + \gamma] |Z(t)|^n\}/s_y \tag{3.13}$$

Using the arc-length relationship:

$$ds^2 = du^2 + dv^2 \Rightarrow \dot{s} = \dot{u}\sqrt{1 + [h'(u)]^2} \tag{3.14}$$

By substituting Equation (3.14) into Equation (3.13),

$$\dot{Z}(t) = \dot{u}(t)\sqrt{1 + [h'(u)]^2}\{A - [\beta \operatorname{sgn}(Z(t)\dot{u}(t)) + \gamma] |Z(t)|^n\}/s_y \tag{3.15}$$

The contact force f_c from the impact is assumed to be purely in the u direction:

$$\mathbf{f}_c(u, \dot{u}) = \begin{Bmatrix} f_c(u, \dot{u}) \\ 0 \end{Bmatrix} \tag{3.16}$$

The specific form of the contact force f_c is shown in Equation 3.38 that is discussed later in Section 3.3.3.

From Equations (3.12) and (3.16), the generalized forces Q_u and Q_v are, therefore, given by

$$Q_u = -\mu N \frac{1}{\sqrt{1 + [h'(u)]^2}} Z(t) - f_c(u, \dot{u}) \tag{3.17a}$$

$$Q_v = -\mu N \frac{h'(u)}{\sqrt{1 + [h'(u)]^2}} Z(t) \tag{3.17b}$$

Substituting these expressions, as well as Equation (3.10), into Equation (3.8) gives

$$m(\ddot{u} + \ddot{x}^t) = -\mu N \frac{1}{\sqrt{1 + [h'(u)]^2}} Z(t) - f_c(u, \dot{u}) - N \frac{h'(u)}{\sqrt{1 + [h'(u)]^2}} \tag{3.18a}$$

$$m(\ddot{v} + \ddot{y}^t) + mg = -\mu N \frac{h'(u)}{\sqrt{1 + [h'(u)]^2}} Z(t) + N \frac{1}{\sqrt{1 + [h'(u)]^2}} \tag{3.18b}$$

By substituting Equation (3.5) as well as rearranging terms, Equation (3.18) becomes

$$m\ddot{u} + \mu\lambda Z(t) + \lambda h'(u) = -m\ddot{x}^t - f_c(u, \dot{u}) \tag{3.19a}$$

$$mh'(u)\ddot{u} + \mu\lambda h'(u)Z(t) - \lambda = -m\ddot{y}^t - mg - mh''(u)\dot{u}^2 \tag{3.19b}$$

Equation (3.19) represents a system of differential-algebraic equations (DAEs) (Shampine and Reichelt, 1997) in terms of two unknowns—$\ddot{u}$ (differential) and λ (algebraic). These equations are linear in the two unknowns, so they can be written as follows:

$$\begin{bmatrix} 1 & \mu Z(t) + h'(u) \\ h'(u) & \mu h'(u) Z(t) - 1 \end{bmatrix} \begin{Bmatrix} m\ddot{u} \\ \lambda \end{Bmatrix} = \begin{Bmatrix} -m\ddot{x}^t \\ -m[\ddot{y}^t + h''(u)\dot{u}^2 + g] \end{Bmatrix} \tag{3.20}$$

This equation is coupled to the PS in Section 3.2.4, but first the nonlinear FIS force is discussed in the next section.

3.2.2 Nonlinear FIS force

From Equation (3.19a), the force of the FIS can be derived as

$$f_{\text{FIS}} = \mu N \frac{1}{\sqrt{1 + [h'(u)]^2}} Z(t) + f_c(u) + N \frac{h'(u)}{\sqrt{1 + [h'(u)]^2}} \tag{3.21}$$

The first term in Equation (3.21) is the frictional component of the FIS where μ is the friction coefficient between the bearing and the curved track. The normal force, N, changes depending on the displacement of the FIS. The dimensionless hysteretic parameter $Z(t)$ is described by the nonlinear differential equation shown in Equation (3.15) where A, β, γ, and n are Bouc-Wen parameters (Fenz and Constantinou, 2008) taken to be 1, 1/2, 1/2, and 2, respectively, in this study, and s_y denotes the yield displacement

of the FIS which is taken to be 1 mm. These values were selected to give a reasonable representation of the rolling resistance in the system. The second term represents the contact force and the last term corresponds to the restoring force of the FIS.

For the case of a circular elevation profile with radius R,

$$h(u) = R - \sqrt{R^2 - u^2} \tag{3.22}$$

The slope is then given by

$$h'(u) = \frac{u}{\sqrt{R^2 - u^2}} = \frac{u}{R} + \frac{1}{2}\left(\frac{u}{R}\right)^3 + \cdots \approx \frac{u}{R} \tag{3.23}$$

Therefore, the curvature is given by

$$h''(u) = \frac{R^2}{(R^2 - u^2)^{3/2}} = \frac{1}{R} + \frac{3}{2}\frac{1}{R}\left(\frac{u}{R}\right)^2 + \cdots \approx \frac{1}{R} \tag{3.24}$$

3.2.3 Primary Structure

The PS used in this study is a three-story shear building, which can be modeled as a 3 degrees of freedom (DOF) system. The EOM of the PS is given by

$$\mathbf{M}\ddot{\mathbf{x}}(t) + \mathbf{C}\dot{\mathbf{x}}(t) + \mathbf{K}\mathbf{x}(t) = -\mathbf{M}\mathbf{1}\ddot{u}_g(t) \tag{3.25}$$

where $\mathbf{x}(t)$ is the story's horizontal displacement and $\mathbf{M}$, $\mathbf{C}$, and $\mathbf{K}$ are 3×3 mass, damping, and stiffness matrices, respectively. The mass and stiffness matrices are given by

$$\mathbf{M} = \begin{bmatrix} m_1 & 0 & 0 \\ 0 & m_2 & 0 \\ 0 & 0 & m_3 \end{bmatrix}, \quad \mathbf{K} = \begin{bmatrix} k_1 + k_2 & -k_2 & 0 \\ -k_2 & k_2 + k_3 & -k_3 \\ 0 & -k_3 & k_3 \end{bmatrix}$$

where m_i and k_i are the mass and stiffness of the ith story. The damping matrix is defined based on modal damping:

$$\mathbf{\Phi}^{\mathrm{T}}\mathbf{C}\mathbf{\Phi} = \begin{bmatrix} 2\zeta_1\omega_1 & 0 & 0 \\ 0 & 2\zeta_2\omega_2 & 0 \\ 0 & 0 & 2\zeta_3\omega_3 \end{bmatrix} \tag{3.26}$$

where ζ_i and ω_i are the damping ratio and the frequency in the ith mode, and $\mathbf{\Phi}$ is the mass normalized mode shape matrix. The quantities of these properties are detailed in Section 3.3.1. Vector $\mathbf{1}$ distributes the force coming from the horizontal ground acceleration $\ddot{u}_g(t)$ to each of the floors.

3.2.4 The Coupled PS-FIS System

The total acceleration of the floor at the isolation system's location is given by

$$\ddot{x}^t(t) = \mathbf{p}^{\mathrm{T}}(\ddot{\mathbf{x}}(t) + \mathbf{1}\ddot{u}_{\mathrm{g}}(t)) \tag{3.27}$$

where $\mathbf{p}$ is a vector identifying the position of the FIS on the structure. By substituting this equation into Equation (3.19a), the equation of motion of the FIS can be rewritten as

$$m\ddot{u}(t) + \frac{N}{\sqrt{1 + [h'(u)]^2}}[\mu Z(t) + h'(u)] + f_c(u, \dot{u}) = -m\mathbf{p}^{\mathrm{T}}(\ddot{\mathbf{x}}(t) + \mathbf{1}\ddot{u}_{\mathrm{g}}(t)) \tag{3.28}$$

With the force of the FIS shown in Equation (3.21), the dynamics of the coupled PS-FIS system is given by

$$\mathbf{M}\ddot{\mathbf{x}}(t) + \mathbf{C}\dot{\mathbf{x}}(t) + \mathbf{K}\mathbf{x}(t) = -\mathbf{M}\mathbf{1}\ddot{u}_{\mathrm{g}}(t) + \mathbf{p}f_{\mathrm{FIS}}(u, \dot{u}, \ddot{u}) \tag{3.29a}$$

$$m\ddot{u}(t) + f_{\mathrm{FIS}}(u, \dot{u}, \ddot{u}) = -m\mathbf{p}^{\mathrm{T}}(\ddot{\mathbf{x}}(t) + \mathbf{1}\ddot{u}_{\mathrm{g}}(t)) \tag{3.29b}$$

From Equation (3.29b), f_{FIS} can be expressed as

$$f_{\mathrm{FIS}}(u, \dot{u}, \ddot{u})x = -m[\ddot{u}(t) + \mathbf{p}^{\mathrm{T}}(\ddot{\mathbf{x}}(t) + \mathbf{1}\ddot{u}_{\mathrm{g}}(t))] \tag{3.30}$$

Substituting this relationship to Equation (3.29a), it can be re-expressed as

$$(\mathbf{M} + m\mathbf{p}\mathbf{p}^{\mathrm{T}})\ddot{\mathbf{x}}(t) + \mathbf{C}\dot{\mathbf{x}}(t) + \mathbf{K}\mathbf{x}(t) = -m\mathbf{p}\ddot{u}(t) - (\mathbf{M} + m\mathbf{p}\mathbf{p}^{\mathrm{T}})\mathbf{1}\ddot{u}_{\mathrm{g}}(t) \tag{3.31}$$

Therefore, variable $\ddot{\mathbf{x}}(t)$ and $\ddot{u}(t)$ can be simultaneously solved from Equations (3.31) and (3.20) which can be expressed in a matrix form as follow

$$\begin{bmatrix} (\mathbf{M} + m\mathbf{p}\mathbf{p}^{\mathrm{T}}) & m\mathbf{p} & \mathbf{0}_{3\times 1} \\ m\mathbf{p}^{\mathrm{T}} & m & \mu Z(t) + h'(u) \\ \mathbf{0}_{1\times 3} & mh'(u) & \mu h'(u) Z(t) - 1 \end{bmatrix} \begin{Bmatrix} \ddot{\mathbf{x}}(t) \\ \ddot{u}(t) \\ \frac{N}{\sqrt{1+[h'(u)]^2}} \end{Bmatrix} = \begin{Bmatrix} -\mathbf{C}\dot{\mathbf{x}}(t) - \mathbf{K}\mathbf{x}(t) - (\mathbf{M} + m\mathbf{p}\mathbf{p}^{\mathrm{T}})\mathbf{1}\ddot{u}_{\mathrm{g}}(t) \\ -m\ddot{u}_{\mathrm{g}}(t) - f_c(u, \dot{u}) \\ -m[h''(u)\dot{u}^2 + g] \end{Bmatrix} \quad (3.32)$$

In this study, vertical displacement in the PS and FIS is assumed to be negligible. Therefore, the system consists of 9 states comprised of 6 states for the displacement $\mathbf{x}(t)$ and velocity $\dot{\mathbf{x}}(t)$ of each floor in the PS, 2 states for FIS displacement $u(t)$ and velocity $\dot{u}(t)$, and 1 state for the hysteretic displacement $Z(t)$. Notice that the hysteretic parameter $\dot{Z}(t)$ [Equation (3.15)] is also being solved at the same time as variable $\ddot{\mathbf{x}}(t)$ and $\ddot{u}(t)$ in Equation (3.32). However, the quantities of interest concern only $\ddot{\mathbf{x}}(t)$ and $\ddot{u}(t)$.

Using MATLAB (R2019A, Mathworks, Natick, MA), Equations (3.32) and (3.15) can be solved by utilizing the ODE built-in function `ode45` (Dorman and Prince, 1980; Shampine and Reichelt, 1997). This solver was selected because it utilizes an adaptive time stepping algorithm, which can help ensure that the nonlinear, piecewise dynamics are properly captured. The interval of integration (`tspan`) is set from zero to the final GM time with an increment of 0.001 sec, i.e., `tspan = 0:0.001:tf` where `tf` is the earthquake duration. The initial conditions are set as a vector of zero. The relative tolerance (`RelTol`) and absolute tolerance (`AbsTol`) are taken to be 10^{-4} and 10^{-7}, respectively. These values are obtained by first starting with the default tolerances (10^{-3} and 10^{-6}) and progressively tightening them until no noticeable changes are observed. In this case, since the tolerances of 10^{-4} and 10^{-7} provide very similar result as 10^{-5} and 10^{-8}, the former set is used for the simulation. All other values in this numerical

integration are taken to be default. Greater computational efficiency could be achieved through the use of event location (Shampine et al., 1991), for example state event location algorithm (Wright and Pei, 2012), but this is a topic of future research.

3.2.5 Performance Metrics

The performance evaluation of the dual-mode FIS is divided into two categories based on the intensity of the GM. For low-intensity GMs (those with intensity scale factors below impact), the evaluation concerns the isolation performance of the FIS. This is considered when the system displaces within its allowable capacities and behaves as a linear system. For high-intensity GMs (those with intensity scale factors above impact), the evaluation concerns the absorption performance of the PS. This is considered when the system displaces more than its allowable capacities, thus creates an impact that results in a nonlinear system. The dual-mode FIS performance is evaluated for three different seismic gaps with details described in Section 3.4.3.

In the case of the FIS, the response quantity of greatest interest is the absolute acceleration of the FIS:

$$a_{\text{FIS}}^{\max} = \max_t |a(t)| \tag{3.33}$$

where $a(t)$ is the absolute acceleration of the FIS and $a_{\text{FIS}}^{\max}$ is the maximum acceleration of the FIS. Of secondary interest is the displacement of the FIS relative to the structure level:

$$u^{\max} = \max_t |u(t)| \tag{3.34}$$

where $u(t)$ is the absolute FIS displacement and $u^{\max}$ is the maximum displacement of the FIS. To evaluate the isolation performance, $a_{\text{FIS}}^{\max}$ is then compared to the second story's acceleration (a_2) for the case of no FIS ($a_2^{\text{no FIS}}$) and locked FIS (a_2^{locked}). The isolation performance is also indicated by the normalized isolation performance index

(J_a) which is defined as

$$J_a = \frac{a_{\text{FIS}}^{\max}}{a_2^{\text{locked}}} \tag{3.35}$$

Note that later figures showing J_a will also includes the case of $a_2^{\text{no FIS}}$ being normalized by a_2^{locked}.

In the case of the PS, the response quantity of interest is the peak inter-story drift ratio:

$$\delta_i^{\max} = \max_t |d_i(t)/h_i| \tag{3.36}$$

where $d_i(t)$ and h_i are the inter-story drift and height of the ith story respectively, and $\delta_i^{\max}$ is the maximum inter-story drift ratio of the associated story. To evaluate the absorption performance, $\delta_i^{\max}$ is then compared to each story's inter-story drift ratio for the case of no FIS ($\delta_i^{\text{no FIS}}$) and locked FIS (δ_i^{locked}). The absorption performance is also indicated by the normalized absorption performance index (J_δ) which is defined as

$$J_\delta = \frac{\delta_1^{\max}}{\delta_1^{\text{locked}}} \tag{3.37}$$

since the inter-story drift of the first floor is the largest. Note that later figures showing J_δ also includes the case of $\delta_1^{\text{no FIS}}$ being normalized by δ_1^{locked}.

3.3 Experimental System

To evaluate the performance of the proposed dual-mode FIS, the system was experimentally tested at Donald G. Fears Structural Engineering Laboratory at the University of Oklahoma. The PS and dual-mode FIS are described in the next sections.

3.3.1 Primary Structure

The PS used in this experimental approach is a lab-scale three-story shear structure made of steel as shown in Figure 3.2.



Figure 3.2: Primary structure at Fears Lab

The PS is a linear 3DOF system where mass, stiffness and damping of the structure were obtained using a method of system identification, which is detailed in Appendix C. Mass and stiffness of each floor are identified as shown in Table 3.1. Modal frequency and damping in each mode are identified as shown in Table 3.2. The columns of the structure are made of high yield strength spring steel and its base is attached to a shake

Table 3.1: Mass and stiffness of each floor of the experimental structure

PS property	Floor 1	Floor 2	Floor 3
Mass [kg]	56.06	56.29	56.20
Stiffness [N/mm]	112.83	135.64	158.35

Table 3.2: Modal properties of the experimental structure

Modal property	Mode 1	Mode 2	Mode 3
Frequency [Hz]	3.3	9.8	14.4
Damping [%]	0.10	0.10	0.20

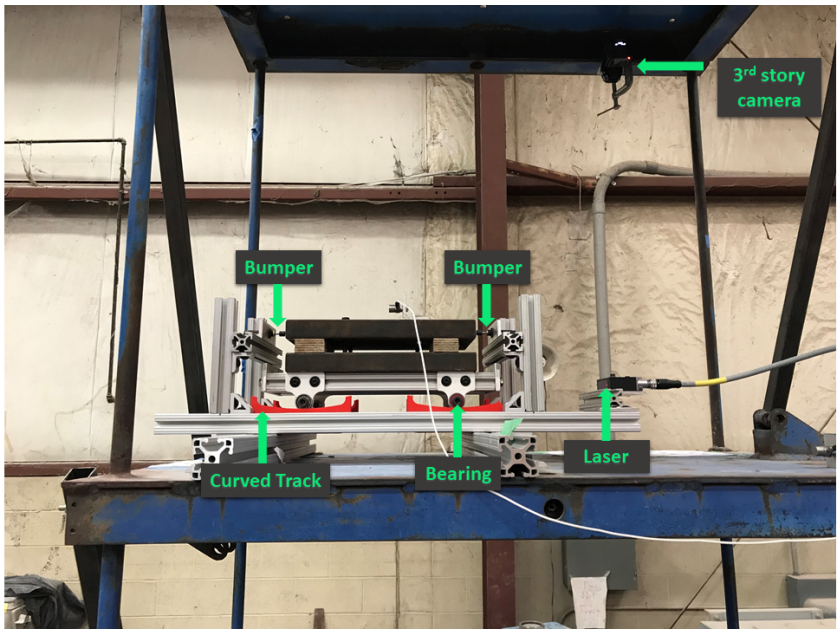


Figure 3.3: Experimental floor isolation system

table in fixed connection allowing displacement in only one direction. Details of the structural components of the PS can be referred to in Table C.3 of Appendix C.

3.3.2 Floor Isolation System

The FIS used in this experiment is shown in Figure 3.3. The system consists of 4 ball bearings that roll on the 3D-printed curved tracks (Calhoun and Harvey, 2018) each having a radius of curvature of 26 cm, which corresponds to a system with 1 Hz frequency. The isolated equipment is represented by two steel blocks that constitute a total mass of 9 kg, which is equivalent to about 16% of the 2nd floor's mass and 5.3% of the PS's total mass. To create nonlinearity in the system, the FIS is designed to gradually impact with two bumpers (characterize in Section 3.3.3), each is installed on either side of the FIS as shown in Figure 3.3. Miniature shock absorbers (MC25, Ace Controls Inc., Farmington Hills, MI, USA) were selected based on their energy capacity for this application. These bumpers have a stroke of 6.6 mm [0.26 in.] that allows for an additional compression during impact. Therefore, for clarification, seismic gap is

measured from the FIS's equilibrium position to the first touch when the steel engages with the bumper.

The FIS is characterized using a sine sweep test that was conducted at Fears Lab. Details of the characterization test can be found in Appendix D. The result has shown that the FIS is indeed a nonlinear system, exhibiting a hardening behavior and hysteretic behavior.

3.3.3 Bumper

The bumper was characterized using a static load-deflection test at multiple rates of 12.5, 25, 50, 100, 250, 500, and 1000 mm/min. From these tests, the contact force f_c model was identified to be:

$$f_c(u,\dot{u}) = \{k_1[u - u_o\,\mathrm{sgn}(u)] + f_o\,\mathrm{sgn}(u) + f_f\,\mathrm{sgn}(\dot{u})] \times \mathbb{I}_{|u|\geqslant u_o} + c\dot{u} \times \mathbb{I}_{u\dot{u}\geqslant 0} \times \mathbb{I}_{|u|\geqslant u_o+u_1} + k_2[u - (u_o+u_2)\,\mathrm{sgn}(u)] \times \mathbb{I}_{|u|\geqslant u_o+u_2} \quad (3.38)$$

where $k_1 = 0.8205$ N/mm, $f_o = 2.154$ N, $f_f = 0.9776$ N, $c = 0.935$ N·s/mm, $u_1 = 0.88$ mm, $k_2 = 50$ N/mm, $u_2 = 6.3$ mm, $\mathrm{sgn}(\cdot)$ is the signum function, and $\mathbb{I}_{(\cdot)}$ is the indicator function.

Figures 3.4(a) and 3.4(b) show load-deflection curves based on the experimental data and the estimated contact force in Equation (3.38) respectively, both exhibit hysteric behaviour that include friction and damping. Since these two plots share similar features overall, the estimated equation is acceptable for use in obtaining the numerical results for evaluating the dual-mode FIS performance.

3.4 Experimental Protocol

This section describes a detailed procedure of the experimental testing as well as the scaling of the GMs.

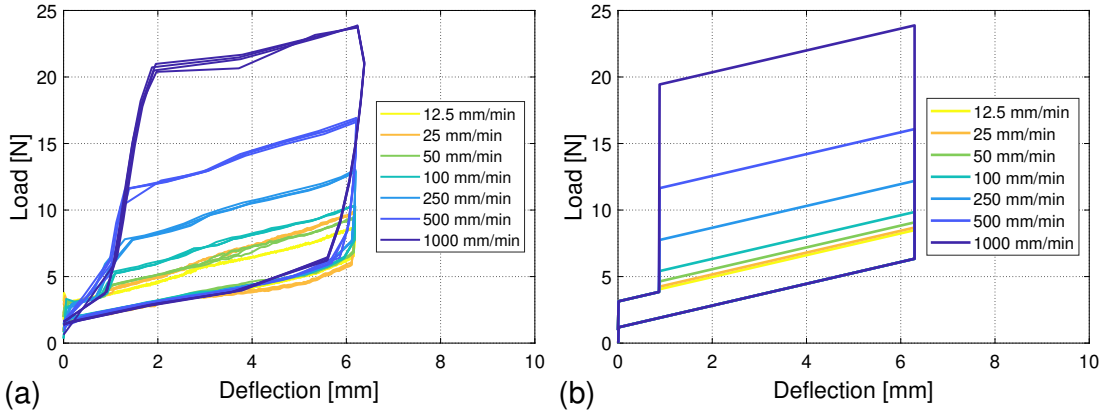


Figure 3.4: Load-deflection curves based on (a) experimental data and (b) estimated contact force f_c model

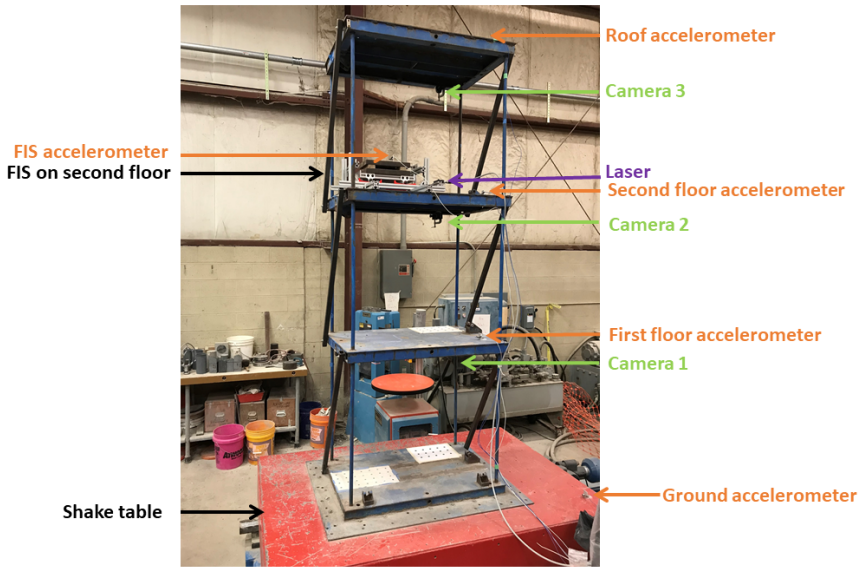


Figure 3.5: Experimental PS-FIS system

3.4.1 PS-FIS Setup

Setup of the PS-FIS system is shown in Figure 3.5. The FIS is installed on the second floor to provide a middle ground between expected good isolator (reduced FIS acceleration) and good absorber (reduced PS drift/displacement) behaviors. This is because a vibration absorber such as TMD generally works best at the top of the building while an isolator is most effective when installed on lower floors because of lower displacement

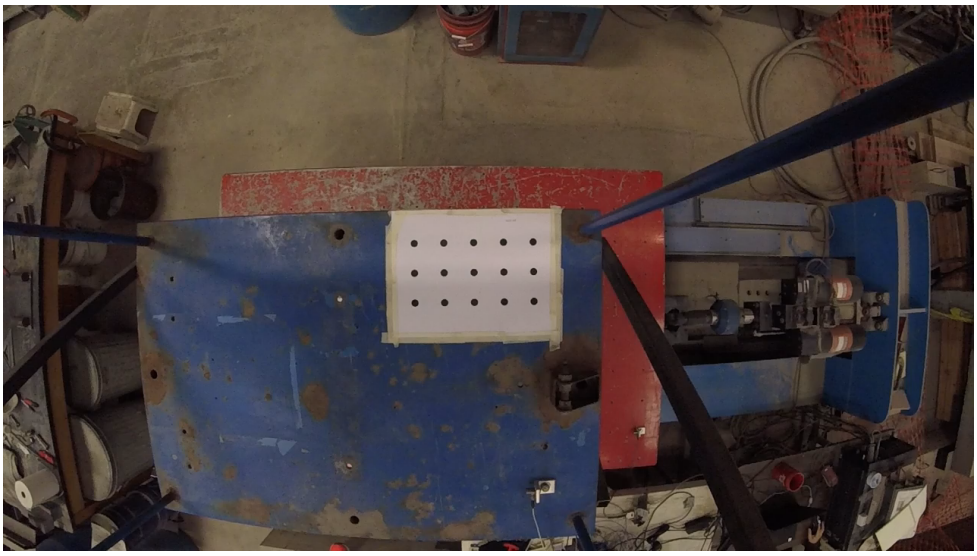


Figure 3.6: A camera shot from the second story camera capturing the second inter-story drift

demands.

As shown in this setup, 5 accelerometers (352C33, PCB Piezotronics, Inc., Depew, NY) are installed to measure the acceleration of the ground, first floor, second floor, third floor, and the FIS. To measure the inter-story drift of each floor, 3 cameras (HERO Session, GoPro, Inc., San Mateo, CA) are installed (Harvey and Elisha, 2018; Zare Hosseinzadeh et al., 2021). Each is rigidly attached to the underside of the deck of the first floor, second floor and third floor as shown. A laser (optoNCDT 1302, Micro-Epsilon, Ortenburg, Germany) is also attached to measure the displacement of the FIS. The accelerometers, cameras, and laser used sample rates of 2000 Hz, 100 fps, and 750 Hz, respectively.

Figure 3.6 shows a picture from the camera that is attached underside of second floor's deck that is used to capture the motion of the calibration/tracking grid. This 50.8 $\times$ 50.8 mm grid of high-contrast dots is taped on the deck of all floors of the PS directly under each camera. Inter-story drift of each floor can be determined from the movement of the black dots during testing.

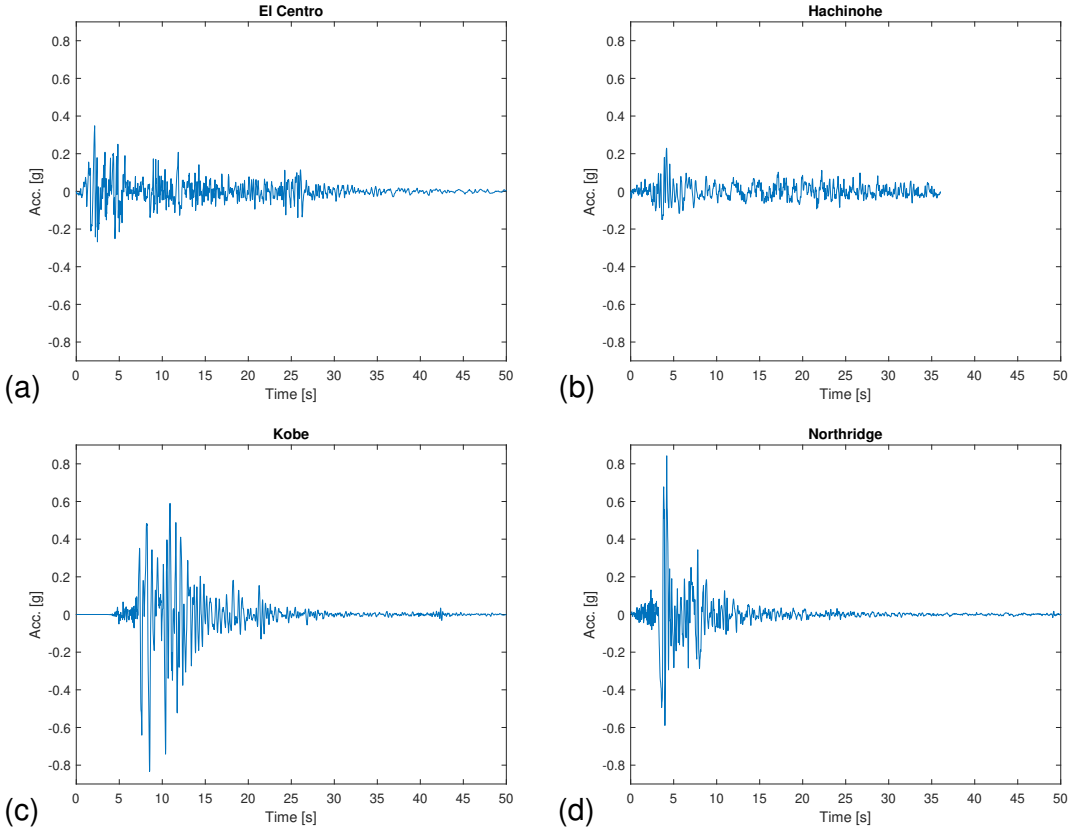


Figure 3.7: Time histories of (a) El Centro, (b) Hachinohe, (c) Kobe and (d) Northridge

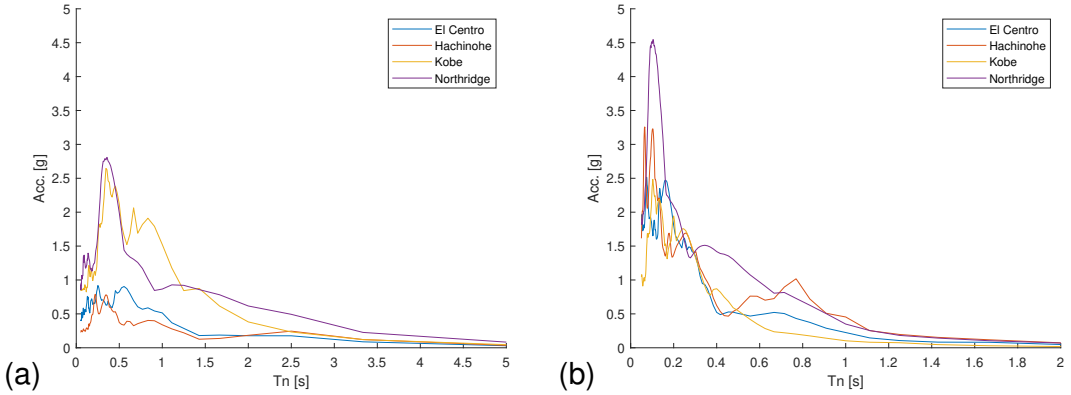


Figure 3.8: Response spectrum with 5% damping for (a) unscaled and (b) scaled GMs

3.4.2 Ground Motions and Testing

Four historic GMs—El Centro, Hachinohe, Kobe and Northridge—are used in this experiment. These GMs are selected based on the recommendation of Ohtori et al. (2004).

Table 3.3: Ground motions used for study, including peak values for the unscaled records.

Name	Earthquake	Station	Date	Component
El Centro	Imperial Valley, California	Imperial Valley Irrigation District	May 18, 1940	N-S
Hachinohe	Tokachi-oki	Hachinohe City	May 16, 1968	N-S
Kobe	Hyogoken Nanbu	Kobe Japanese Meteorological Agency	January 17, 1995	N-S
Northridge	Northridge, California	Sylmar County Hospital parking lot	January 17, 1994	N-S

Table 3.4: Characteristics of unscaled ground motions.

Name	PGA (g)	S_1 (g)	I_a (m/s)	t_{strong} (s)
El Centro	0.348	0.515	1.82	24.4
Hachinohe	0.229	0.339	0.903	27.9
Kobe	0.834	1.52	8.39	8.34
Northridge	0.843	0.866	5.01	5.33

Time history of each GM is shown in Figure 3.7, and their details are tabulated in Table 3.3. Peak ground acceleration (PGA) and some important intensity measures are listed in Table 3.4, including the Arias intensity I_a (Arias, 1970) and the strong motion duration t_{strong} accounting for 90% of the total I_a (Trifunac and Brady, 1975). The response spectra with 5% damping for both unscaled and scaled GMs are shown in Figure 3.8. Detail on the scaling of the GMs is discussed in the next section.

3.4.2(a) Scale Factors

Three types of scale factors (SFs) have been applied to the real GM data in order to generate the lab-scale GMs. These include the scale factor for similitude, spectral acceleration and GM intensity.

Similitude Scale Factor. In order to generate a suitable GM in the lab, the earthquake's amplitude and time are scaled using the benchmark building (Ohtori et al., 2004) as a reference structure. The SF is then calculated based on the similitude analysis.

The SF for time is given by

$$S_t = \frac{1/f_{ref}}{1/f_p} \tag{3.39}$$

where f_{ref} and f_p denote the fundamental frequency of the reference structure and the experimental prototype respectively. The reference structure has a fundamental frequency of 0.99 Hz while that of the lab prototype is 3.3 Hz. Substituting these values into Equation (3.39), the time SF is $S_t = 3.4$.

The length SF is given by

$$S_L = \frac{H_{ref}}{H_p} \tag{3.40}$$

where H_{ref} and H_p denote the height of the reference structure and the prototype respectively. The benchmark building has a story height of 396.24 cm and that of the prototype is 79.375 cm. Substituting these numbers into Equation (3.40), the length SF is $S_L = 4.99 \approx 5$.

Spectral Acceleration Scale Factor. The GMs have been scaled to have a spectral acceleration of $0.2g$ at 1 sec period and 5% damping. This number takes into consideration the actuator's maximum allowable displacement in the lab.

GM Intensity Scale Factor. Since the performance of the dual-mode FIS is evaluated based on GM intensity, an additional scale factor has been applied such that the FIS can be tested from low-intensity GMs to high-intensity GMs. The range of the intensity SF is different for each GM depending on how harsh the GM affects the PS, which can be estimated visually from the PS responses in the lab. The intensity SFs for each GM can be referred to in Table 3.5.

The above-mentioned SFs have been applied to generate lab-scale GMs. Note that the similitude SF is the same for all GMs. However, the spectral acceleration SF and intensity SF vary according to the earthquakes.

3.4.3 Testing procedure

As mentioned in Section 3.2.5, performance evaluation of the dual-mode FIS with three seimic gaps are compared to the case of no FIS and locked FIS. The former refers to the case where the FIS is removed from the second floor of the PS. The latter refers to the case where the FIS is not allowed to move, i.e., the seismic gap is equivalent to zero.

To see how displacement capacity affects the performance of the dual-mode FIS, the three seismic gaps used for the FIS is tabulated in Table 3.6. The naming convention of the gap can be disregarded since it is merely due to the testing sequence conducted in the lab. Gap B serves as the nominal case in which gaps C and F are picked based on.

Table 3.5: Experimental tests conducted. Impacts were observed at scale factors that are *italicized*.

Configuration	GM	Scale factors
No FIS	El Centro	0.5, 1, 2, 3
	Hachinhoe	0.5, 1, 1.5
	Kobe	0.5, 1, 2, 3
	Northridge	0.5, 1, 1.5, 2
Locked FIS	El Centro	0.5, 1, 2, 3
	Hachinohe	0.5, 1, 1.5
	Kobe	0.5, 1, 2, 3
	Northridge	0.5, 1, 1.5, 2
Gap B	El Centro	0.25, 0.5, 0.75, *1*, *1.25*, *1.5*, *1.75*, *2*, *2.25*, *2.5*
	Hachinohe	0.125, 0.25, 0.375, *0.5*, *0.75*, *1*, *1.25*, *1.5*
	Kobe	0.25, 0.5, 0.75, 1, *1.25*, *1.5*, *1.75*, *2*, *2.25*, *2.5*, *2.75*, *3*
	Northridge	0.25, 0.375, 0.5, *0.625*, *0.75*, *1*, *1.25*, *1.5*, *1.75*, *2*
Gap C	El Centro	0.125, 0.25, 0.375, *0.5*, *0.625*, *0.75*, *0.875*, *1*, *1.25*, *1.5*, *1.75*, *2*
	Hachinohe	0.125, *0.25*, *0.375*, *0.5*, *0.625*, *0.75*, *1*, *1.25*
	Kobe	0.125, 0.25, 0.375, *0.5*, *0.625*, *0.75*, *1*, *1.25*, *1.5*, *1.75*, *2*
	Northridge	0.125, 0.25, *0.375*, *0.5*, *0.625*, *0.75*, *1*, *1.25*, *1.5*
Gap F	El Centro	0.5, 0.75, 1, *1.25*, *1.5*, *1.75*, *2*, *2.25*
	Hachinohe	0.25, 0.375, *0.5*, *0.625*, *0.75*, *1*, *1.25*, *1.5*
	Kobe	0.5, 1, 1.5, *1.75*, *2*, *2.25*
	Northridge	0.25, 0.5, 0.75, *1*, *1.25*, *1.5*, *1.75*, *2*

Gap C is smaller than gap B by half whereas gap F is larger than gap B by 50%.

The configuration of the testing as well as the intensity SFs for each GM are shown in Table 3.5. These intensity SFs are selected to cover a reasonable range of data points prior to and after impacts for each GM. Note that a SF of 1 is equivalent to the case in which the intensity SF has not been included.

3.5 Experimental Results

This section discusses the experimental results and evaluates the dual functionality of the FIS. To recall, the isolation performance is determined by evaluating the maximum acceleration of the FIS ($a_{\text{FIS}}^{\text{max}}$) and the second floor ($a_2^{\text{locked}}$). On the other hand, the absorption performance is determined by evaluating the inter-story drifts of the first, second and third floor denoted by δ_1, δ_2 and δ_3 respectively. The case of locked FIS serves as a baseline performance for evaluating the cases with seismic gaps, although the case of no FIS has also been included in the results.

Since the dual-mode FIS performs differently when subjected to different earthquakes, each GM is evaluated individually containing the discussion of their baseline performance, isolation performance and absorption performance. Note that "scale factors (SF)" in this section refers to the intensity scale factor.

3.5.1 El Centro

3.5.1(a) Baseline (linear) performance

Figure 3.9 shows the response of the PS with no FIS and the locked FIS when subject to El Centro at varying GM SFs. The 2nd floor's peak total acceleration (Figure

Table 3.6: Seismic gaps used for experimental FIS

	Gap		
	B	C	F
Displacement Capacity [mm]	21.95	11.95	32.79

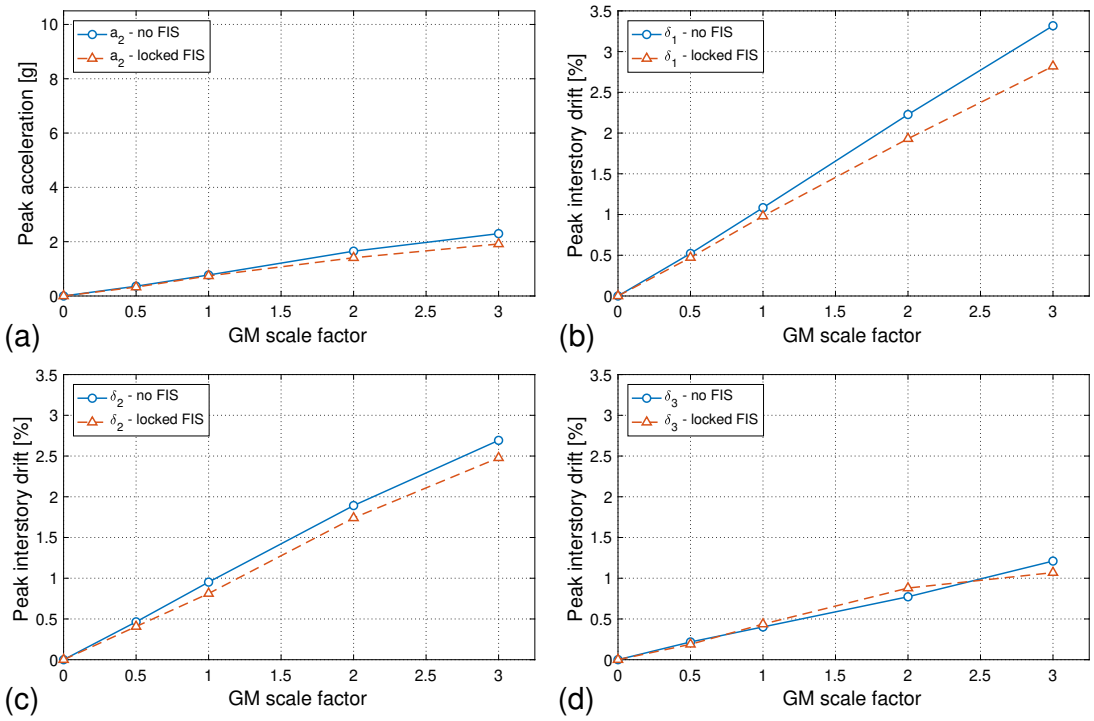


Figure 3.9: Peak responses with no FIS and locked FIS for El Centro: (a) 2nd floor total acceleration a_2, (b) 1st story drift δ_1, (c) 2nd story drift δ_2, and (d) 3rd story drift δ_3.

3.9(a)) and the peak inter-story drift ratios (Figures 3.9(b–d)) exhibit approximately linear responses over the range of GM SFs considered. In nearly all cases, larger peak accelerations and inter-story drifts are seen for the case of no FIS. These PS responses serves as the baseline to which the isolation and absorption performance of the FIS are compared in the following sections.

3.5.1(b) Isolation performance

Figure 3.10 shows peak responses of the FIS with different gaps at varying GM SFs when subjected to El Centro. Total acceleration and displacement of the FIS are shown in Figures 3.10(a) and 3.10(b) respectively.

For the acceleration response (Figure 3.10(a)), there is always a decrease in acceleration prior to impact for all three gaps. At a SF of 0.5, gap B and gap F have a decrease in acceleration with respect to locked FIS of about 82% and 72% respectively. Gap

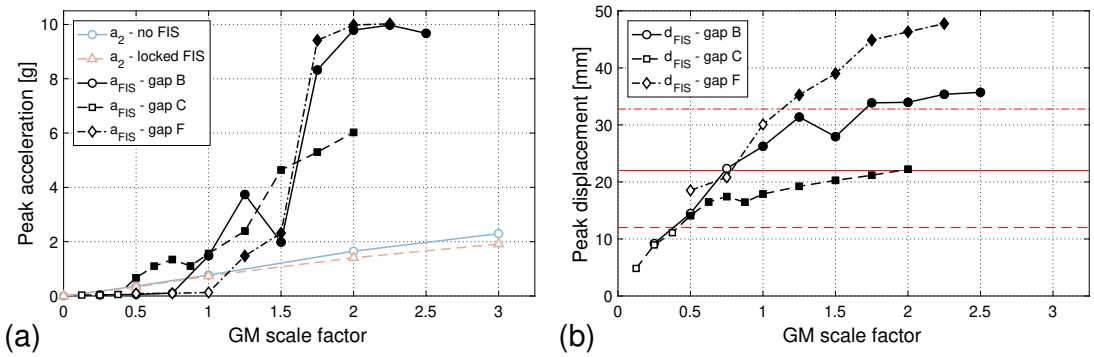


Figure 3.10: Peak FIS responses with different seismic gaps for El Centro: (a) total accelerations a_2 and a_{FIS}, and (b) FIS displacement d_{FIS}. The horizontal lines represent the seismic gap for each case (based on line style). The filled markers indicates cases in which impacts occurred in the FIS.

C also indicates a reduction in acceleration before it impacts. Therefore, prior to impact, the FIS performs well as an isolator when subjected to El Centro. However, when impacts occur, the data tells a different story. A dramatic rise in acceleration can be observed for all cases. Gap B experiences an increase in FIS acceleration about twice as much the baseline case at a SF of 1. Similar observation can be made during impact of gap C and gap F. After the first impact occurs, the system continues to gain acceleration as the GM SF increases. Therefore, during and after impact, the performance of the FIS as an isolator degrades, during which time the experimental evaluation shifts to look at the PS responses instead as discussed in Section 3.5.1(c).

For the FIS displacement response (Figure 3.10(b)), notice that the three horizontal lines are below each gap's impact SF, which means gaps B, C and F indeed impact at a SF of 1, 0.5 and 1.25 respectively. As shown in Figure 3.10(b), the displacement of the FIS continues to increase even though it has already reached its allowable displacement capacity. This is due to the aforementioned additional compression of 6.6 mm in the bumpers. However, the ultimate displacement goes beyond the addition of 6.6 mm, which means there has to be an additional deflection in the system. This could be due to the way the bumpers are installed during testing. As seen in Figure 3.3, the bumpers are located at the end of a cantilever (from the aluminum support), and thus deflects

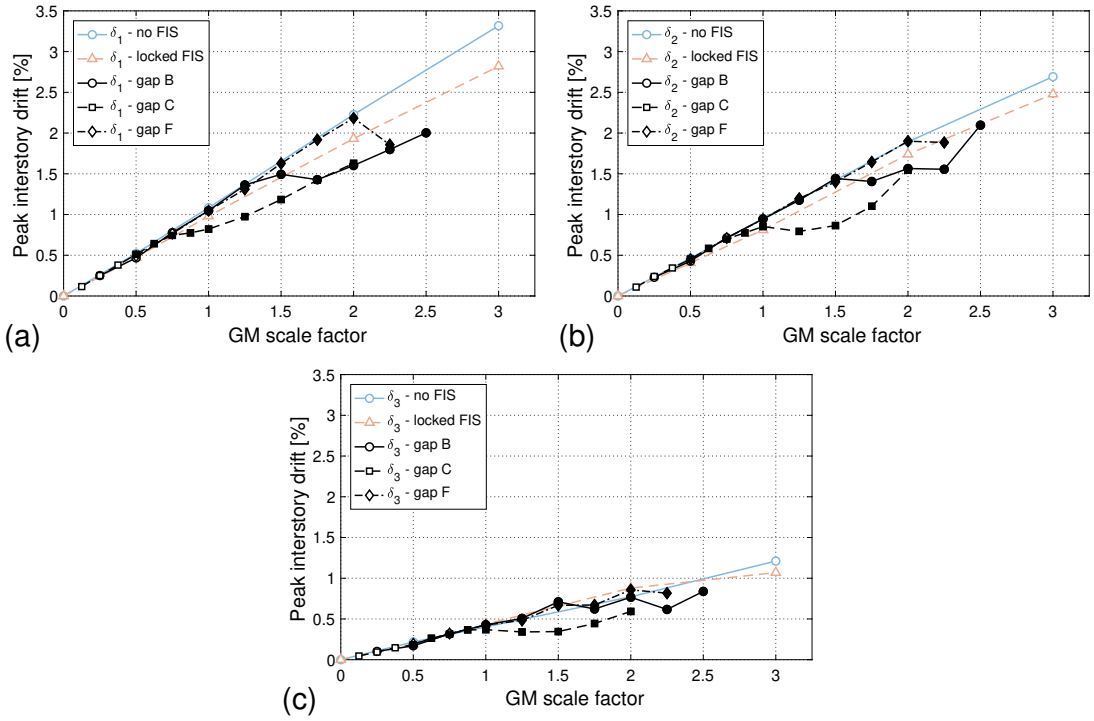


Figure 3.11: Peak PS responses with different seismic gaps for El Centro: (a) 1st story drift δ_1, (b) 2nd story drift δ_2, and (c) 3rd story drift δ_3. The filled markers indicates cases in which impacts occurred in the FIS.

when strongly hit by the top steel plate. This phenomenon can also be seen in other GM cases.

3.5.1(c) Absorption performance

Figure 3.11 shows peak responses of the PS with different gaps at varying SFs when subjected to El Centro. Prior to impact, it is apparent that the drift responses for the case with FIS are almost the same as the case of no FIS. Therefore, the FIS has no effect on the responses of the PS when it displaces within the allowable capacity.

However, after impact, a divergence from the linear response can be observed for all three stories. The greatest observable divergence belongs to gap C where the reduction seems greatest at a SF of 1.5. This gap, though has a smaller capacity, seems to outperform gap B and gap F for the absorption performance. While gap B and gap F also exhibit inter-story drift reduction, notice that their divergence occur at higher SFs

compared to gap C because they have larger gaps and need higher intensity SFs to see impacts. Among the three stories, gap B shows the best reduction in the first story while its performance in the second and third stories is variable. Even though gap F has seismic displacement capacity 50% larger than gap B, it seems to perform worse than gap B and C overall. After impact, gap F continues to show increase in drift until a SF of 2, but eventually exhibits a reduction at a SF of 2.25.

For all gaps, a reduction in inter-story drift does not occur immediately after impact. Noticeable divergence seems to happen at a higher GM SF where the impact is stronger. Recall that gap B and C have the greatest gain in FIS acceleration from a SF of 1.5 to 1.75 (see Figure 3.10(a)). At this intensity, gap B also exhibits its first reduction in drift as shown in Figure 3.11, which mean harsh impact is good for the absorption performance of gap B. However, gap F continues to show increase in inter-story drift despite experiencing similar acceleration gain at a SF of 1.5. For gap C, a similar observation to gap B can be observed where it shows great absorption performance within the intensity range in which it has high acceleration content.

In conclusion, when subjected to El Centro, the FIS indeed shows absorption performance after impact. However, this performance varies for different seismic gaps.

3.5.2 Hachinohe

3.5.2(a) Baseline performance

Figure 3.12 shows the linear response of the PS with no FIS and locked FIS when subjected to Hachinohe at varying SFs. Figure 3.12(a) shows peak acceleration of the second floor where the response is approximately linear. Figures 3.12(b), 3.12(c) and 3.12(d) show peak inter-story drift of the first, second and third stories respectively. The responses for the case of locked FIS look more linear than those for the case of no FIS. For both acceleration and inter-story drifts, higher responses are observed for the case of no FIS. These PS responses serve as the baseline performance for discussing the

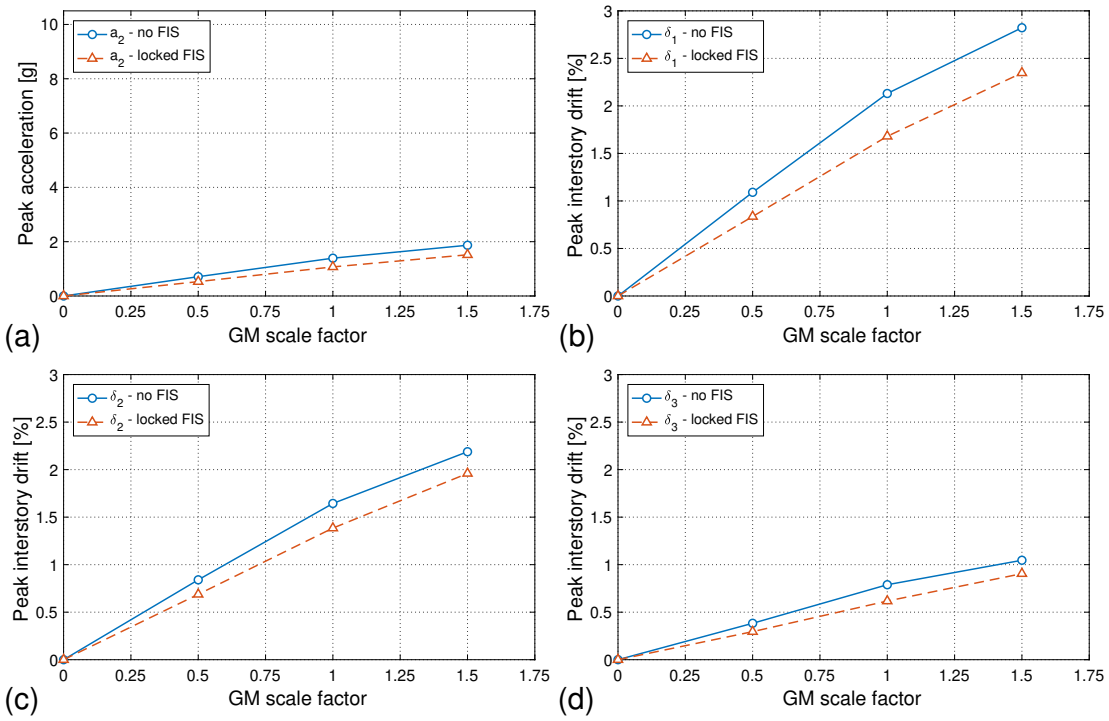


Figure 3.12: Peak responses with no FIS and locked FIS for Hachinohe: (a) 2nd floor total acceleration a_2, (b) 1st story drift δ_1, (c) 2nd story drift δ_2, and (d) 3rd story drift δ_3.

isolation and absorption performances for Hachinohe.

3.5.2(b) Isolation performance

Figure 3.13 shows peak responses of the FIS with different gaps at varying GM SFs. Total acceleration and displacement of the FIS are shown in Figures 3.13(a) and 3.13(b) respectively. For Hachinohe, impacts occur at a relatively smaller SF compared to El Centro. Thus, not a lot of data points can be seen prior to impact. However, it is still apparent from Figure 3.13(a) that all cases with FIS gaps have peak acceleration below that of the locked FIS case when the system is linear (i.e., prior to impact), which indicates that the FIS exhibit isolation performance. However, during and after impact, a gain in acceleration can be observed in all cases. While gap C shows a more gradual increase in acceleration, gap B and F exhibit a drastic gain between a SF of 0.75 and 1. Thus, when subjected to Hachinohe, the FIS also performs poorly as an isolator in the

nonlinear region. The absorption performance is discussed in the Section 3.5.2(c).

Figure 3.13(b) shows that the FIS impacts at a SF of 0.25 for gap C, and 0.5 for both gap B and F. It is observed that the FIS displacement from this GM also results in the 6.6 mm compression of the bumper as well as an additional deflection in the cantilever. Notice that a gain in acceleration of the FIS can also be reflected from its increase in displacement since Figures 3.13(a) and 3.13(b) share similar pattern.

3.5.2(c) Absorption performance

Figure 3.14 shows peak inter-story drift of the PS with different seismic gaps at varying GM SFs. For all cases, a reduction in the PS responses can be observed after impact. The reduction is clearly the greatest in the first story, while noticeable divergence and similar response pattern can also be seen in the second and third story. At a SF of 1.5, gaps B and F experience a decrease in the first inter-story drift of about 50% and 22% respectively. Meanwhile, gap C's best performance corresponds to a reduction of about 41% at a SF of 1.25. At this SF, a small reduction can also be observed in the third story for gap C and B. Overall, gap C seems to show the greatest divergence in all stories while gap F continue to have the least effect on the reduction of the PS responses. From the figure, the FIS exhibits great absorption performance after impact when it is subjected to Hachinohe. Unlike El Centro, the intensity that corresponds to the greatest gain in FIS acceleration (between a SF of 0.75 and 1 in Figure 3.13(a)) does not necessarily show a reduction in the inter-story drift. As seen in Figure 3.14 between a SF of 0.75 to 1, the opposite has occurred where a slight increase in the PS responses is observed.

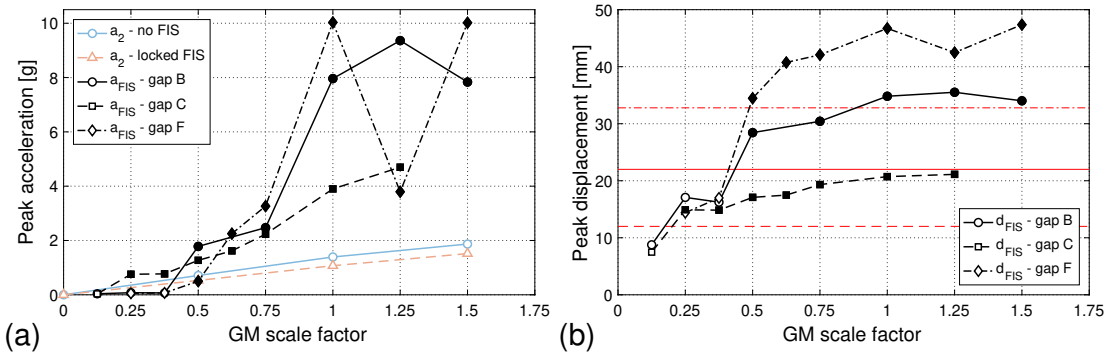


Figure 3.13: Peak FIS responses with different seismic gaps for Hachinohe: (a) total accelerations a_2 and a_{FIS}, and (b) FIS displacement d_{FIS}. The horizontal lines represent the seismic gap for each case (based on line style). The filled markers indicates cases in which impacts occurred in the FIS.

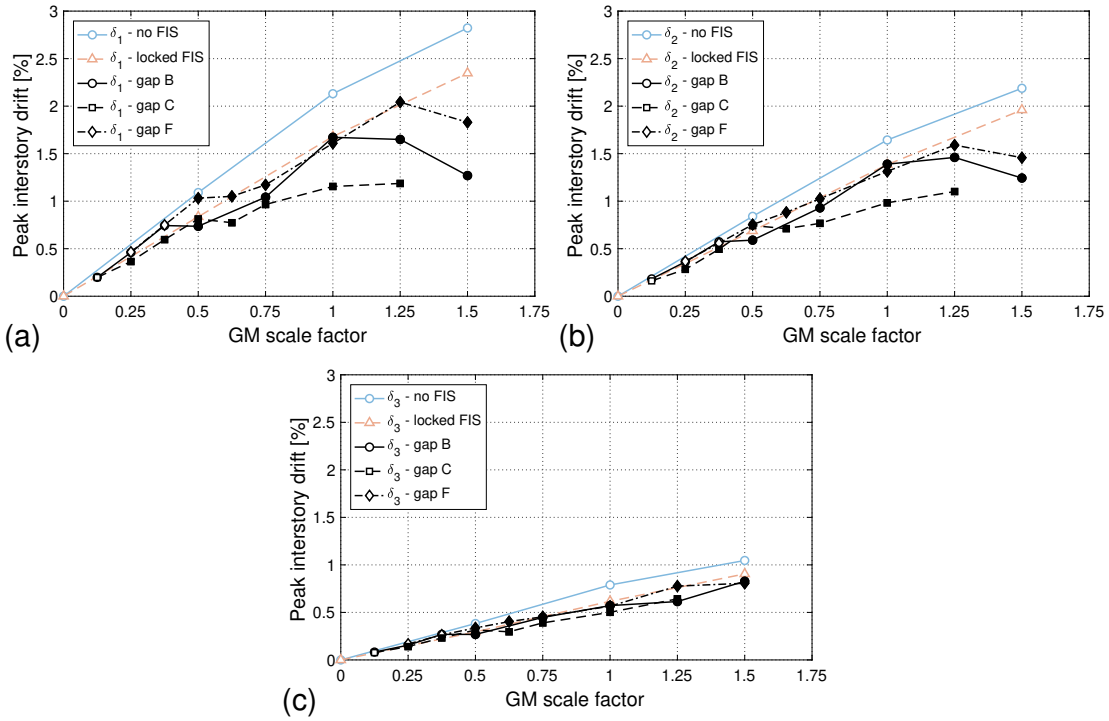


Figure 3.14: Peak PS responses with different seismic gaps for for Hachinohe: (a) 1st story drift δ_1, (b) 2nd story drift δ_2, and (c) 3rd story drift δ_3. The filled markers indicates cases in which impacts occurred in the FIS.

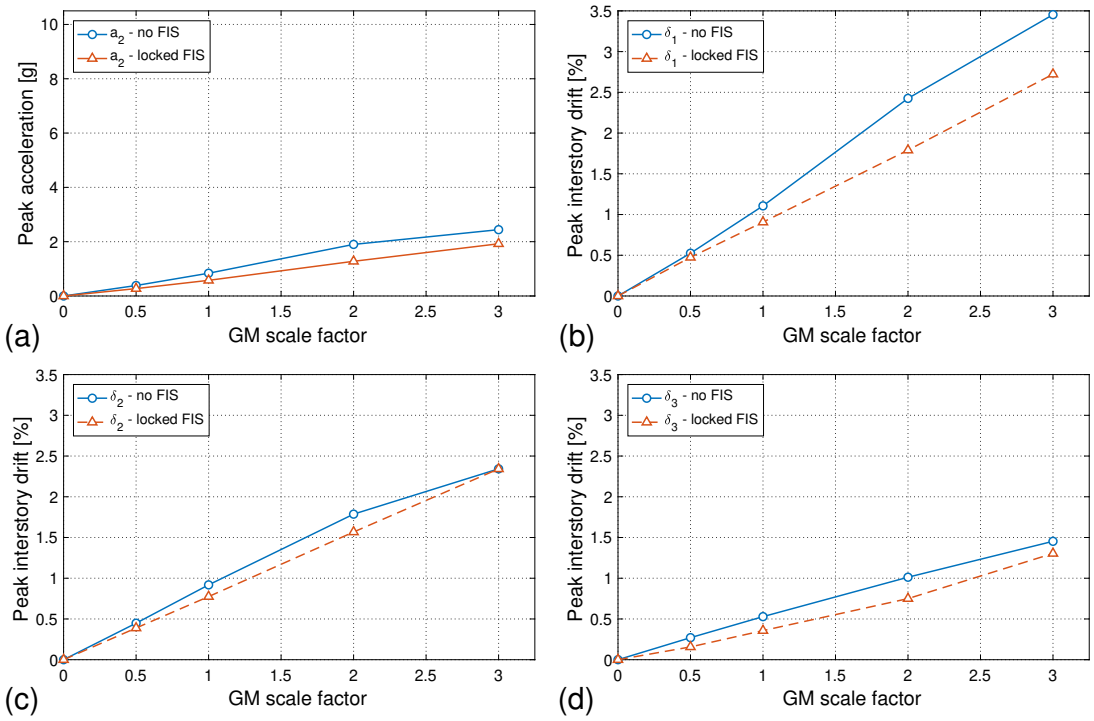


Figure 3.15: Peak responses with no FIS and locked FIS for Kobe: (a) 2nd floor total acceleration a_2, (b) 1st story drift δ_1, (c) 2nd story drift δ_2, and (d) 3rd story drift δ_3.

3.5.3 Kobe

3.5.3(a) Baseline performance

Figure 3.15 shows peak PS responses for the case of no FIS and locked FIS when subjected to Kobe at varying SFs. Overall, the responses are approximately linear for both acceleration and inter-story drifts, which serve as the baseline cases for discussing the isolation and absorption performance respectively for Kobe. Like El Centro and Hachinohe, PS with no FIS exhibits larger responses than the case with locked FIS.

3.5.3(b) Isolation performance

Figure 3.16 shows peak responses of the FIS with different seismic gaps when subjected to Kobe at varying SFs. The FIS acceleration and displacement are shown in Figures 3.16(a) and 3.16(b), respectively. In all cases, a decrease in FIS acceleration can be observed prior to impact. Gap B and F show a reduction of about 87% and 85% re-

spectively at a SF of 1 while gap C also exhibits a decrease in acceleration in its linear response. Notice that gap F continues to show great acceleration reduction even until reaching a GM SF of 1.5. This means, when subjected to Kobe, an FIS with a large seismic gap can exhibit great isolation performance even at high intensity. Therefore, Kobe can be more advantageous for the FIS's isolation performance than the cases of El Centro or Hachinohe as discussed earlier.

However, as expected, Kobe also exhibits an increase in acceleration during and after impact. While gap F shows great isolation performance, it also experiences a drastic gain in acceleration during impact at a SF of 1.75. Gap B and C also show increase in acceleration in the nonlinear range. Therefore, like other GMs, Kobe also exhibits poor isolation performance during and after impact.

In Figure 3.16(b), the FIS displacement increases as the GM SF goes up. From this figure, it is apparent that the FIS indeed experiences impact at a SF of 1.25, 0.5 and 1.75 for gaps B, C and F respectively. Compression in the bumpers as well as additional deflection are also present in this case. For both the acceleration and displacement, there are higher responses as the SF increases.

3.5.3(c) Absorption performance

Figure 3.17 shows peak inter-story drift of the PS with different seismic gaps at varying GM SFs. For all stories, the linear responses of the three gaps resemble the baseline cases (no FIS and locked FIS) quite well in exception of gap F in the first story where it has higher inter-story drift at a SF of 1.5. Overall, impacts seem to have very little effect on the PS responses especially in the second story where the data of all the three gaps lie almost perfectly on the locked FIS line. In the first and third story, there is a small divergence from the linear response at a SF of 3 that is observed for gap B only. This indicates that when the system is subjected to Kobe, it does not exhibit any noticeable absorption performance. Notice that there seems to be no clear correlation between

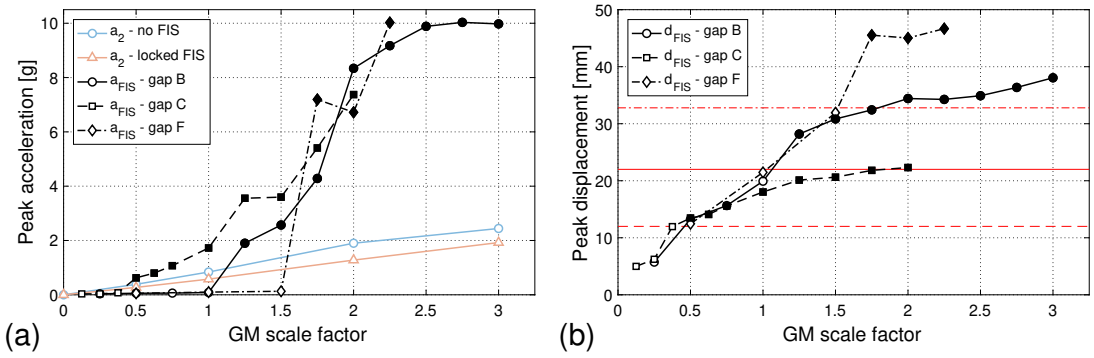


Figure 3.16: Peak FIS responses with different seismic gaps for Kobe: (a) total accelerations a_2 and a_{FIS}, and (b) FIS displacement d_{FIS}. The horizontal lines represent the seismic gap for each case (based on line style). The filled markers indicates cases in which impacts occurred in the FIS.

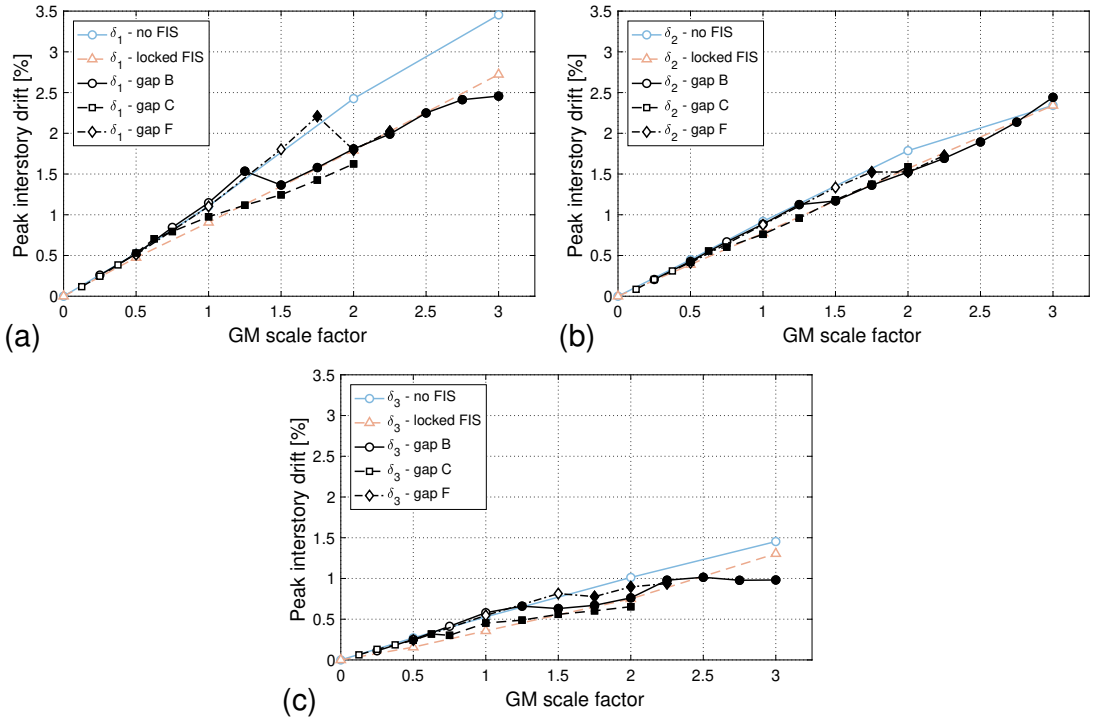


Figure 3.17: Peak PS responses with different seismic gaps for Kobe: (a) 1st interstory drift δ_1, (b) 2nd interstory drift δ_2, and (c) 3rd interstory drift δ_3. The filled markers indicates cases in which impacts occurred in the FIS.

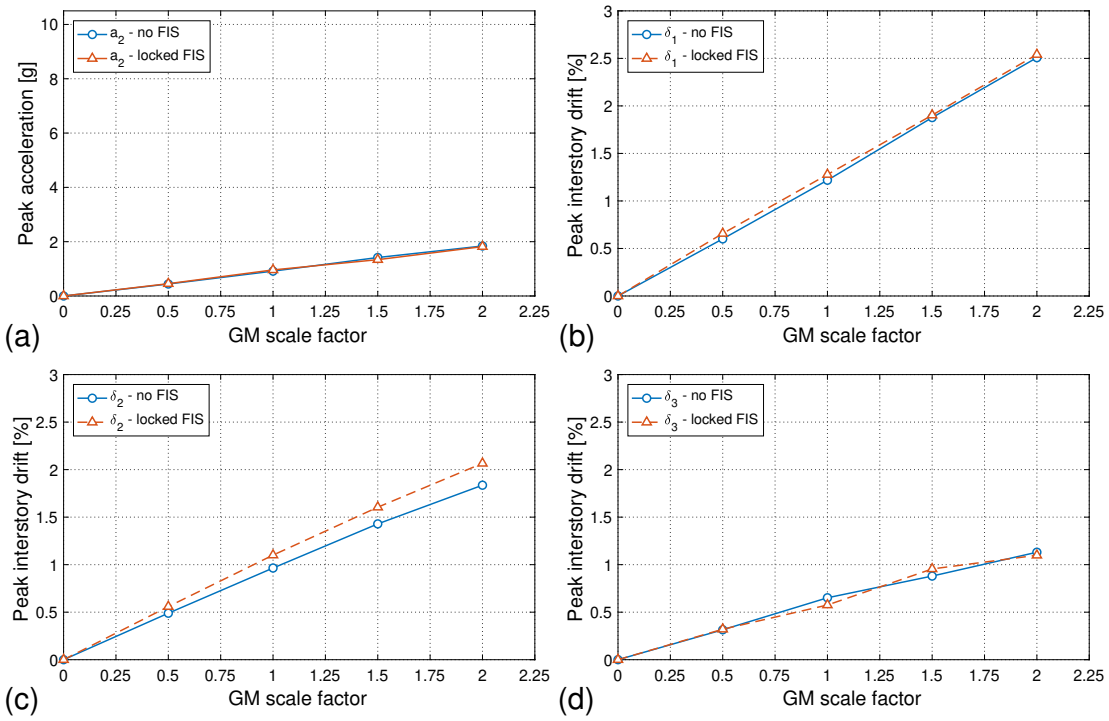


Figure 3.18: Peak responses with no FIS and locked FIS for Northridge: (a) 2nd floor total acceleration a_2, (b) 1st story drift δ_1, (c) 2nd story drift δ_2, and (d) 3rd story drift δ_3.

the gain in FIS acceleration as shown in Figure 3.16 to how it affects the absorption performance in Figure 3.17. Therefore, unlike El Centro and Hachinohe, Kobe overall has negligible effect on the absorption performance of the FIS both during and after impact.

3.5.4 Northridge

3.5.4(a) Baseline performance

Figure 3.18 shows the PS responses for the case of no FIS and locked FIS when subjected to Northridge at varying SFs. As shown in Figure 3.18(a), the response of locked FIS and no FIS are almost identical. In Figure 3.18(b), unlike other GMs, the inter-story drift responses for the case of no FIS are overall smaller than those of the locked FIS case. These responses serve as baseline cases for evaluating the isolation and absorption performance of the FIS as discussed in the next sections.

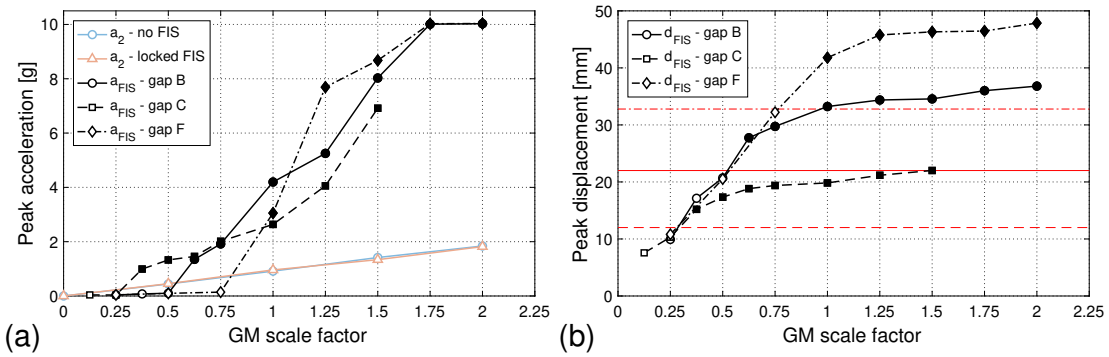


Figure 3.19: Peak FIS responses with different seismic gaps for Northridge: (a) total accelerations a_2 and a_{FIS}, and (b) FIS displacement d_{FIS}. The horizontal lines represent the seismic gap for each case (based on line style). The filled markers indicates cases in which impacts occurred in the FIS.

3.5.4(b) Isolation performance

Figure 3.19 shows peak responses of the FIS with different gaps at varying GM SFs. The acceleration and displacement responses are shown in Figures 3.19(a) and 3.19(b) respectively. Prior to impact, the FIS acceleration of all three gaps is observed to be smaller than the baseline cases. Thus, like other GMs, Northridge also exhibit isolation performance when the system is linear. However, as expected, an increase in acceleration is observed during and after impact, which results in a poor isolation performance of the FIS when the system is subjected to Northridge.

Peak displacement of the FIS is shown in Figure 3.19(b). With the displacement shown, it can be confirmed that Northridge results in an impact occurring at a SF of 0.625, 0.375 and 1 for gaps B, C and F respectively. Compression in the bumpers and additional deflection are also present for this GM.

3.5.4(c) Absorption performance

Figure 3.20 shows peak inter-story drifts of the PS with different gaps when subjected to Northridge at varying SFs. The linear responses of all cases fit very well to the baseline performance. However, after impact, a small reduction in drift can be observed in all cases. In the first story (Figure 3.20(a)), all three gaps have almost the exact same effect

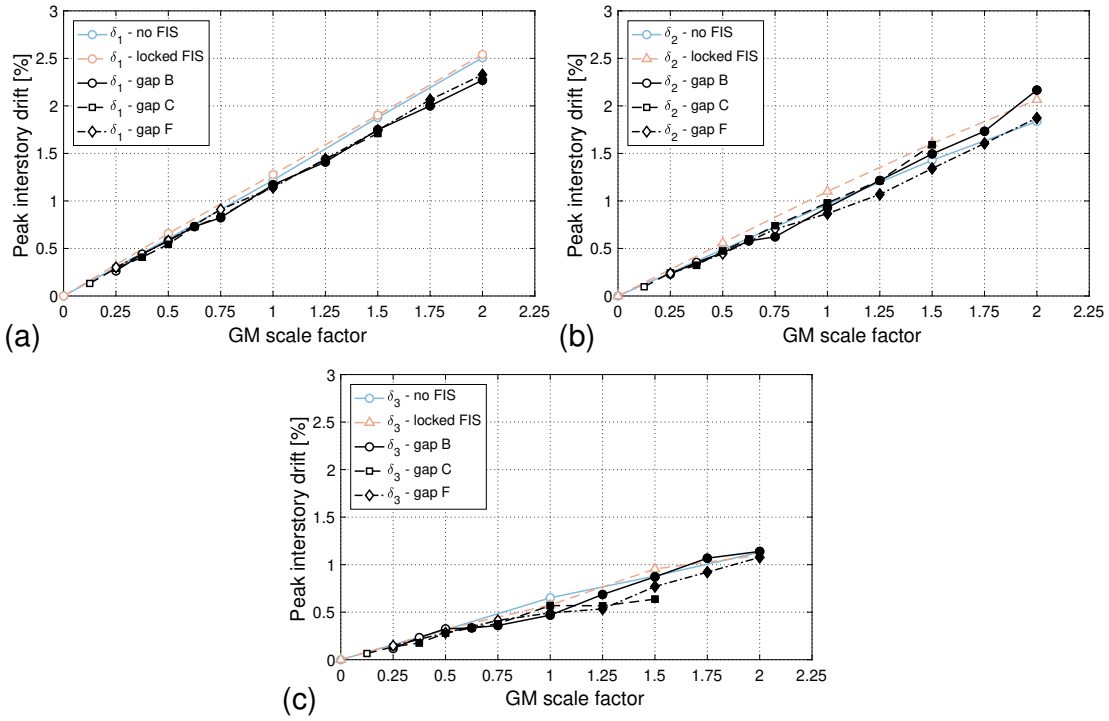


Figure 3.20: Peak PS responses with different seismic gaps for Northridge: (a) 1st interstory drift δ_1, (b) 2nd interstory drift δ_2, and (c) 3rd interstory drift δ_3. The filled markers indicates cases in which impacts occurred in the FIS.

on the PS response where a small reduction in drift is observed. In the second and third stories, gap F exhibits higher reduction in inter-story drift than for the case of gaps B and C after impact. Note that this response is different from other GMs where gap F usually shows the least effect on the absorption performance. Overall, Northridge results in an impact that has very little effect on the absorption performance of the FIS. Similar to Kobe, an increase in FIS acceleration response after impact as shown in Figure 3.19(a) seems to have negligible effect on the PS responses when subjected to Northridge.

3.5.5 Normalized Performance Indices

The isolation and absorption performance of the FIS can also be evaluated by the normalized isolation performance index (J_a) and normalized absorption performance index (J_δ) respectively as defined in Section 3.2.5.

Figure 3.21 shows the normalized isolation performance index for the case with

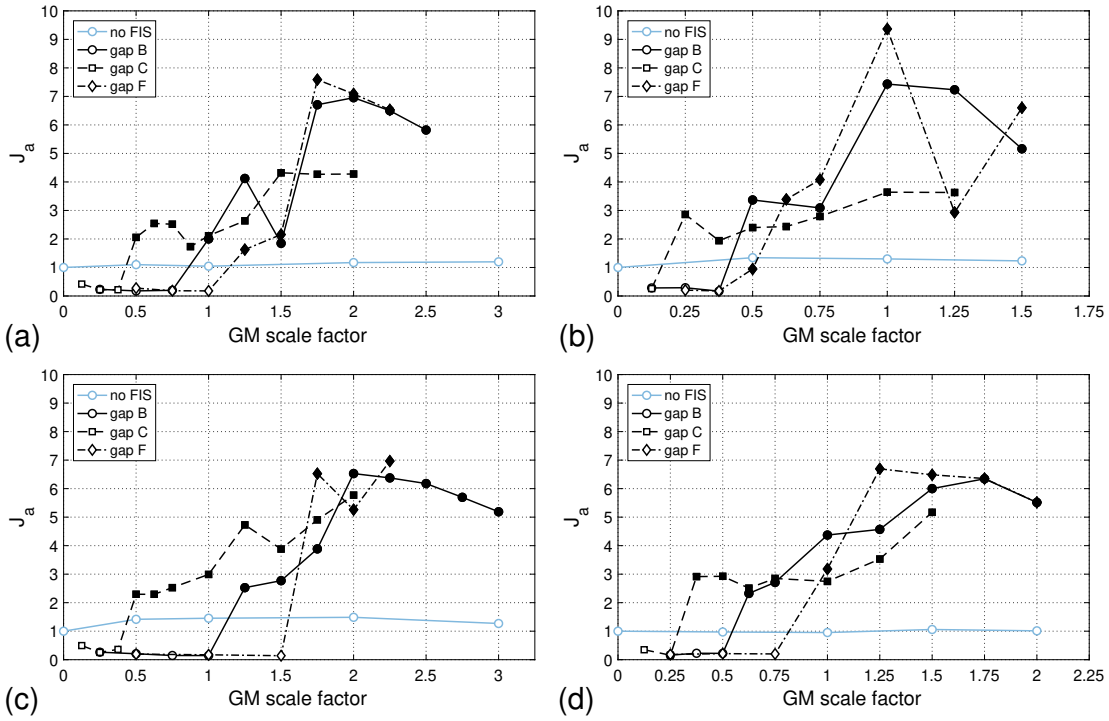


Figure 3.21: Peak total acceleration performance index J_a for (a) El Centro, (b) Hachinohe, (c) Kobe, and (d) Northridge. The filled markers indicates cases in which impacts occurred in the FIS.

no FIS and and with FIS gaps when subjected to different GMs at varying SFs. Note that since these values are normalized by a_2^{locked}, points below 1 indicate good isolation performance whereas points above 1 indicate poor isolation performance relative to the locked FIS case. Prior to impacts, all GMs indicate great isolation performance. However, during and after impact, the FIS performs poorly as an isolator due to a drastic gain in acceleration as shown in Figure 3.21. Notice that while gap F can generally isolate at higher intensity, it also exhibits the greatest gain in acceleration after impact. This is because the larger gap allows for greater velocities to develop before impact, resulting in harsher impacts with higher accelerations. For El Centro, Hachinohe and Kobe, the case of no FIS lies above 1 indicating that the addition of mass to the second floor helps reduce the second's floor acceleration. However, this seems to be not true for Northridge GM since the case of no FIS stays perfectly at a value of 1.

Figure 3.22 shows the normalized absorption performance index for the case with

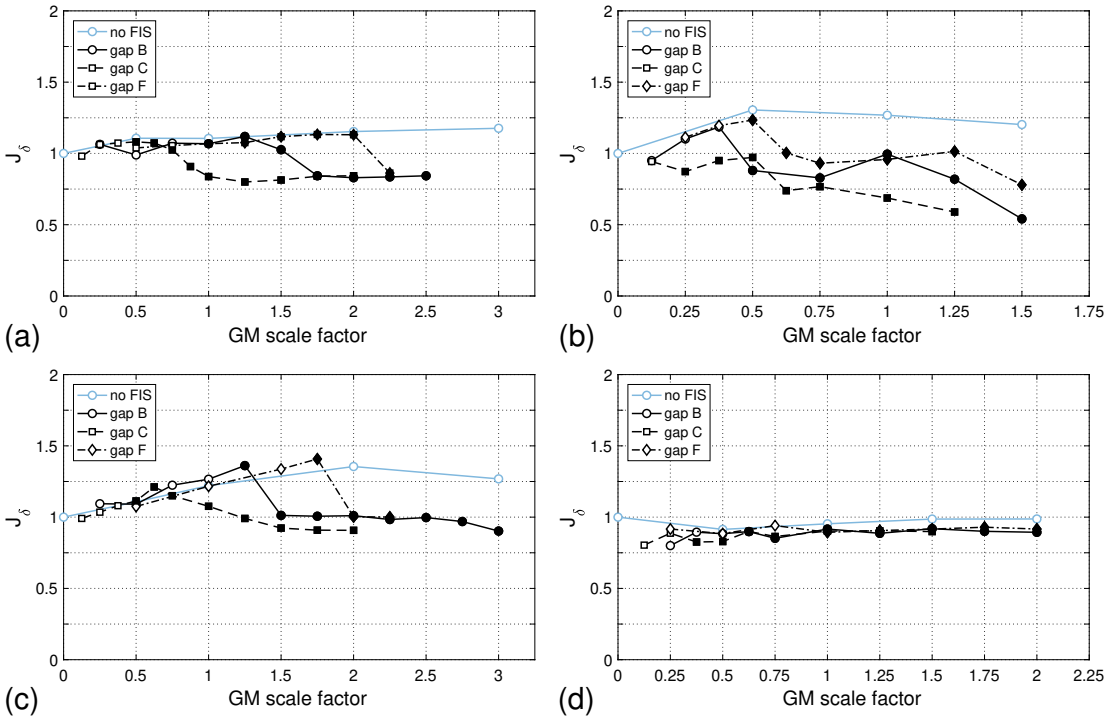


Figure 3.22: Peak interstory drift performance index J_δ for (a) El Centro, (b) Hachinohe, (c) Kobe, and (d) Northridge. The filled markers indicates cases in which impacts occurred in the FIS.

no FIS and with FIS gaps when subjected to different GMs at varying SFs. Since these values are normalized by δ_1^{locked}, points below 1 indicate good absorption performance whereas points above 1 indicate poor absorption performance relative to the locked FIS case. Prior to impact, PS responses for El Centro, Hachinohe and Kobe indicate an increase in inter-story drift while Northridge's response stays constant throughout where a small reduction in drift can be observed both before and after impact. During impact, El Centro and Kobe continue to show an increase in drift until a certain SF where drift reduction can be noticed. After impact, El Centro and Hachinohe show the highest reduction in drift (20–50%) while Kobe and Northridge have negligible effect overall on the absorption performance. For the first three GMs, gap C seems most influential on the drift reduction. Overall, gap B outperforms gap F for the absorption performance. Notice that among these four GMs, Hachinohe indicates the best absorption performance, and the reasons accountable for such great performance is discussed in the next

section.

3.5.6 Discussion of the Experimental Results

This section discusses the results of the experiments to investigate the FIS responses to different earthquakes. From earlier sections, it is apparent that El Centro and Hachinohe provide good absorption performance whereas Kobe and Northridge have very little effect on the absorption performance of the FIS. Referring back to the characteristics of the GMs in Section 3.4.2, both El Centro and Hachinohe have relatively higher t_{strong} than Kobe and Northridge even though the latter two have higher PGA values. For this reason, there is time for the absorbers to begin functioning which results in a good absorption performance. Therefore, the longer strong motion duration can be the main reason why El Centro and Hachinohe exhibit greater absorption performance.

To further evaluate the GM characteristics in relation to the FIS performance, spectrograms for gap B of the four GMs based on the accelerations measured at the roof of the PS are shown in Figure 3.23. Notice the horizontal red streaks, representing the amount of energy, presented in each GM. They appear at the frequencies of about 3.5 Hz, 10 Hz and 15 Hz which correspond to the PS's three natural frequencies. In all these cases, a redistribution of energy from the first mode to higher modes can be seen. Due to the nature of higher mode's mode shape, it contributes less to the drift response of the PS. Therefore, a greater energy redistribution to higher modes would correspond to a smaller PS responses. Notice that Hachinohe overall has a relatively higher redistribution of energy to the third mode than as seen with other GMs, which can be another reason why it has the greatest absorption performance.

3.6 Numerical Results

Using the form of the contact force f_c found in the characterization test detailed in Section 3.3.3, the PS-FIS experiment can be numerically modelled using the same GMs

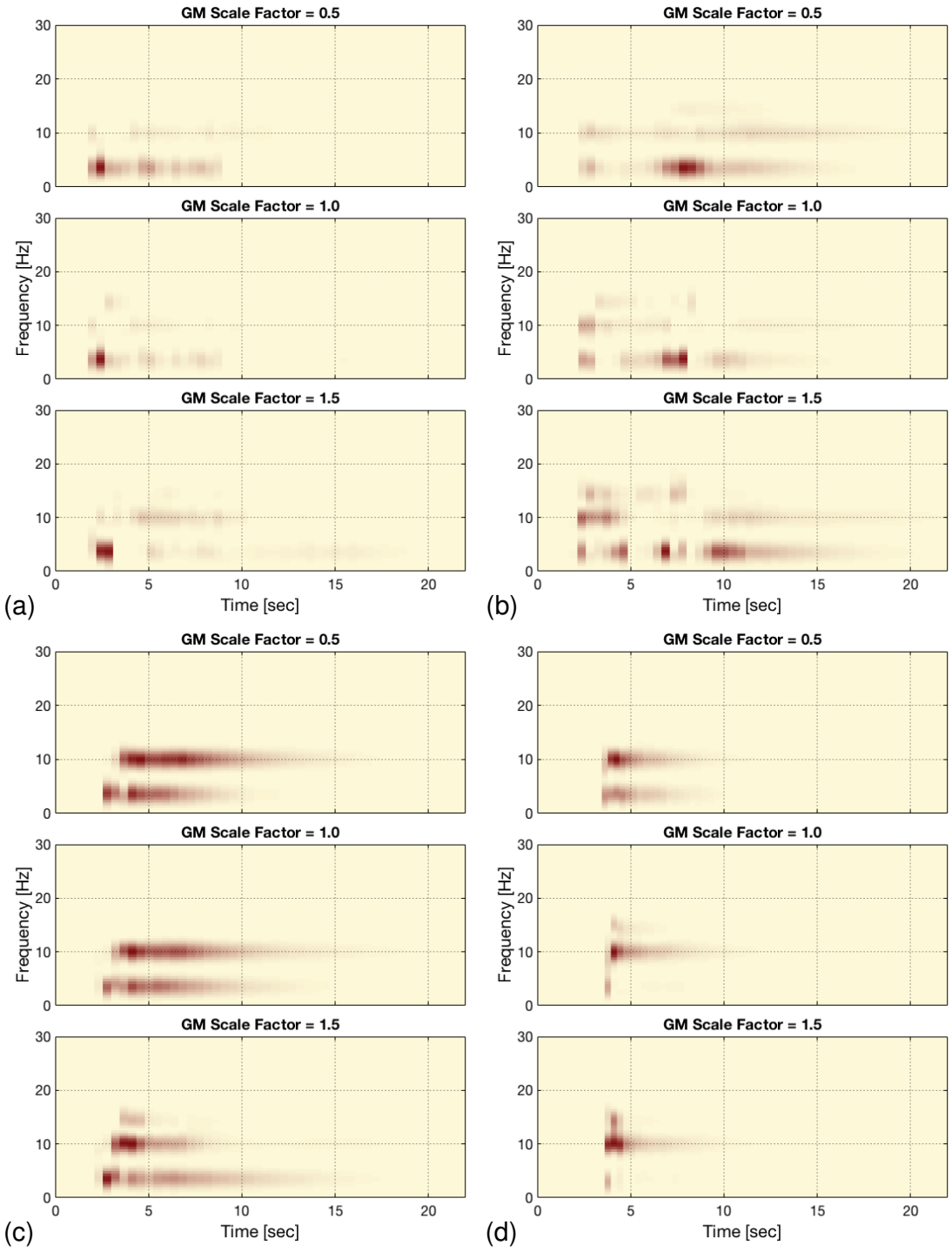


Figure 3.23: Spectrograms of the roof acceleration for gap B subject to (a) El Centro, (b) Hachinohe, (c) Kobe, and (d) Northridge.

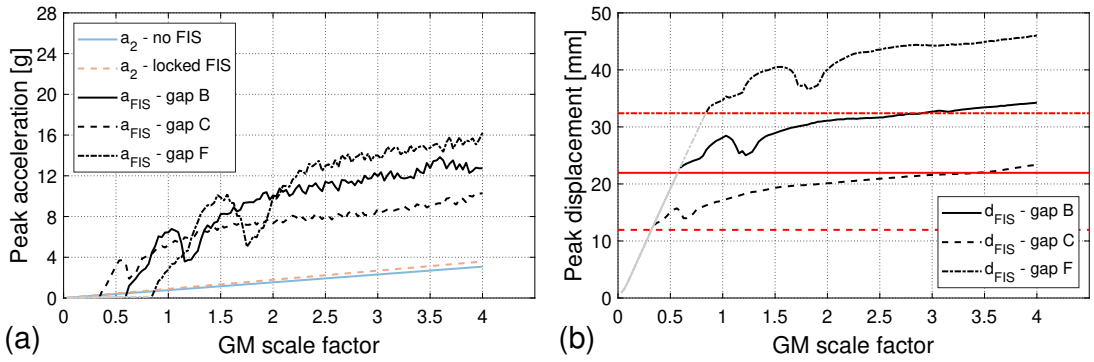


Figure 3.24: Peak FIS responses with different seismic gaps for El Centro: (a) total accelerations a_2 and a_{FIS}, and (b) FIS displacement d_{FIS}. The horizontal lines represent the seismic gap for each case (based on line style). The grey portion indicates cases in which there are no impact whereas the black portion indicates cases in which impacts occurred in the FIS.

and system properties. With ease of numerical simulation, isolation and absorption performance of the FIS can be evaluated at finer increment of intensity SFs under a reasonable time frame.

Using this simulation, the numerical results are obtained and discussed in this section. The peak acceleration and interstory drift responses are plotted in the same format shown in the experimental results. Responses of El Centro are shown in Figures 3.24 and 3.25. Responses of Hachinohe are shown in Figures 3.26 and 3.27. Responses of Kobe are shown in Figures 3.28 and 3.29. Responses of Northridge are shown in Figures 3.30 and 3.31. These results contain overall features that resemble the experimental results except for the baseline cases of El Centro and Hachinohe. From the experiment, the case of locked FIS of these two GMs exhibit lower responses than the case of no FIS. However, the reverse is seen in the numerical results. Baseline cases of Kobe and Northridge are accurately reflected in the numerical results. For the cases with seismic gaps, the responses contain the overall features exhibited in the experiment, with finer details and up to a SF of 4.

The isolation and absorption performance indices are shown in Figures 3.32 and 3.33, respectively. Recall that these data are normalized by the case of locked FIS.

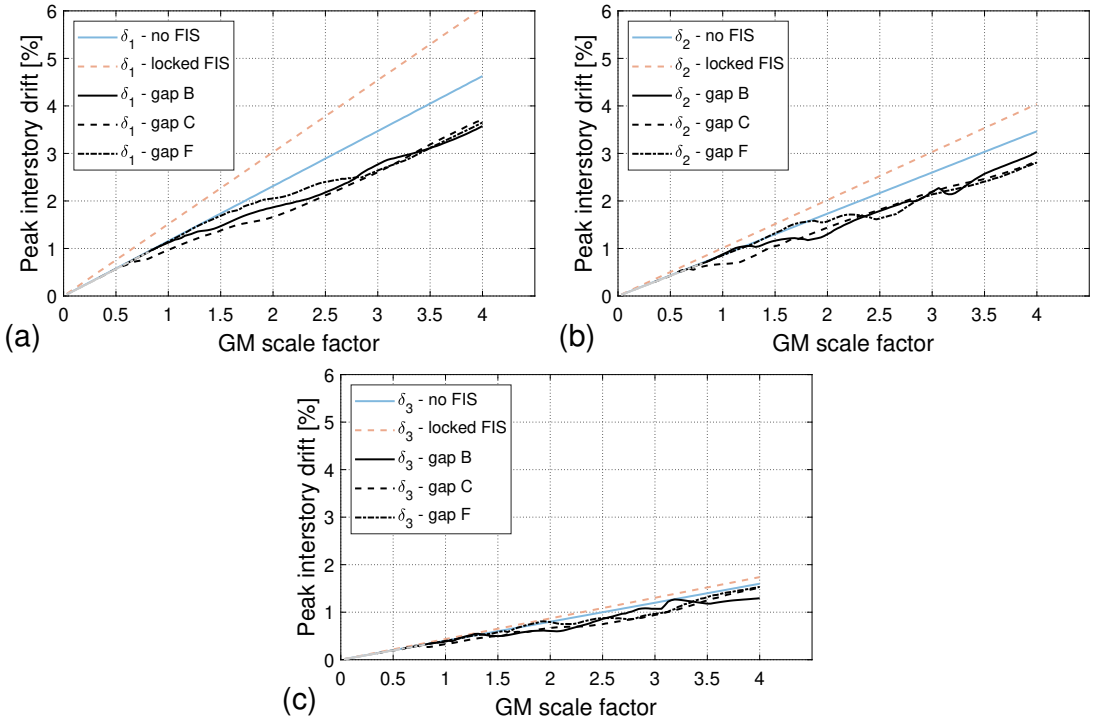


Figure 3.25: Peak PS responses with different seismic gaps for El Centro: (a) 1st interstory drift δ_1, (b) 2nd interstory drift δ_2, and (c) 3rd interstory drift δ_3. The grey portion indicates cases in which there are no impact whereas the black portion indicates cases in which impacts occurred in the FIS.

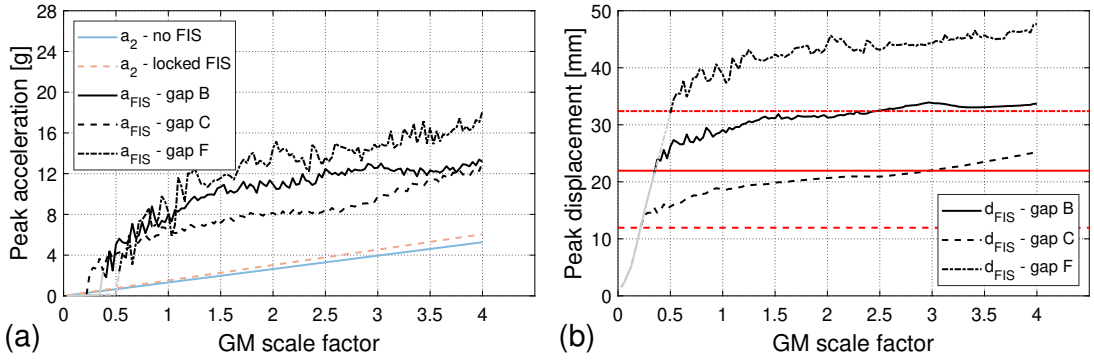


Figure 3.26: Peak FIS responses with different seismic gaps for Hachinohe: (a) total accelerations a_2 and a_{FIS}, and (b) FIS displacement d_{FIS}. The horizontal lines represent the seismic gap for each case (based on line style). The grey portion indicates cases in which there are no impact whereas the black portion indicates cases in which impacts occurred in the FIS.

Therefore, values below 1 for J_a and J_δ exhibit enhanced performance in isolation and absorption respectively. From Figure 3.32, the FIS always exhibits isolation behaviour before impact. However, a huge increase in acceleration can be seen when the FIS experiences impact. After this initial increase, the normalized acceleration fluctuates with

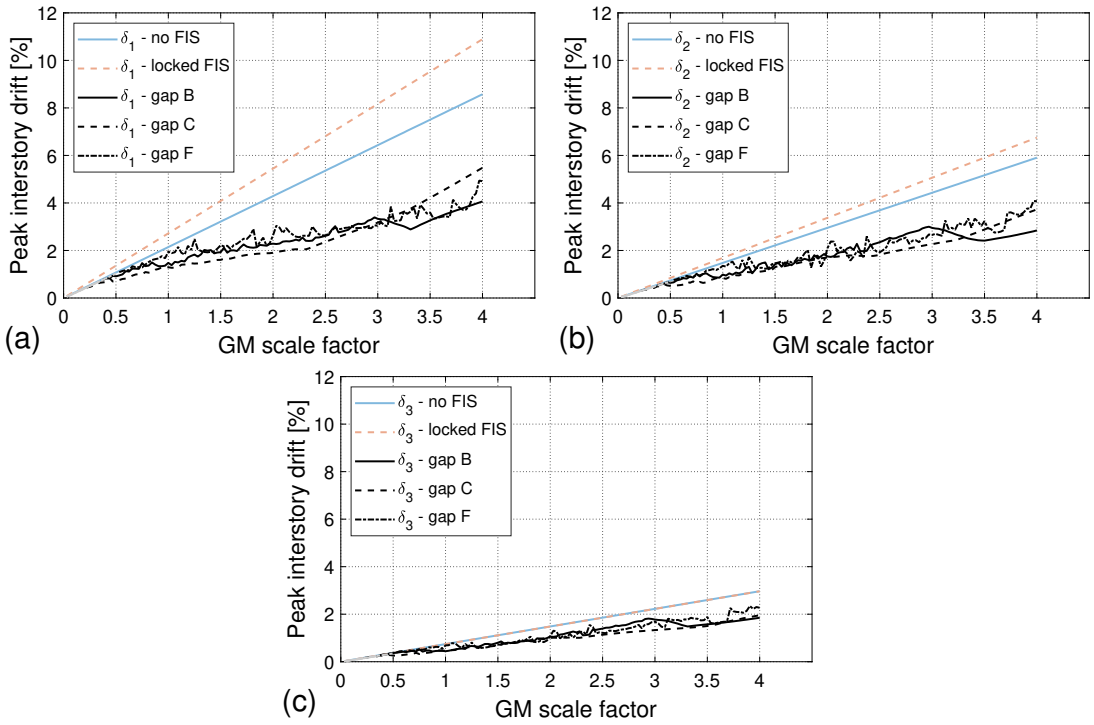


Figure 3.27: Peak PS responses with different seismic gaps for Hachinohe: (a) 1st interstory drift δ_1, (b) 2nd interstory drift δ_2, and (c) 3rd interstory drift δ_3. The grey portion indicates cases in which there are no impact whereas the black portion indicates cases in which impacts occurred in the FIS.

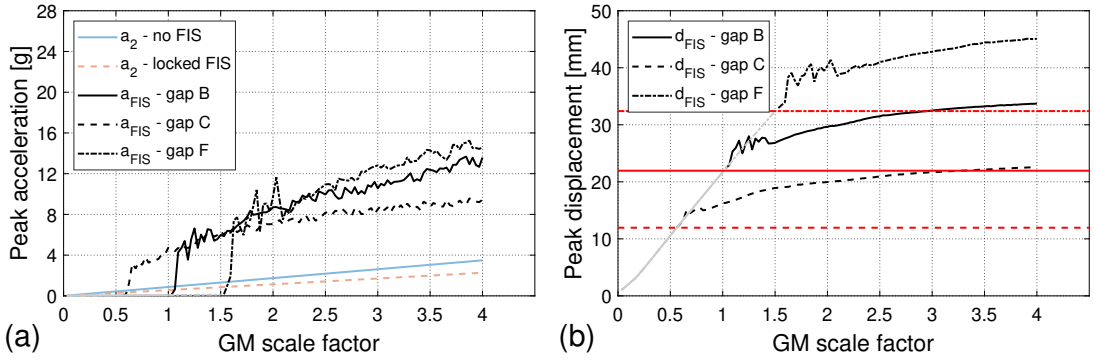


Figure 3.28: Peak FIS responses with different seismic gaps for Kobe: (a) total accelerations a_2 and a_{FIS}, and (b) FIS displacement d_{FIS}. The horizontal lines represent the seismic gap for each case (based on line style). The grey portion indicates cases in which there are no impact whereas the black portion indicates cases in which impacts occurred in the FIS.

an overall decreasing trend as the GM scale factor increases. From Figure 3.33, absorption performance can be observed for El Centro, Hachinohe and Northridge whereas Kobe exhibits poor absorption performance both before and after impact. With respect to the locked FIS, El Centro and Hachinohe exhibit interstory drift reduction both be-

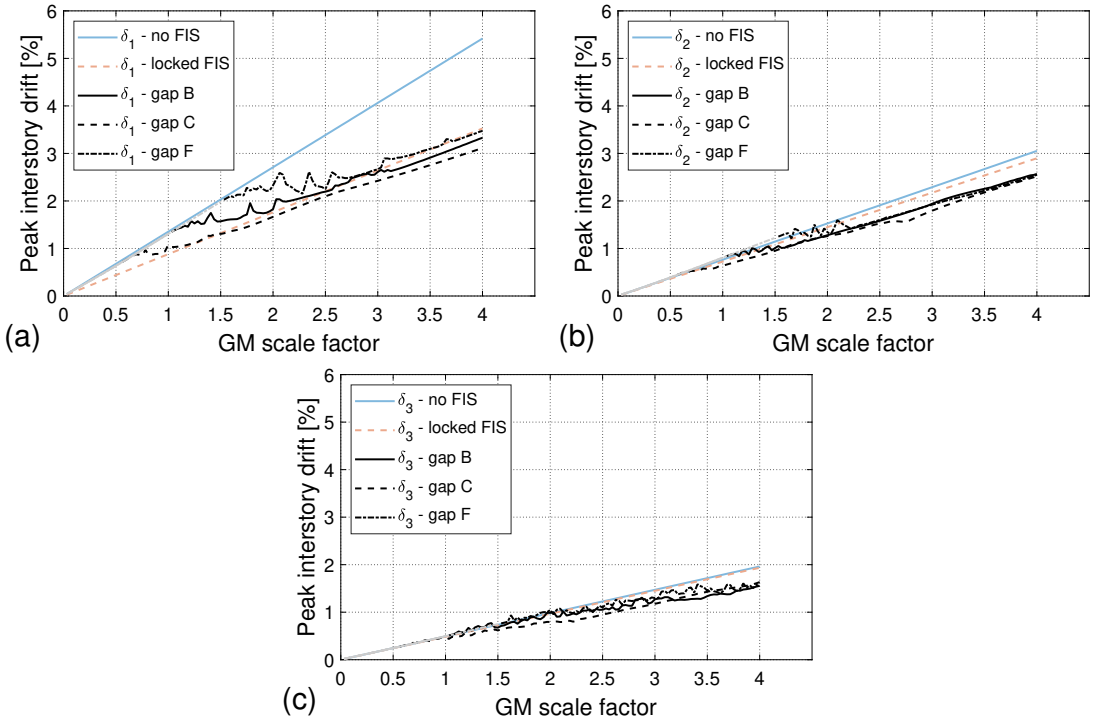


Figure 3.29: Peak PS responses with different seismic gaps for Kobe: (a) 1st interstory drift δ_1, (b) 2nd interstory drift δ_2, and (c) 3rd interstory drift δ_3. The grey portion indicates cases in which there are no impact whereas the black portion indicates cases in which impacts occurred in the FIS.

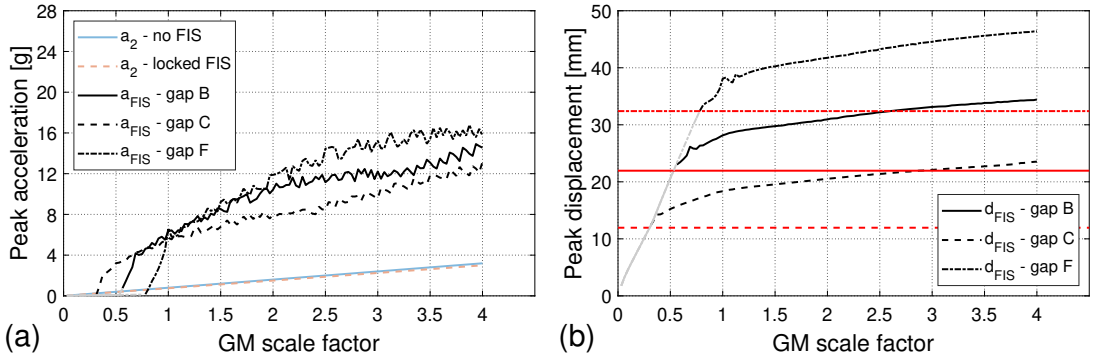


Figure 3.30: Peak FIS responses with different seismic gaps for Northridge: (a) total accelerations a_2 and a_{FIS}, and (b) FIS displacement d_{FIS}. The horizontal lines represent the seismic gap for each case (based on line style). The grey portion indicates cases in which there are no impact whereas the black portion indicates cases in which impacts occurred in the FIS.

fore and after impact. However, great divergence in drift reduction starts to occur after impact. For El Centro (Figure 3.33(a)), the reduction becomes plateaus starting at a SF of 3 for all seismic gaps. For Hachinohe (Figure 3.33(b)), the drift responses continue to decrease until a SF of about 2.5 after which a small increase is observed. For Kobe

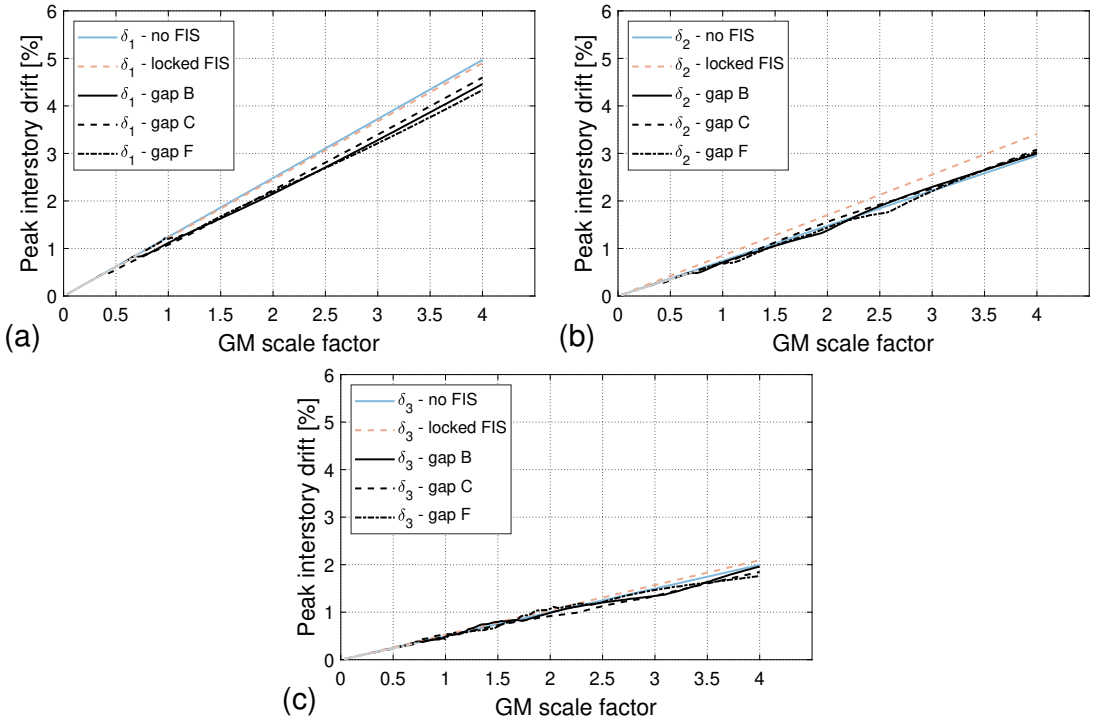


Figure 3.31: Peak PS responses with different seismic gaps for Northridge: (a) 1st interstory drift δ_1, (b) 2nd interstory drift δ_2, and (c) 3rd interstory drift δ_3. The grey portion indicates cases in which there are no impact whereas the black portion indicates cases in which impacts occurred in the FIS.

(Figure 3.33(c)), impact reduces the interstory drift but are not effective enough to reduce the PS's responses compared to the case of locked FIS. For Northridge (Figure 3.33(d)), impacts improve the FIS's absorption performance only at small intensities. As seen in Figure 3.33(d), from a SF of 1 to 4, impacts have no effect on the absorption performance index.

3.7 Summary

Chapter 3 describes the experimental process for conducting lab-scale dual-mode FIS tests as well as evaluates the FIS's isolation and absorption performance by analyzing both the experimental and numerical results.

In summary, a rolling FIS with 250-mm radius of curvature track was mounted onto the second floor of a three-story lab-scale steel structure subjected to four historic ground motions—El Centro, Hachinohe, Kobe, and Northridge. Three seismic gaps—

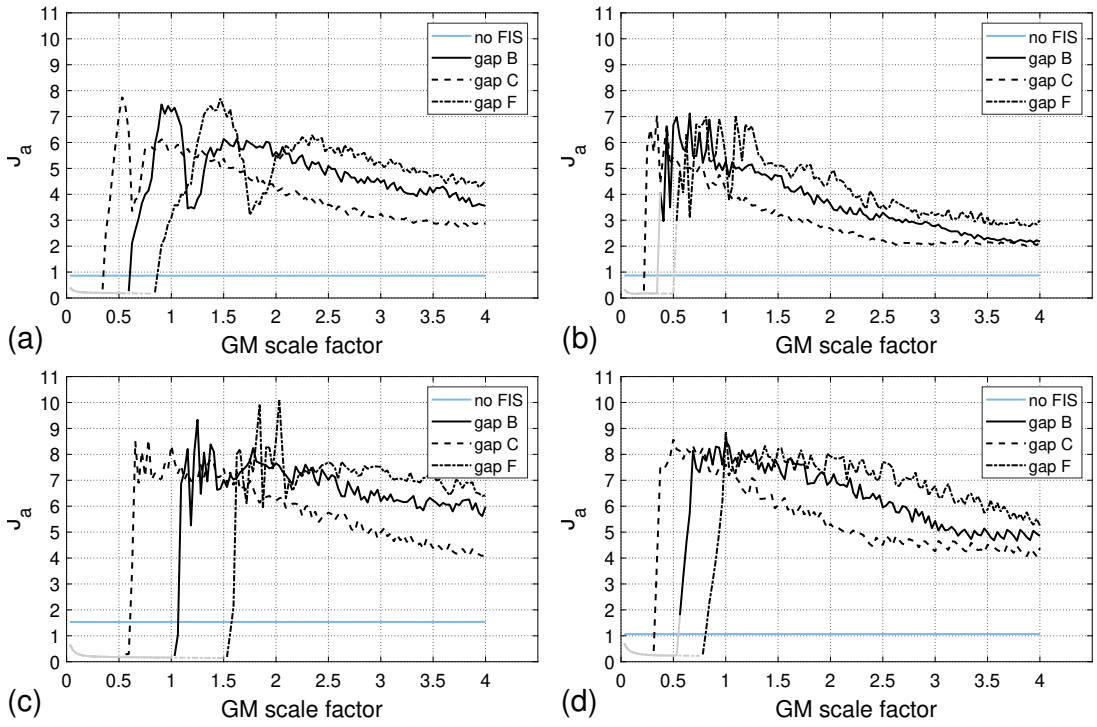


Figure 3.32: Peak total acceleration performance index J_a for (a) El Centro, (b) Hachinohe, (c) Kobe, and (d) Northridge. The grey portion indicates cases in which there are no impact whereas the black portion indicates cases in which impacts occurred in the FIS.

21.95, 11.95, and 32.79 mm—were investigated at varying GM intensity scale factor, which were then compared to baseline cases (i.e., locked FIS and no FIS) in order to evaluate the effectiveness of the FIS as both an isolator and an absorber. The evaluation was conducted using a performance index where the FIS responses are normalized with the responses of locked FIS.

From the experimental and numerical results, the following conclusions can be made: (1) the impact-induced nonlinearity creates a dynamic couple between the FIS and the PS as indicated by the divergence from linear responses, (2) installing a FIS to the PS floor can effectively mitigate seismic response in the isolated content as long as the FIS displacement stays within a linear range, (3) impacts can be harnessed to protect the PS for Hachinohe and El Centro but general ineffective for Kobe and Northridge, (4) while larger seismic gap can isolate more effectively (i.e., at higher intensity SFs),

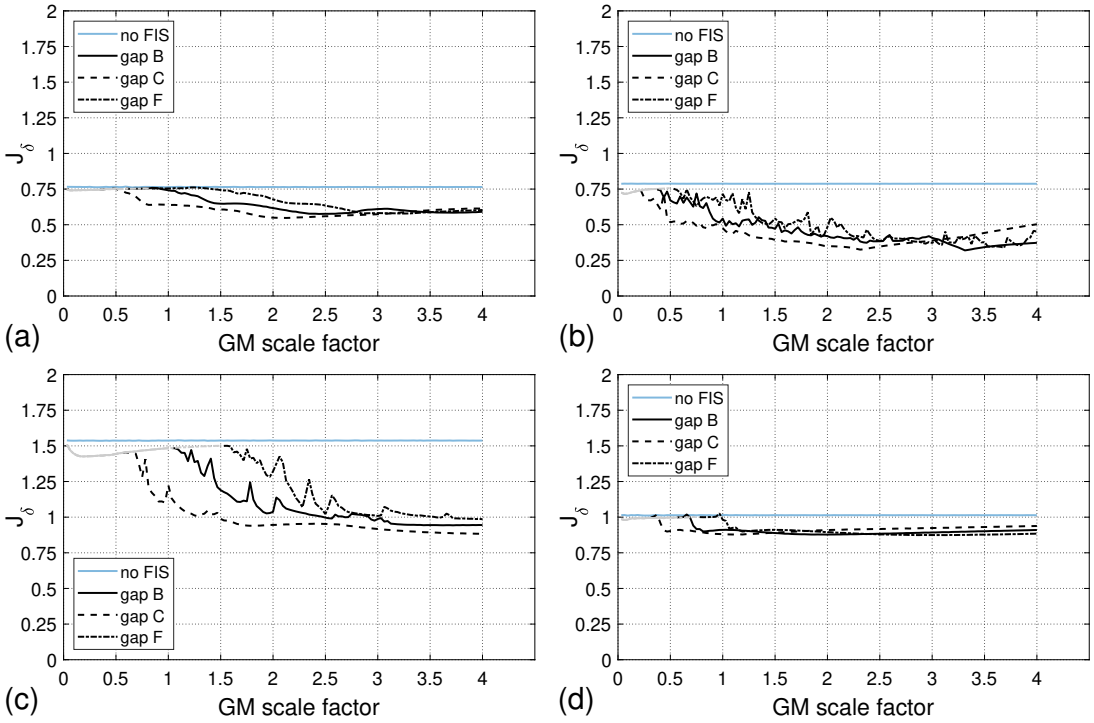


Figure 3.33: Peak interstory drift performance index J_δ for (a) El Centro, (b) Hachinohe, (c) Kobe, and (d) Northridge. The grey portion indicates cases in which there are no impact whereas the black portion indicates cases in which impacts occurred in the FIS.

it does not necessarily provide better absorption performance, (5) smaller seismic gap generally exhibits earlier divergence from the linear response in the absorption performance, (6) higher strong motion duration results in greater absorption performance, and (7) energy redistribution to higher mode in the PS is advantageous to reducing the PS responses.

Chapter 4
Summary, Conclusions, and Future Work

4.1 Summary and Conclusions

The performance evaluation of a dual-mode FIS has been studied using two approaches (probabilistic and experimental) to analyze its behaviour as a vibration isolator in the linear range (i.e., FIS having no impact) and as a vibration absorber in the nonlinear range (i.e., FIS experiencing impacts). Both approaches measure the FIS acceleration response to evaluate isolation performance and the PS interstory drift response to evaluate absorption performance.

The probabilistic approach relies solely on numerical simulation that utilizes a nonlinear reduced order model to ease the computational burden allowing for a more efficient way to collect numerical data within a constraint time frame. This permits critical consideration of many different controlling factors including seismic gap, impact parameters, isolation mass ratio, FIS location, and performance metric parameters via the optimization study that utilizes a 25000-sample Latin hyper cube method and a genetic algorithm. A suite of 50 synthetic ground motions is applied at various hazard levels: service level (SLE), design basis (DBE), and maximum considered earthquake (MCE).

The experimental approach is based on a lab-scale experiment and a numerical simulation that was developed using the same parameters as the experiment. With time constraint, this approach uses four historic ground motions (El Centro, Hachinohe, Kobe and Northridge) at varying intensity scale factors, and considers only seismic gaps as

the controlling factor.

Based on the results from these two approaches, it can be concluded that the FIS is capable of protecting sensitive equipment when it displaces within its allowable capacity. Beyond this limit, a reduction in the primary structure's interstory drift can also be observed in some cases, which results in an FIS that is a *dual-mode vibration isolator/absorber system*.

4.2 Future Work

The results obtained from this research have paved the way for a promising dual-mode seismic isolation system. For the probabilistic approach, future studies should consider the following extensions and their effects on the PS-FIS performance: (1) uncertainty in the properties of the PS, (2) inelasticity within the PS, (3) less flexible MRFs, (4) lateral force resisting systems other than MRFs, (5) nonlinear models for the isolator prior to impact, and (6) other contact models of impact. For the experimental approach, future works should take the following extensions into consideration: (1) FIS responses at other stories (i.e., first floor and roof), (2) different curving track profiles, (3) various isolation mass ratios, (4) different impact parameters (i.e., different shock absorber), (5) using multiple shock absorbers, and (6) numerical optimization study that leads to validation testings.

Bibliography

Anajafi, H. and Medina, R. A. (2018a). "Evaluation of ASCE 7 equations for designing acceleration-sensitive nonstructural components using data from instrumented buildings." *Earthquake Engineering and Structural Dynamics*, 47(4), 1075–1094. doi: 10.1002/eqe.3006.

Anajafi, H. and Medina, R. A. (2018b). "Partial mass isolation system for seismic vibration control of buildings." *Structural Control and Health Monitoring*, 25(2), e2088. doi:10.1002/stc.2088.

Andreaus, U. and De Angelis, M. (2020). "Influence of the characteristics of isolation and mitigation devices on the response of single-degree-of-freedom vibro-impact systems with two-sided bumpers and gaps via shaking table tests." *Structural Control and Health Monitoring*, 27(5), e2517. doi:10.1002/stc.2517.

Arias, A. (1970). "Measure of earthquake intensity." *Report no.*, Massachusetts Inst. of Tech., Cambridge. Univ. of Chile, Santiago de Chile.

ASCE (2017). *Minimum Design Loads and Associated Criteria for Buildings and Other Structures*. American Society of Civil Engineers (ASCE), Reston, VA, ASCE/SEI 7-16 edition.

Baggio, S., Berto, L., Favaretto, T., Saetta, A., and Vitaliani, R. (2015). "Seismic isolation technique of marble sculptures at the Accademia Gallery in Florence: numerical calibration and simulation modelling." *Bulletin of Earthquake Engineering*, 13(9), 2719–2744. doi:10.1007/s10518-015-9741-2.

Becker, T. C., Bao, Y., and Mahin, S. A. (2017). "Extreme behavior in a triple friction pendulum isolated frame." *Earthquake Engineering and Structural Dynamics*, 46(15), 2683–2698. doi:10.1002/eqe.2924.

Bin, P., Tehrani, M. H., Nisa, M., Harvey, Jr, P. S., and Taflanidis, A. A. (n.d.). "Analysis and optimization of a nonlinear dual-mode floor isolation system subjected to earthquake excitations." *Earthquake Engineering & Structural Dynamics* in press, doi: 10.1002/eqe.3449.

Brincker, R., Zhang, L., and Andersen, P. (2001). "Modal identification of output-only systems using frequency domain decomposition." *Smart Materials and Structures*, 10, 441–445. doi:10.1088/0964-1726/10/3/303.

Calhoun, S. J. and Harvey, Jr., P. S. (2018). "Enhancing the teaching of seismic isolation using additive manufacturing." *Engineering Structures*, 167, 494–503. doi: 10.1016/j.engstruct.2018.03.084.

Calhoun, S. J., Tehrani, M. H., and Harvey, Jr, P. S. (2019). "On the performance of double rolling isolation systems." *Journal of Sound and Vibration*, 449, 330–348. doi:10.1016/j.jsv.2019.02.030.

Casey, C. D., Harvey, Jr, P. S., and Song, W. (2018). "Multi-unit rolling isolation system arrays: Analytical model and sensitivity analysis." *Engineering Structures*, 173, 656–668. doi:10.1016/j.engstruct.2018.06.118.

Chen, M. C., Pantoli, E., Wang, X., Astroza, R., Ebrahimian, H., Hutchinson, T. C., Conte, J. P., Restrepo, J. I., Marin, C., Walsh, K. D., Bachman, R. E., Hoehler, M. S., Englekirk, R., and Faghihi, M. (2016). "Full-scale structural and nonstructural building system performance during earthquakes: Part I–specimen description, test protocol, and structural response." *Earthquake Spectra*, 32(2), 737–770. doi: 10.1193/012414EQS016M.

Chen, Y. and Soong, T. T. (1988). "Seismic response of secondary systems." *Engineering Structures*, 10, 218–228. doi:10.1016/0141-0296(88)90043-0.

De Angelis, M., Perno, S., and Reggio, A. (2012). "Dynamic response and optimal design of structures with large mass ratio TMD." *Earthquake Engineering and Structural Dynamics*, 41(1), 41–60. doi:10.1002/eqe.1117.

Deb, K. (2001). *Multi-Objective Optimization using Evolutionary Algorithms*. John Wiley & Sons, Ltd, Chichester, England.

Den Hartog, J. P. (1985). *Mechanical Vibration*. Dover.

Dorman, J. and Prince, P. (1980). "A family of embedded runge-kutta formulae." *Journal of Computational and Applied Mathematics*, 6, 19–26. doi:10.1016/0771-050X(80)90013-3.

Engle, T., Mahmoud, H., and Chulahwat, A. (2015). "Hybrid tuned mass damper and isolation floor slab system optimized for vibration control." *Journal of Earthquake Engineering*, 19, 1197–1221. doi:10.1080/13632469.2015.1037406.

FEMA (2003). *Multi-hazard loss estimation method: Earthquake model: HAZUS MR4 technical manual*. Federal Emergency Management Agency, Washington, D.C.

Fenz, D. M. and Constantinou, M. C. (2008). "Spherical sliding isolation bearings with adaptive behavior: Experimental verification." *Earthquake Engineering and Structural Dynamics*, 37, 185–205. doi:10.1002/eqe.750.

Foutch, D. A. (2000). "State of the art report on performance prediction and evaluation of steel moment-frame buildings." *Report No. FEMA-355F*, Federal Emergency Management Agency (FEMA) (September).

Fu, T. S. and Johnson, E. A. (2011). "Distributed mass damper system for integrating structural and environmental controls in buildings." *Journal of Engineering Mechanics*, 137(3), 205–213. doi:10.1061/(ASCE)EM.1943-7889.0000211.

Gavin, H. P. and Dickinson, B. W. (2011). "Generation of uniform-hazard earthquake ground motions." *Journal of Structural Engineering*, 137, 423–432. doi: 10.1061/(ASCE)ST.1943-541X.0000331.

Gidaris, I., Taflanidis, A. A., Lopez-Garcia, D., and Mavroeidis, G. P. (2016). "Multi-objective risk-informed design of floor isolation systems." *Earthquake Engineering and Structural Dynamics*, 45(8), 1293–1313. doi:10.1002/eqe.2708.

Gourdon, E., Alexander, N. A., Taylor, C. A., Lamarque, C.-H., and Pernot, S. (2007). "Nonlinear energy pumping under transient forcing with strongly nonlinear coupling: Theoretical and experimental results." *Journal of Sound and Vibration*, 300(3-5), 522–551. doi:10.1016/j.jsv.2006.06.074.

Gutierrez Soto, M. and Adeli, H. (2013). "Tuned mass dampers." *Archives of Computational Methods in Engineering*, 20(4), 419–431. doi:10.1007/s11831-013-9091-7.

Hamidi, M. and El Naggar, M. H. (2007). "On the performance of SCF in seismic isolation of the interior equipment of buildings." *Earthquake Engineering and Structural Dynamics*, 36, 1581–1604. doi:10.1002/eqe.708.

Harvey, Jr., P. S. and Elisha, G. (2018). "Vision-based vibration monitoring using existing cameras installed within a building." *Structural Control and Health Monitoring*, 25, e2235. doi:10.1002/stc.2235.

Harvey, Jr., P. S., Elisha, G., and Casey, C. D. (2018). "Experimental investigation of an impact-based, dual-mode vibration isolator/absorber system." *International Journal of Non-Linear Mechanics*, 104, 59–66. doi:10.1016/j.ijnonlinmec.2018.02.013.

Harvey, Jr., P. S. and Gavin, H. P. (2013). "The nonholonomic and chaotic nature of a rolling isolation system." *Journal of Sound and Vibration*, 332, 3535–3551. doi: 10.1016/j.jsv.2013.01.036.

Harvey, Jr., P. S. and Gavin, H. P. (2014a). "Double rolling isolation systems: A mathematical model and experimental validation." *International Journal of Non-Linear Mechanics*, 61, 80–92. doi:10.1016/j.ijnonlinmec.2014.01.011.

Harvey, Jr., P. S. and Gavin, H. P. (2014b). "Truly isotropic biaxial hysteresis with arbitrary knee sharpness." *Earthquake Engineering and Structural Dynamics*, 43, 2051–2057. doi:10.1002/eqe.2436.

Harvey, Jr., P. S., Zéhil, G.-P., and Gavin, H. P. (2014). "Experimental validation of simplified models for rolling isolation systems." *Earthquake Engineering and Structural Dynamics*, 43, 1067–1088. doi:10.1002/eqe.2387.

Housner, G. W., Bergman, L. A., Caughey, T. K., Chassiakos, A. G., Claus, R. O., Masri, S. F., Skelton, R. E., Soong, T. T., Spencer, B. F., and Yao, J. T. P. (1997). "Structural control: Past, present, and future." *Journal of Engineering Mechanics*, 123, 897–971. doi:10.1061/(ASCE)0733-9399(1997)123:9(897).

Hughes, P. J. and Mosqueda, G. (2020). "Evaluation of uniaxial contact models for moat wall pounding simulations." *Earthquake Engineering and Structural Dynamics*, 49(12), 1197–1215. doi:10.1002/eqe.3285.

IBM (2014). "POWER7 Information: Vibration and Shock. Systems Hardware Information (April). Accessed 14 April 2018. URL: https://www.ibm.com/support/knowledgecenter/POWER7/p7ebe/p7ebevibrationandshock.htm.

Igusa, T. and Der Kiureghian, A. (1985). "Dynamic characterization of two-degree-of-freedom equipment-structure systems." *Journal of Engineering Mechanics*, 111, 1–19. doi:10.1061/(ASCE)0733-9399(1985)111:1(1).

Ismail, M., Rodellar, J., and Ikhouane, F. (2009). "An innovative isolation bearing for motion-sensitive equipment." *Journal of Sound and Vibration*, 326, 503–521. doi:10.1016/j.jsv.2009.06.022.

Jia, G., Gidaris, I., Taflanidis, A. A., and Mavroeidis, G. P. (2014). "Reliability-based assessment/design of floor isolation systems." *Engineering Structures*, 78, 41–56. doi:10.1016/j.engstruct.2014.07.031.

Kemeny, Z. A. (1997). "Ball-in-cone rolling isolation systems." U.S. Patent 5599106.

Konstantinidis, D. and Nikfar, F. (2015). "Seismic response of sliding equipment and contents in base-isolated buildings subjected to broadband ground motions." *Earthquake Engineering and Structural Dynamics*, 44(6), 865–887. doi:10.1002/eqe.2490.

Lambrou, V. and Constantinou, M. C. (1994). "Study of seismic isolation systems for computer floors." *Report No. NCEER-94-0020*, National Center for Earthquake Engineering Research.

Liu, S. and Warn, G. P. (2012). "Seismic performance and sensitivity of floor isolation systems in steel plate shear wall structures." *Engineering Structures*, 42, 115–126. doi:10.1016/j.engstruct.2012.04.015.

Lu, L.-Y., Lee, T.-Y., and Yeh, S.-W. (2011). "Theory and experimental study for sliding isolators with variable curvature." *Earthquake Engineering and Structural Dynamics*, 40, 1609–1627. doi:10.1002/eqe.1106.

Luo, J., Wierschem, N. E., Fahnestock, L. A., Bergman, L. A., Spencer, B. F., Al-Shudeifat, M., McFarland, D. M., Quinn, D. D., and Vakakis, A. F. (2014a). "Realization of a strongly nonlinear vibration-mitigation device using elastomeric bumpers." *Journal of Engineering Mechanics*, 140(5), 04014009. doi:10.1061/(ASCE)EM.1943-7889.0000692.

Luo, J., Wierschem, N. E., Hubbard, S. A., Fahnestock, L. A., Quinn, D. D., McFarland, D. M., Spencer Jr, B. F., Vakakis, A. F., and Bergman, L. A. (2014b). "Large-scale experimental evaluation and numerical simulation of a system of nonlinear energy sinks for seismic mitigation." *Engineering Structures*, 77, 34–48. doi: 10.1016/j.engstruct.2014.07.020.

Matta, E. and De Stefano, A. (2009). "Robust design of mass-uncertain rolling-pendulum TMDs for the seismic protection of buildings." *Mechanical Systems and Signal Processing*, 23, 127–147. doi:10.1016/j.ymssp.2007.08.012.

Murudi, M. M. and Mane, S. M. (2004). "Seismic effectiveness of tuned mass damper (TMD) for different ground motion parameters." *13th World Conference on Earthquake Engineering*, Vancouver, B.C., Canada (August 1–6, 2004). Paper No. 2325.

Muthukumar, S. and DesRoches, R. (2006). "A hertz contact model with non-linear damping for pounding simulation." *Earthquake Engineering and Structural Dynamics*, 35(7), 811–828. doi:10.1002/eqe.557.

Naeim, F. and Kelly, J. M. (1999). *Design of seismic isolated structures*. John Wiley & Sons, New York, NY.

Nucera, F., Vakakis, A. F., McFarland, D. M., Bergman, L. A., and Kershen, G. (2007). "Targeted energy transfer in vibro-impact oscillator for seismic mitgation." *Nonlinear Dynamics*, 50, 651–677. doi:10.1007/s11071-006-9189-7.

Ohtori, Y., Christenson, R. E., Spencer, Jr., B. F., and Dyke, S. J. (2004). "Benchmark control problems for seismically excited nonlinear buildings." *Journal of Engineering Mechanics*, 130, 366–385. doi:10.1061/(ASCE)0733-9399(2004)130:4(366).

Pranesh, M. and Sinha, R. (2000). "VFPI: an isolation device for aseismic design." *Earthquake Engineering and Structural Dynamics*, 29, 603–627. doi:10.1002/(SICI)1096-9845(200005)29:5⟨603::AID-EQE927⟩3.3.CO;2-N.

Rawlinson, T. A., Marshall, J. D., Ryan, K. L., and Zargar, H. (2015). "Development and experimental evaluation of a passive gap damper device to prevent pounding in base-isolated structures." *Earthquake Engineering and Structural Dynamics*, 44(11), 1661–1675. doi:10.1002/eqe.2542.

Reggio, A. and De Angelis, M. (2013). "Optimal design of an equipment isolation system with nonlinear hysteretic behaviour." *Earthquake Engineering and Structural Dynamics*, 42(13), 1907–1930. doi:10.1002/eqe.2304.

Reggio, A. and De Angelis, M. (2014). "Combined primary-secondary system approach to the design of an equipment isolation system with high-damping rubber bearings." *Journal of Sound and Vibration*, 333(9), 2386–2403. doi:10.1016/j.jsv.2013.12.006.

Reggio, A. and De Angelis, M. (2015). "Optimal energy-based seismic design of non-conventional tuned mass damper (tmd) implemented via inter-story isolation." *Earthquake Engineering and Structural Dynamics*, 44(10), 1623–1642. doi:10.1002/eqe.2548.

Ryan, K. L., Soroushian, S., Maragakis, E., Sato, E., Sasaki, T., and Okazaki, T. (2016). "Seismic simulation of an integrated ceiling-partition wall-piping system at E-Defense. I: Three-dimensional structural response and base isolation." *Journal of Structural Engineering*, 142(2), 04015130. doi:10.1061/(ASCE)ST.1943-541X.0001384.

SAC Steel Project (1994). Technical Office, Richmond, CA 94804-4698. URL: http://www.sacsteel.org/ (last accessed 4 May 2021).

Shampine, L., Gladwell, I., and Brankin, R. (1991). "Reliable solution of special event location problems for ODEs." *ACM Transactions on Mathematical Software*, 17, 11–25. doi:10.1145/103147.103149.

Shampine, L. F. and Reichelt, M. W. (1997). "The MATLAB ODE suite." *SIAM Journal on Scientific Computing*, 18(1), 1–22. doi:10.1137/S1064827594276424.

Shi, Y., Kurata, M., and Nakashima, M. (2014). "Disorder and damage of base-isolated medical facilities when subjected to near-fault and long-period ground motions." *Earthquake Engineering and Structural Dynamics*, 43(11), 1683–1701. doi:10.1002/eqe.2417.

Soni, D. P., Mistry, B. B., Jangid, R. S., and Panchel, V. R. (2011). "Seismic response of the double variable frequency pendulum isolator." *Structural Control and Health Monitoring*, 18, 450–470. doi:10.1002/stc.384.

Taflanidis, A. A. and Beck, J. L. (2008). "An efficient framework for optimal robust stochastic system design using stochastic simulation." *Computer Methods in Applied Mechanics and Engineering*, 198(1), 88–101 Computational Methods in Optimization Considering Uncertainties, doi:10.1016/j.cma.2008.03.029.

Tehrani, M. H. (2019). "Design and assessment of innovative dual-mode rolling isolation systems. Ph.D. Dissertation, University of Oklahoma.

Tehrani, M. H. and Harvey, Jr., P. S. (2019). "Enhanced passive control of dual-mode systems under extreme seismic loading: an optimal control approach." *Structural Control and Health Monitoring*, 26(7), e2367. doi:10.1002/stc.2367.

Tehrani, M. H., Harvey, Jr, P. S., Mirza, A. M., and Gavin, H. P. (2018). "Inelastic condensed dynamic models for estimating seismic demands for buildings." *Engineering Structures*, 177, 616–629. doi:10.1016/j.engstruct.2018.07.083.

Trifunac, M. D. and Brady, A. G. (1975). "A study on the duration of strong earthquake ground motion." *Bulletin of the Seismological Society of America*, 65(3), 581–626.

Tsai, C. S., Lin, Y.-C., Chen, W.-S., and Su, H. C. (2010). "Tri-directional shaking table tests of vibration sensitive equipment with static dynamics interchangeable-ball pendulum system." *Earthquake Engineering and Engineering Vibration*, 9, 103–112. doi:10.1007/s11803-010-9009-4.

Wang, J., Wang, B., Wierschem, N. E., and Spencer Jr, B. F. (2020). "Dynamic analysis of track nonlinear energy sinks subjected to simple and stochastice excitations." *Earthquake Engineering and Structural Dynamics*, 49(9), 863–883. doi: 10.1002/eqe.3268.

Wang, J., Wierschem, N. E., Spencer, B. F., and Lu, X. (2015a). "Experimental study of track nonlinear energy sinks for dynamic response reduction." *Engineering Structures*, 94, 9–15. doi:10.1016/j.engstruct.2015.03.007.

Wang, J., Wierschem, N. E., Spencer, B. F., and Lu, X. (2015b). "Track nonlinear energy sink for rapid response reduction in building structures." *Journal of Engineering Mechanics*, 141(1), 04014104. doi:10.1061/(ASCE)EM.1943-7889.0000824.

Wang, J., Wierschem, N. E., Spencer, B. F., and Lu, X. (2016). "Numerical and experimental study of the performance of a single-sided vibro-impact track nonlinear energy sink." *Earthquake Engineering and Structural Dynamics*, 45, 635—-652. doi: 10.1002/eqe.2677.

Warn, G. P. and Ryan, K. L. (2012). "A review of seismic isolation for buildings: Historical development and research needs." *Buildings*, 2, 300–325. doi: 10.3390/buildings2030300.

Wiebe, R. and Harvey, Jr, P. S. (2019). "On the Euler-Lagrange equation for systems of rigid-bodies or lumped masses." *Journal of Computational and Nonlinear Dynamics*, 14(9), 094502. doi:10.1115/1.4044145.

Wierschem, N. E., Quinn, D. D., Hubbard, S. A., Al-Shudeifat, M. A., McFarland, D. M., Luo, J., Spencer, B. F., Vakakis, A. F., and Bergman, L. A. (2012). "Equivalent modal damping, stiffening and energy exchanges in multi-degree-of-freedom systems with strongly nonlinear attachments." *Journal of Multi-body Dynamics*, 226(2), 122–146. doi:10.1177/1464419311432671.

Wright, J. P. and Pei, J. (2012). "Solving dynamical systems involving piecewise restoring force using state event location." *Journal of Engineering Mechanics*, 138. doi:10.1061/(ASCE)EM.1943-7889.0000404.

Xiang, P. and Nishitani, A. (2014). "Seismic vibration control of building structures with multiple tuned mass damper floors integrated." *Earthquake Engineering and Structural Dynamics*, 43(6), 909–925. doi:10.1002/eqe.2379.

Yang, T., Calvi, P. M., and Wiebe, R. (2020). "Numerical implementation of variable friction sliding base isolators and preliminary experimental results." *Earthquake Spectra*, 36(2), 767–787. doi:10.1177/8755293019891721.

Zare Hosseinzadeh, A., Tehrani, M. H., and Harvey, Jr, P. S. (2021). "Modal identification of building structures using vision-based measurements from multiple interior surveillance cameras." *Engineering Structures*, 288, 111517. doi:10.1016/j.engstruct.2020.111517.

Zargar, H., Ryan, K. L., and Marshall, J. D. (2013). "Feasibility study of a gap damper to control seismic isolator displacements in extreme earthquakes." *Structural Control and Health Monitoring*, 20(8), 1159–1175. doi:10.1002/stc.1525.

Zargar, H., Ryan, K. L., Rawlinson, T. A., and Marshall, J. D. (2017). "Evaluation of a passive gap damper to control displacements in a shaking test of a seismically isolated three-story frame." *Earthquake Engineering and Structural Dynamics*, 46(1), 51–71. doi:10.1002/eqe.2771.

Ziyaeifar, M. and Noguchi, H. (1998). "Partial mass isolation in tall buildings." *Earthquake Engineering and Structural Dynamics*, 27(1), 49–65. doi:10.1002/(SICI)1096-9845(199801)27:1⟨49::AID-EQE718⟩3.0.CO;2-J.

Appendix A
State Space Formulation

Assuming the FIS response is in the linear range ($|d| \leqslant d_o$), Equation (2.3) can be written in matrix form as follows:

$$\begin{bmatrix} \hat{\mathbf{M}} + m\hat{\mathbf{p}}\hat{\mathbf{p}}^{\mathrm{T}} & m\hat{\mathbf{p}} \\ m\hat{\mathbf{p}}^{\mathrm{T}} & m \end{bmatrix} \begin{Bmatrix} \ddot{\boldsymbol{\eta}}(t) \\ \ddot{d}(t) \end{Bmatrix} + \begin{bmatrix} \hat{\mathbf{C}} & \mathbf{0}_{r\times 1} \\ \mathbf{0}_{1\times r} & c \end{bmatrix} \begin{Bmatrix} \dot{\boldsymbol{\eta}}(t) \\ \dot{d}(t) \end{Bmatrix} + \begin{bmatrix} \hat{\mathbf{K}} & \mathbf{0}_{r\times 1} \\ \mathbf{0}_{1\times r} & k \end{bmatrix} \begin{Bmatrix} \boldsymbol{\eta}(t) \\ d(t) \end{Bmatrix} = - \begin{Bmatrix} \hat{\boldsymbol{\Gamma}} + m\hat{\mathbf{p}} \\ m \end{Bmatrix} \ddot{u}_{\mathrm{g}}(t) \tag{A.1}$$

The state-space representation of the linear PS-FIS system in Equation (A.1) is given by

$$\dot{\mathbf{x}}(t) = \mathbf{A}\mathbf{x}(t) + \mathbf{B}\ddot{u}_{\mathrm{g}}(t) \tag{A.2}$$

where $\mathbf{x}(t) = [\boldsymbol{\eta}^{\mathrm{T}}(t) \;\; d(t) \;\; \dot{\boldsymbol{\eta}}^{\mathrm{T}}(t) \;\; \dot{d}(t)]^{\mathrm{T}} \in \mathbb{R}^{2r+2}$ is the state vector. The matrices in Equation (A.2) are defined as

$$\mathbf{A} = \begin{bmatrix} \mathbf{0}_{(r+1)\times(r+1)} & \mathbf{I}_{(r+1)} \\ -\mathbf{M}_{\text{PS-FIS}}^{-1}\mathbf{K}_{\text{PS-FIS}} & -\mathbf{M}_{\text{PS-FIS}}^{-1}\mathbf{C}_{\text{PS-FIS}} \end{bmatrix}, \mathbf{B} = \begin{Bmatrix} \mathbf{0}_{(r+1)\times 1} \\ -\mathbf{M}_{\text{PS-FIS}}^{-1}\boldsymbol{\Gamma}_{\text{PS-FIS}} \end{Bmatrix} \tag{A.3}$$

In these expressions, $\mathbf{I}_a$ is the identity matrix of dimension a, $\mathbf{0}_{a\times b}$ is the zero matrix of dimension $a \times b$, and the PS-FIS matrices are given by

$$\mathbf{M}_{\text{PS-FIS}} = \begin{bmatrix} \hat{\mathbf{M}} + m\hat{\mathbf{p}}\hat{\mathbf{p}}^{\mathrm{T}} & m\hat{\mathbf{p}} \\ m\hat{\mathbf{p}}^{\mathrm{T}} & m \end{bmatrix}, \mathbf{C}_{\text{PS-FIS}} = \begin{bmatrix} \hat{\mathbf{C}} & \mathbf{0}_{r\times 1} \\ \mathbf{0}_{1\times r} & c \end{bmatrix},$$
$$\mathbf{K}_{\text{PS-FIS}} = \begin{bmatrix} \hat{\mathbf{K}} & \mathbf{0}_{r\times 1} \\ \mathbf{0}_{1\times r} & k \end{bmatrix}, \boldsymbol{\Gamma}_{\text{PS-FIS}} = \begin{Bmatrix} \hat{\boldsymbol{\Gamma}} + m\hat{\mathbf{p}} \\ m \end{Bmatrix} \tag{A.4}$$

The response quantities defined in Section 2.3.1 can be written in state-space form,

$$\mathsf{y}(t) = \mathbf{C}\mathbf{x}(t) + \mathsf{D}\ddot{u}_{\mathrm{g}}(t) \tag{A.5}$$

where the output vector $\mathbf{C}$ and feed-through coefficient D are given by

$$\begin{aligned}
\text{relative displacement of FIS:}\quad & \mathbf{C} = \{\mathbf{0}_{1\times r}\ \ 1\ \ \mathbf{0}_{1\times r}\ \ 0\}, \\
& \mathsf{D} = 0 && \text{(A.6a)} \\
\text{total acceleration of FIS:}\quad & \mathbf{C} = \{\mathbf{0}_{1\times r}\ \ 0\ \ \hat{\mathbf{p}}^{\mathrm{T}}\ \ 1\}\mathbf{A}, \\
& \mathsf{D} = 1 + \{\mathbf{0}_{1\times r}\ \ 0\ \ \hat{\mathbf{p}}^{\mathrm{T}}\ \ 1\}\mathbf{B} && \text{(A.6b)} \\
\text{total acceleration of } j\text{th story level:}\quad & \mathbf{C} = \{\mathbf{0}_{1\times r}\ \ 0\ \ \mathbf{p}_j^{\mathrm{T}}\mathbf{\Phi}_r\ \ 0\}\mathbf{A}, \\
& \mathsf{D} = 1 + \{\mathbf{0}_{1\times r}\ \ 0\ \ \mathbf{p}_i^{\mathrm{T}}\mathbf{\Phi}_r\ \ 0\}\mathbf{B} && \text{(A.6c)} \\
j\text{th inter-story drift:}\quad & \mathbf{C} = \{(\mathbf{p}_j - \mathbf{p}_{j-1})\mathbf{\Phi}_r\ \ 0\ \ \mathbf{0}_{1\times r}\ \ 0\}, \\
& \mathsf{D} = 0 && \text{(A.6d)} \\
\text{roof drift:}\quad & \mathbf{C} = \{\mathbf{p}_{\mathrm{roof}}^{\mathrm{T}}\mathbf{\Phi}_r\ \ 0\ \ \mathbf{0}_{1\times r}\ \ 0\}, \\
& \mathsf{D} = 0 && \text{(A.6e)}
\end{aligned}$$

where $\mathbf{p}_j$ and $\mathbf{p}_{\mathrm{roof}}$ are Boolean n-vectors identifying the DOF in the PS model [Equation (2.1a)] associated with the jth-story level and roof displacements relative to the ground, respectively; i.e., $u_j(t) = \mathbf{p}_j^{\mathrm{T}}\mathbf{q}(t)$ and $u_{\mathrm{roof}}(t) = \mathbf{p}_{\mathrm{roof}}^{\mathrm{T}}\mathbf{q}(t)$. The complex transfer function $H(\omega)$ is then given by

$$H(\omega) = \mathbf{C}(j\omega\mathbf{I} - \mathbf{A})^{-1}\mathbf{B} + \mathsf{D} \tag{A.7}$$

where $j = \sqrt{-1}$.

Appendix B
Equilibrium Formulation

Consider the FP bearing shown in Fig. 3.1. The free body diagram (FBD) of the FP bearing in a displaced configuration is shown in Fig. B.1. The normal force N is perpendicular to the slider, and friction acts along the the sliding surface. The direction of these forces is described by the angle θ of the sliding surface at the point of contact, which is related to the sliding surface's shape $h(x)$ as follows:

$$\cos\theta = \frac{dx}{\sqrt{dh^2 + dx^2}} \equiv \frac{1}{\sqrt{1 + [h'(x)]^2}} \tag{B.1a}$$

$$\sin\theta = \frac{dh}{\sqrt{dh^2 + dx^2}} \equiv \frac{h'(x)}{\sqrt{1 + [h'(x)]^2}} \tag{B.1b}$$

$$\tan\theta = \frac{dh}{dx} \equiv h'(x) \tag{B.1c}$$

Note that these derivatives are evaluated at $x = u$.

Now, applying dynamic equilibrium:

$$\rightarrow^+ \Sigma F_x = ma_x: \quad -N\sin\theta - \mu N\,\mathrm{sgn}(\dot{u})\cos\theta = m(\ddot{x}^t + \ddot{u}) \tag{B.2a}$$

$$\uparrow^+ \Sigma F_y = ma_y: \quad N\cos\theta - \mu N\,\mathrm{sgn}(\dot{u})\sin\theta - mg = m[\ddot{y}^t + h'(u)\ddot{u} + h''(u)\dot{u}^2] \tag{B.2b}$$

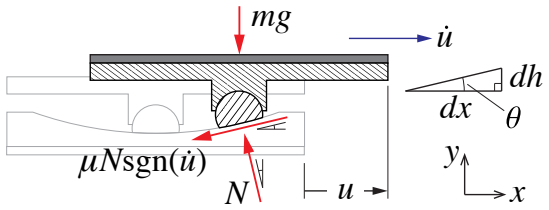


Figure B.1: Free body diagram of a FP bearing.

where the total acceleration a_y in the y-direction has been expressed in terms of u using the kinematic constraint (3.3). These two coupled equations have two unknowns: normal force N and motion u (and its derivatives). We seek to eliminate N, and write a single equation of motion in terms of only u. To do this, let's define a normalized normal force

$$\lambda \equiv \frac{1}{\sqrt{1 + [h'(u)]^2}} N$$

Doing so, and substituting the expressions (B.1) for the sine and cosine of θ into Eq. (B.2), the following equations are recovered:

$$-\lambda h'(u) - \mu\lambda \operatorname{sgn}(\dot{u}) = m(\ddot{x}^t + \ddot{u}) \tag{B.3a}$$

$$\lambda - \mu\lambda h'(u) \operatorname{sgn}(\dot{u}) - mg = m[\ddot{y}^t + h'(u)\ddot{u} + h''(u)\dot{u}^2] \tag{B.3b}$$

These equations are linear in the two unknowns (λ and $\ddot{u}$), so we can write them as follows:

$$\begin{bmatrix} 1 & \mu \operatorname{sgn}(\dot{u}) + h'(u) \\ h'(u) & \mu h'(u) \operatorname{sgn}(\dot{u}) - 1 \end{bmatrix} \begin{Bmatrix} m\ddot{u} \\ \lambda \end{Bmatrix} = \begin{Bmatrix} -m\ddot{x}^t \\ -m[\ddot{y}^t + h''(u)\dot{u}^2 + g] \end{Bmatrix} \tag{B.4}$$

Inverting the matrix and solving for the unknowns gives

$$\begin{Bmatrix} m\ddot{u} \\ \lambda \end{Bmatrix} = -\frac{1}{1 + [h'(u)]^2} \begin{bmatrix} \mu h'(u) \operatorname{sgn}(\dot{u}) - 1 & -\mu \operatorname{sgn}(\dot{u}) - h'(u) \\ -h'(u) & 1 \end{bmatrix} \begin{Bmatrix} -m\ddot{x}^t \\ -m[\ddot{y}^t + h''(u)\dot{u}^2 + g] \end{Bmatrix} \tag{B.5}$$

Expanding and simplifying the first equation gives

$$m\{1 + [h'(u)]^2\}\ddot{u} + mh'(u)h''(u)\dot{u}^2 + m\mu\{g + \ddot{y}^t + h''(u)\dot{u}^2 - h'(u)\ddot{x}^t\} \operatorname{sgn}(\dot{u}) + mgh'(u) = -m\ddot{x}^t - mh'(u)\ddot{y}^t \tag{B.6}$$

Appendix C
System Identification of Experimental Structure

Knowing the structural properties of each floor of the PS is an important step prior to building the mass, stiffness and damping matrices for the experimental system used in this study. To obtain such values can be a challenge since it is practically inconvenient to directly measure the mass of each floor and difficult, if not impossible, to measure their exact stiffness and damping. Therefore, a method of system identification is used to obtain such properties, which is done through a series of tests and analysis described in this appendix.

C.1 Mathematical Formulation

Consider a 3-degree-of-freedom mathematical model describing the 3-story shear-type experimental structure subject to base excitation $\ddot{u}_g(t)$:

$$\mathbf{M}\ddot{\mathbf{u}}(t) + \mathbf{C}\dot{\mathbf{u}}(t) + \mathbf{K}\mathbf{u}(t) = -\mathbf{M}\mathbf{1}\ddot{u}_g(t) \tag{C.1}$$

where

$$\mathbf{u}(t) = \begin{Bmatrix} u_1(t) \\ u_2(t) \\ u_3(t) \end{Bmatrix}, \mathbf{M} = \begin{bmatrix} m_1 & 0 & 0 \\ 0 & m_2 & 0 \\ 0 & 0 & m_3 \end{bmatrix}, \mathbf{K} = \begin{bmatrix} k_1 + k_2 & -k_2 & 0 \\ -k_2 & k_2 + k_3 & -k_3 \\ 0 & -k_3 & k_3 \end{bmatrix}, \mathbf{1} = \begin{Bmatrix} 1 \\ 1 \\ 1 \end{Bmatrix} \tag{C.2}$$

in which $u_i(t)$ is the displacement of the ith story level relative to the base, and m_i and k_i are the ith floor mass and story stiffness, respectively, which are to be determined.

Likewise, the damping matrix $\mathbf{C}$ will be determined experimentally.

Now, consider masses Δm_i that are added to each of the floors ($i = 1, 2, 3$). The equation of motion for the modified structure is given by

$$(\mathbf{M} + \Delta\mathbf{M})\ddot{\mathbf{u}}(t) + \mathbf{C}\dot{\mathbf{u}}(t) + \mathbf{K}\mathbf{u}(t) = -(\mathbf{M} + \Delta\mathbf{M})\mathbf{1}\ddot{u}_g(t) \tag{C.3}$$

where

$$\Delta\mathbf{M} = \begin{bmatrix} \Delta m_1 & 0 & 0 \\ 0 & \Delta m_2 & 0 \\ 0 & 0 & \Delta m_3 \end{bmatrix} \tag{C.4}$$

The modified equation of motion can be written in state-space form as follows:

$$\dot{\mathbf{x}}(t) = \mathbf{A}\mathbf{x}(t) + \mathbf{B}\ddot{u}_g(t) \tag{C.5}$$

where $\mathbf{x}(t) = [\mathbf{u}^{\mathrm{T}}(t) \;\; \dot{\mathbf{u}}^{\mathrm{T}}(t)]^{\mathrm{T}} \in \mathbb{R}^6$ is the state vector. The matrices in Equation (C.5) are defined as

$$\mathbf{A} = \begin{bmatrix} \mathbf{0}_{3\times3} & \mathbf{I}_{3\times3} \\ -(\mathbf{M} + \Delta\mathbf{M})^{-1}\mathbf{K} & -(\mathbf{M} + \Delta\mathbf{M})^{-1}\mathbf{C} \end{bmatrix}, \mathbf{B} = \begin{Bmatrix} \mathbf{0}_{3\times1} \\ -\mathbf{1} \end{Bmatrix} \tag{C.6}$$

The response quantities of interest are the total accelerations of each story level, i.e., $\ddot{u}_i(t) + \ddot{u}_g(t)$, which can be written in state-space form,

$$\mathbf{y}(t) = \ddot{\mathbf{u}}(t) + \mathbf{1}\ddot{u}_g(t) \equiv \mathbf{C}\mathbf{x}(t) + \mathbf{D}\ddot{u}_{\mathrm{g}}(t) \tag{C.7}$$

where

$$\mathbf{C} = \begin{bmatrix} -(\mathbf{M} + \Delta\mathbf{M})^{-1}\mathbf{K} & -(\mathbf{M} + \Delta\mathbf{M})^{-1}\mathbf{C} \end{bmatrix}, \text{ and } \mathbf{D} = \mathbf{0}_{3\times1} \tag{C.8}$$

The complex transfer function $H(f)$ at frequency f [Hz] is then given by

$$H(f) = \mathbf{C}(2\pi f j\,\mathbf{I} - \mathbf{A})^{-1}\mathbf{B} + \mathbf{D} \tag{C.9}$$

where $j = \sqrt{-1}$. Note that $H(f)$ is a 3-vector, where the ith entry, $H_i(f)$, is the transfer

function for the *i*th story.

Experimentally, the structure was subjected to band-limited (1–20 Hz) white noise, and the shake table and floor accelerations were recorded. Let these measured acceleration time histories be denoted $a_g(t)$ and $a_i(t)$ ($i = 1, 2, 3$), respectively, and their Fourier transforms calculated using the fast Fourier transform (FFT) at discrete frequencies f_j be denoted $A_g(f_j)$ and $A_i(f_j)$, respectively. The frequency response (gain) is defined by

$$G_i(f_j) = \frac{|A_i(f_j)|}{|A_g(f_j)|}, \ i = 1, 2, 3 \tag{C.10}$$

The frequency response $G_i(f_j)$ is simply the absolute value of the transfer function $H_i(f)$, which will be used to fit the structure parameters

$$\boldsymbol{x} = (m_1, m_2, m_3, c_1, c_2, c_3, k_1, k_2, k_3)$$

However, there is inherent redundancy in these parameters (i.e., the structure is defined by only six parameters, e.g., ω_1, ω_2, ω_3, ζ_1, ζ_2, and ζ_3), so one would typically measure as accurately as possible three of the parameters. Instead, in this study, additional *known* masses Δm_i are attached to the structure. A few different configurations ($l = 1, 2, 3, 4$; see Table C.1) are considered, where $H_i^l(f_j)$ and $G_i^l(f_j)$ denote respectively the transfer function and frequency response for the *l*th configuration.

Table C.1: Configurations for system identification

Configuration No.	Additional masses [kg (lb-s^2/ft)]		
	Δm_1	Δm_2	Δm_3
1	0	0	0
2	9.190 (0.6292)	0	0
3	9.190 (0.6292)	9.203 (0.6301)	0
4	18.34 (1.256)	0	0

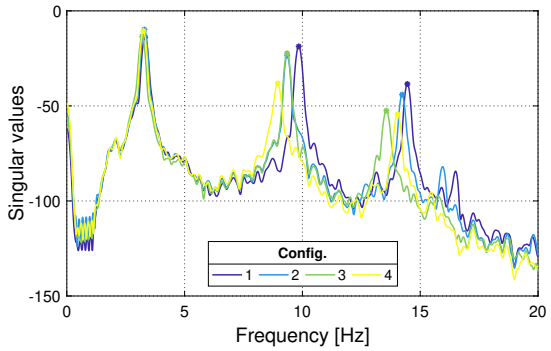


Figure C.1: First singular values of the power spectral density matrix for each configuration, with the identified frequencies indicated ($*$).

C.2 System Identification

The system identification was carried out using a two-step approach. The first step was to identify the masses and stiffnesses of the structure based on the identified modal frequencies. The second step was to estimate the modal damping ratios by fitting the transfer function to the frequency response data.

C.2.1 Mass and Stiffness Identification

To identify the modal frequencies of each configuration, frequency domain decomposition (FDD) (Brincker et al., 2001) was used. In this method, the power spectral density matrix is decomposed using the singular value decomposition, and the modal frequencies are found as the peaks in the spectrum of the first singular value. Figure C.1 shows the singular value spectra for each configuration, and the identified frequencies are tabulated in Table C.2.

Table C.2: Identified modal frequencies using frequency domain decomposition (FDD).

Modal frequency	Configuration no.			
	1	2	3	4
f_1 [Hz]	3.3222	3.2932	3.1952	3.2512
f_2 [Hz]	9.8425	9.3525	9.3485	8.9484
f_3 [Hz]	14.4547	14.232	13.563	14.037

A set of values for mass and stiffness of each floor were obtained via genetic algorithm (GA) to fit the modal frequencies of the PS. In this process, mass and stiffness of each floor were given a certain bound to be optimized. The mass of each floor was estimated based on the actual measurement of the experimental structure. Components of the structure that constitute the weight for each floor are shown in Table C.3. The first floor consists of a deck, 2 longitudinal ribs, a transverse rib, 2 longitudinal angles, 2 transverse angles, a large block below deck, a large block above deck, 2 small blocks, 4 columns, and 2 braces, which result in a total weight of 129.507 lb. The second floor has the same components as the first floor without the 2 small blocks, which constitute a total weight of 128.898 lb. The roof consists of the same components as the second floor but with only 2 columns and 1 brace, which result in a total weight of 117.875 lb.

Since the mass is known fairly accurately, the range given for the optimization of the mass is within ±5% of m_1 = 4.01 lb-s^2/ft, m_2 = 4.01 lb-s^2/ft, and m_3 = 3.66 lb-s^2/ft. On the other hand, stiffness is harder to estimate from the structure physically. Thus, the range given to optimize stiffness is more lenient, with a lower bound of 500 lb/in. and upper bound of 1500 lb/in.* The objective function for this optimization is based on the following equation, in which estimated modal frequencies $\hat{f}_i^l$ from the mathematical model were fitted to the identified modal frequencies f_i^l of the experimental structure, using their relative error:

$$(m_1, m_2, m_3, k_1, k_2, k_3)^* = \underset{m_1,m_2,m_3,k_1,k_2,k_3}{\arg\min} \sum_{l=1}^{4} \sum_{i=1}^{3} \left[\frac{f_i^l - \hat{f}_i^l}{f_i^l} \right]^2 \tag{C.11}$$

The optimization was run for multiple times to obtain values that provide the best estimate. After each run of the optimization, a set of values for m_1, m_2, m_3, k_1, k_2 and k_3 were obtained. These values are associated with certain errors from the comparison. However, the set that provides the smallest error was chosen. Thus, the identified

*These values are loosely based on four 0.75-in.-diameter columns of length 31.25 in., which gives a story stiffness of 708 lb/in., assuming fix-fixed boundary conditions.

Table C.3: Experimental structure components and weights.

System	Components	Dimension [in.]	Cross-sectional area [in.^{2}]	Length/thickness [in.]	Volume [in.^{3}]	Weight [lb]
Floor	Deck	PL 35.875 × 24.125	865.484	0.265	229.353	66.364
	Long. ribs	PL 31.250 × 2.000	62.500	0.250	15.625	4.521
	Trans. rib	PL 3.875 × 2.000	7.750	0.250	1.938	0.561
	Long. angles	L2×2×1/4	0.938	35.500	33.299	9.635
	Trans. angles	L2×2×1/4	0.938	19.500	18.291	5.293
Blocks	Large (below deck)	PL2 × 1	2	0.114	0.228	0.066
		Trapezoid1 × 2.75 × 3.375	6.328	0.110	0.696(×2)	0.403
	Large (above deck)	PL2 × 1.5	3	0.105	0.315	0.091
		PL2 × 1	2	0.105	0.21	0.061
		Trapezoid1 × 2.625 × 3.375	6.117	0.105	0.642(×2)	0.372
	Small blocks	PL1 × 1.875	1.875	0.115	0.216	0.0625
		Trapezoid1 × 2.375 × 2.25	3.797	0.110	0.418(×2)	0.242
LRFS	Columns	⌀3/4	0.442	31.250	13.813	3.997
	Braces	HSS1 × 1 × 0.083	0.27	39	10.530	3.047

masses and stiffness are $m_1^* = 56.06$ kg, $m_2^* = 56.29$ kg, and $m_3^* = 56.20$ kg (3.8385, 3.8540, and 3.8478 lb-s^2/ft, respectively) and $k_1^* = 112.83$ N/mm, $k_2^* = 135.64$ N/mm, and $k_3^* = 158.35$ N/mm (644.3, 774.5, and 904.2 lb/in., respectively). The estimated modal frequencies based on these values are given in Table C.4. On average, the relative error between the measured and estimated frequencies is 0.09%.

C.2.2 Modal Damping Estimation

To estimate modal damping of each mode, latin hypercube sampling was used for the optimization. In this method, 1000 sample points of damping ratio were used in an exhaustive search to optimize the fitness function. Even though nine parameters (m_1, m_2, m_3, k_1, k_2, k_3, ζ_1, ζ_2, and ζ_3) were being optimized, masses and stiffnesses were given a very narrow bound (within ±0.1% of their fitted values) since they were already identified in the previous section. For modal damping, each mode was fit independently starting from third to second to first mode. The fitness function for this optimization is posed as follows:

$$\zeta_n^* = \arg\min_{\zeta_n} \sum_{l=1}^{4} \sum_{i=1}^{3} \sum_{j} \left[\ln H_i^l(f_j) - \ln G_i^l(f_j) \right]^2 \tag{C.12}$$

As shown, transfer function is being fit to the frequency response data on the natural log scale to avoid the over-fitting of a large value. First, the values in the vicinity (±10%) of the third modal frequency of the structure were used to fit ζ_3, while damping ratio ζ_1 and ζ_2 were fixed to nearly zero. Then, the optimization is run to find the best fitted ζ_3.

Table C.4: Best estimates of modal frequencies based on GA-optimized masses and stiffnesses.

Modal frequency	Configuration no.			
	1	2	3	4
f_1 [Hz]	3.3242	3.2882	3.1965	3.2525
f_2 [Hz]	9.8292	9.3589	9.3462	8.9552
f_3 [Hz]	14.440	14.211	13.571	14.061

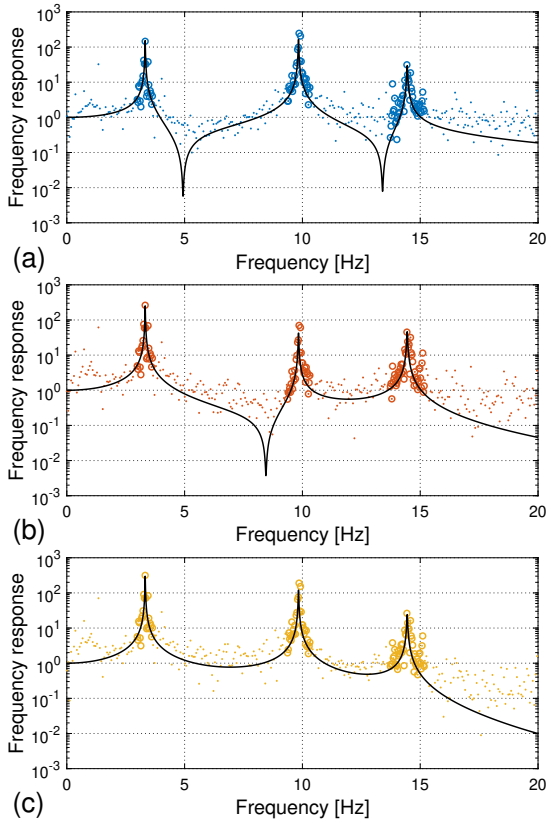


Figure C.2: Frequency response data (·) from the (a) first, (b) second, and (c) third floors, indicating selected data (○) used to fit modal damping ratios, with the fitted transfer functions (—).

Similar process was applied to obtain the second modal damping ratio. Values around the second modal frequency (also ±10%) were used to fit ζ_2, while ζ_1 and ζ_3 were held constant to zero and to the obtained value respectively. After ζ_2 was obtained from the optimization, ζ_1 was being fit last. Similarly, values in the vicinity of the first modal frequency were used to fit the first modal damping ratio, while ζ_2 and ζ_3 were held constant. Then, the optimization is run to obtain ζ_1.

From this optimization, the identified modal damping ratios are $\zeta_1^* = 0.1\%$, $\zeta_2^* = 0.1\%$, and $\zeta_3^* = 0.2\%$. The frequency response spectra of the structure from the experiment and the estimated modal damping are shown in Figure C.2.

Appendix D
Characterization Test

Figure D.1 shows the setup for sine sweep test to characterize the FIS. A laser is attached to measure the displacement of the isolated steel blocks. Accelerometer 1 and accelerometer 2 are installed to record the acceleration of the shake table and the isolated content respectively. Two bumpers are attached on both sides of the FIS as shown. They serve as shock absorbers to provide a gradual impact. The setup is mounted on a shake table ready for testing.

After the data is processed, it can be determined that the system is nonlinear as shown in Figure D.2.

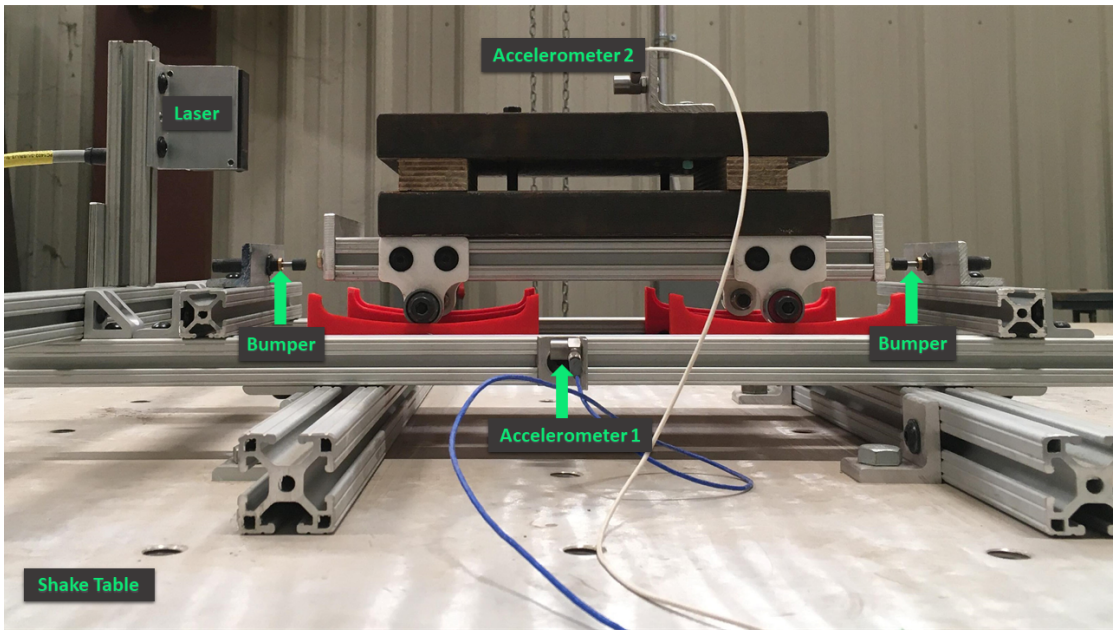


Figure D.1: FIS setup for sine sweep test

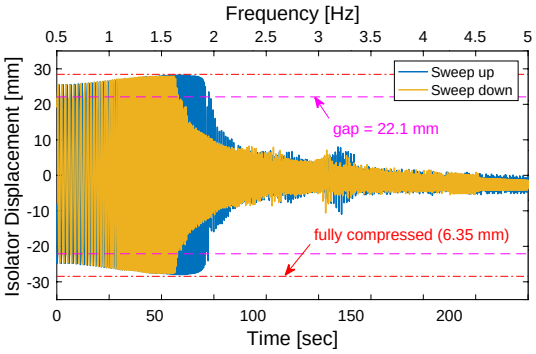


Figure D.2: Sine sweep test exhibiting hysteresis (history dependence)